الجمهورية الجزائرية الديمقراطية الشعبية

République Algérienne Démocratique et Populaire Ministère de L'Enseignement Supérieur et de la Recherche Scientifique



UNIVERSITÉ FERHAT ABBAS - SETIF1 FACULTÉ DE TECHNOLOGIE

THÈSE

Présentée au Département de Génie civil Pour l'obtention du diplôme de

DOCTORAT

Domaine : Sciences et Technologie

Filière: Génie civil Option: Matériaux et structures

Par

KHELLAF Abdelghani

THÈME

Approche par éléments discrets des sols granulaires. Application à l'analyse des pressions latérales des terres.

Soutenue le 08/07/2025 devant le Jury:

HADJI Riheb	Professeur	Univ. Ferhat Abbas Sétif 1	Président
MANSOURI Mouloud	M .C. A	Univ. Ferhat Abbas Sétif 1	Directeur de thèse
BOUAFIA Ali	Professeur	Univ. Saad Dahlab, Blida	Examinateur
RADJAI Farhang	Professeur	Univ. Montpellier, France	Examinateur
MEKERBI Mohamed	M .C. A	Univ. Ferhat Abbas Sétif 1	Examinateur

Dedications

To my parents,

for their unwavering love and support,

who have always believed in my dreams and encouraged me to pursue my passions.

To my beloved wife M. Bouthaina, whose unwavering love, patience, and support have been my greatest strength—this achievement is as much yours as it is mine.

And to my precious daughters (Khadidja, Ritadj and Israa), whose laughter and joy inspire me every day—may this work remind you that with perseverance and love, anything is possible.

To my friends,

for their companionship and encouragement,

who made this trip so pleasant and enjoyable.

To my thesis supervisor,

for his invaluable guidance and wisdom,

which has inspired me to strive for excellence in my research.

And finally, to all those who believe in the power of knowledge, this thesis is dedicated to you,

in the hope of contributing modestly to our understanding of the world.

Acknowledgments

I would like to express my gratitude to all the individuals who have, in one way or another, contributed to the successful completion of this work. Whether they were directly involved in my supervision or simply crossed my path during this journey, each encounter has been meaningful.

I would particularly like to thank my thesis supervisor, Dr Mouloud Mansouri, who graciously agreed to guide me throughout these years. His trust and invaluable advice enabled me to complete my thesis successfully. It was a real pleasure to work with him, and I am deeply grateful for his pedagogical approach, his scientific and technical expertise, and especially his exceptional human qualities. Thanks to our shared experience, he has greatly stimulated my desire to continue in the fields of research and teaching, for which I am sincerely grateful.

I would also like to thank all the members of my defense jury: Pr. Hadji Rihab for agreeing to chair the jury, Pr. FARHANG Radjai, Pr. BOUAFIA ALI and Dr. MEKERBI Mohamed for agreeing to evaluate this thesis. I would also like to take this opportunity to thank Pr. Hadji Rihab in particular for the many discussions we have had over these years. Many thanks to all those who have shared my daily life over the years, whether within the walls of the university, in the fresh mountain air, or even under the roses... Finally, I would like to express my deepest gratitude to my family, who have always supported me.

Sétif, 08/07/2025 Abdelghani; k

Summary

Introduction	XIV
Chapter 01	1
GRANULAR SOILS	1
1.1. Introduction	
1.2. Physical characteristics of a granular soil	2
1.2.1. The shape descriptors	
1.3. Mechanical behavior of granular soils	
1.3.1. Mechanical behavior under compression triaxial conditions	
1.3.2. Triaxial Test Overview	
1.3.3. Stress-Strain Response	
1.3.4. Characteristic state	
1.4. Conclusion	12
Chapter 02	13
DISCRETE ELEMENT METHOD	13
2.1. Introduction	13
2.2. Molecular Dynamics	13
2.2.1. Contact Forces	
2.2.2. Normal stiffness	
2.2.3. Viscous Damping	16
2.2.4. Tangential Stiffness	17
2.2.5. Friction and Sliding	
2.2.6. Rolling Resistance	
2.3. Numerical Resolution	
2.3.1. Explicit Resolution Scheme	
2.4. Numerical modeling Parameters	23
2.5. Modeling Techniques	25
2.5.1. Neighborhood Detection	
2.6. Generation of an Initial State (samples creation)	27
2.7. Boundary condition	30
2.8. Representative Elementary Volume	31
2.9. Usual grain shape models	
2.10. Conclusion	

Chapter 03	35
A STICK-SLIP FRICTION MODEL FOR DISCR	
3.1. Introduction	35
3.2. Stik-slip motion	
3.3. Usual contact models in DEM	
3.4. Stick-slip friction model	
3.5. Simulations and Discussion	
3.5.1. Quasi-static example	46
3.6. Discussion of results and model	
3.7. Model application for large scale specimen	
3.8. Conclusions	59
Application of DEM to the analysis of Pressures at rest in dry granular soils	LATERAL EARTH
4.1. Introduction	61
4.2. Discrete Element Method	64
4.3. Model properties	66
4.3.1. A description of the simulated oedometer	66
4.3.2. Microscopic sample properties	
4.3.3. Macroscopic geotechnical parameters4.4. Evolution of K_0 under oedometric loading	
4.4.1. Evolution of K_0 for a one loading-unloading cycle	67
4.5. Effects of micromechanical parameters on K_0	
4.5.1. Contact orientations and contact number	70 74
4.5.4. Analytical description	
4.5.5. Numerical simulations	
4.6. Summary discussion	
4.7. Conclusion	81

Chapter 05	83
APPLICATION OF DEM TO THE ANALYSIS OF THE ACTIVE AND PASSIVE LATERAL EARTH PRESSURES IN DRY GRANULAR	
SOILS	83
5.1. Introduction	83
5.2. Rankine limit states	84
5.3. Lateral forces on a vertical wall	87
5.4. Active and passive pressure mobilization displacements	88
5.5.1. Model dimensions	89
5.5.2. Backfill properties	90
5.6. Lateral earth pressure distribution at rest	93
5.7. Active and passive states simulations	95
5.9.1. A review on triaxial testing with different stress paths	101
5.9.2. Biaxial tests for passive and active pressure states	102
5.10. Conclusion	106
CONCLUSIONS AND PERSPECTIVES	108

List of Figures

Figure 1.1. Roundness Scale. (Power 1953)	.4
Figure 1.2. Typical granulometric curve.	.5
Figure 1.3. scheme of a triaxial cell extracted from the NF P 94-074(on the left) and the stresses on the samp (on the right).	
Figure 1.4. Typical stress-strain curves (on the left) and volumetric strain Vs axial strain curves (on the righ obtained from conventional biaxial tests	
Figure 1.5. parameters characterizing the stress-axial strain curves and volumetric strain-axial strain curves	.0
Figure 1.3. Behavior of loose and dense granular materials obtained from a simple shear test [22]	. 1
Figure 1.4: Critical state at large deformations [24].	2
Figure 2.1: Local contact reference frame	4
Figure 2.2.: Normal contact law. a. Normal contact stiffness; b. Normal stiffness and viscous damping1	5
Figure 2.3.: Tangential Contact Stiffness	7
Figure 2.4.: Standard Contact Law	9
Figure 2.5.: Verlet Time Integration Scheme	22
Figure 2.6.: Dynamic equivalent of a Disk Resting on a horizontal surface	24
Figure 2.7. Direct Detection Method.	26
Figure 2.8.: Container dividing Method.	26
Figure 2.9.: Delaunay Triangulation Method.	27
Figure 2.10.: Packing on a Square Grid.	29
Figure 2.11.: Voronoi Partition and Filling of Cells with Circular shaped Grains	30
Figure 2.12 Illustration of rigid, periodic and flexible boundaries used in DEM simulations. (a) Rigid boundarillustration; (b) periodic boundaries (c) flexible boundary [30]	
Figure 2.13 Dispersion of the σ-ε curves for two samples with identical properties of 500 and 4000 grain subjected to biaxial loading according to [31]	
Figure 3.1. Ottawa sands: $a - SEM$ photomicrograph, $b - an$ enlargement image of the framed area in (a) [59]3	36
Figure 3.2. Schematic view of the microscopic contact of tow surfaces: F_n – Normal forces, F_s – shear	ar
forces	36
Figure 3.3. Illustrative scheme of stick-slip behavior	37
Figure 3.4. Typical evolution of friction force in terms of shear velocity	37
Figure 3.5. Soft-contact particles interaction	39
Figure 3.6. Stick-slip friction model	ŀ 1
Figure 3.7. The diagram of the model implementation	13
Figure 3.8. Circular shaped grain translating on a planar surface	14
Figure 3.9. The friction force and the grain sliding evolution	
	16

Figure 3.11. Vertical position of the grain 1	47
Figure 3.12. Comparison between the presented friction models:	48
Figure 3.13. Schematic representation of the performed test the grain can undergo only a translation rotation being locked	
Figure 3.14. Friction force and $tan(\beta)$ evolution: a – with time; b – a zoom of the dynamic pawhere β is maintained constant such as $tan\beta = \mu_s$	
Figure 3.15. Translation velocity evolution	52
Figure 3.16. Grain size distribution	54
Figure 3.17. Diagram of the performed biaxial compression shear test	55
Figure 3.18. A snapshot of a simulated biaxial at failure phase	55
Figure 3.19. Deviatoric stresses Vs Axial strain	56
Figure 3.19. Volumetric deformation Vs Axial strain.	58
Figure 4.1. Grain interaction force models.	65
Figure 4.2. Illustration of the rolling resistance model.	65
Figure 4.3. Diagram of the simulated oedometer	66
Figure 4.4. Evolution of K_0 for one loading-unloading cycle,	68
Figure 4.5. Evolution of K_0 for three loading – unloading cycles	70
Figure 4.6. Fabric properties of the sample during the loading-unloading cycle	
Figure 4.7. Evolution of horizontal and vertical contact numbers in terms of vertical stress funloading cycle	
Figure 4.8. Rose diagram of number of contacts per direction,	74
Figure 4.9. Normal contact forces rose diagram	74
Figure 4.10. Force diagrams; (a) Frictionless grains, loading and unloading phases,	75
Figure 4.11. The simulated example	77
Figure 4.12. The degree of structural anisotropy vs vertical stress,	78
Figure 4.13. Evolution of K_0 in terms of the applied vertical stress.	79
Figure 5.1.: a. Stress state in a normally consolidated soil mass resting between smooth planes;	84
Figure 5.2.: Active limit equilibrium. a. Failure shape; b. Corresponding Mohr circles	85
Figure 5.3: Experimental failure mode in active limit state [134].	86
Figure 5.4. Passive limit equilibrium. a. Failure shape; b. Corresponding Mohr circles	86
Figure 5.5: lateral pressure distribution acting on vertical wall:(a) without surcharge, (b) with unifor	_
Figure 5.6: Variation of earth pressure with displacement	88
Figure 5.7: Model dimensions and boundary conditions.	89
Figure 5.8: Passive wedge calculated with Terzaghi's log-spiral method [117].	90
Figure 5.9: Snapshot of the backfill with flexible load chain above (black disks)	
Figure 5.10: Flexible chain contact's model.	91
Figure 5.11: lateral pressure coefficient variation under a variable vertical stress.	92
Figure 5.12: Backfill decomposition into 5 layers	93

Figure 5.13: Lateral Pressure distribution at-rest without wall-backfill friction.	94
Figure 5.14. Force chains distribution inside the backfill without wall-backfill friction	95
Figure 5.15: The sliding wedge and shearing bands (a) active state, (b) passive state. (the blue-colored grains more rolling movement)	_
Figure 5.16: Lateral earth pressure. (left) passive state, (right) active state.	97
Figure 5.17: Void ratio. (left) passive state, (right) active state.	98
Figure 5.18: Lateral earth pressure coefficients. (left) passive state, (right) active state	99
Figure 5.19: Lateral pressure distribution in backfill layers. (left) passive state, (right) active state	100
Figure 5.20: Triaxial total stress paths in p-q stress plane (drained test)	101
Figure 5.21: deviatoric stresses evolution during CBCT and BUCT.	103
Figure 5.22: Volumetric strain during CBCT and BUCT.	104
Figure 5.23 CBCT and BUCT Mohr circles and linear Mohr envelopes	105

List of tables

Table 1.1. Roundness Grades (Power 1953)	3
Table 1.2. MIT System of soil classification. $F = Fine$, $M = Medium$, $C = Coarse$.	5
Table 2.1. Usual grain shape models.	33
Table 3.1. Usual friction model.	40
Table 3.2. Simulations parameters.	44
Table 3.3. Parameters used for Biaxial tests	54
Table 3.4. Data and results of the performed shear tests	57
Table 3.5. Macroscopic shear strength parameters of the material obtained from a biaxial test	59
Table 4.3. Macroscopic shear strength parameters of the material obtained from a biaxial test	67
Table 5.1. Approximate Displacement Required to Mobilize Active and Passive Earth Pressures	89
Table 5.2. microscopic flexible chain grains parameters	91
Table 5.3. CBCT and BUCT shear strength parameters	105

List of Symbols

mi : The mass of a grain i.

n : The number of grains in the simulation.

xi : The position of grain i along the X-axis.

Fi : The force exerted on the grain i

 M_{ij} : The moment exerted on grain i.

Fij : The force exerted by grain j on grain i...

 $F_{ext,i}$: The external forces exerted on grain i.

g: The acceleration due to gravity.

 $\overrightarrow{e_x}, \overrightarrow{e_y}, \overrightarrow{e_z}$: The unit vectors of the global coordinate system along X, Y, and Z, respectively.

Gi : The center of mass of grain i.

 φ_i : Rotation of the frame attached to grain i relative to the global frame.

Ri : The radius of grain i.

 \overrightarrow{V}_{i} : The translational velocity of grain i.

 $\overrightarrow{\omega_i}$: The rotational velocity grain *i*.

C: The contact point between the two grains i, j.

 $\vec{V}_{r,c}$: The relative contact velocity.

 $\overrightarrow{G_lG_l}$: The branch vector.

 \vec{n} : The normal unit vector of the local coordinate system.

 \vec{S} : The tangential unit vector of the local coordinate system.

 V_n : The normal component of the relative contact velocity.

 V_s : The tangential component of the relative contact velocity.

 D_n : The normal overlap between two grains.

 D_s : The tangential displacement between two grains.

 t_0 : The time when the contact started.

 m_{eff} : The effective mass.

 t_c : The contact time..

 v_n : The normal damping coefficient.

 k_n : the normal stiffness.

 Δt : The time step.

 μ_s : static friction coefficients.

 μ_k : kinetic friction coefficients.

 F_s : Tangentiel contact force.

 F_n : Normal contact force.

 K_0 : At rest lateral earth pressure coefficient.

 K_a : the active lateral earth pressure coefficient.

 K_p : the passive lateral earth pressure coefficient.

 r_c : curve raidus.

 ξ : Roundness coefficient.

 Ψ : sphericity index.

 S_g : effective surface.

Introduction

The determination of lateral earth pressures is a very important element in geotechnical engineering, influencing the design and stability of various structures such as retaining walls, foundations, and earth embankments. Understanding the mechanisms governing these pressures is crucial to their correct estimation and to the stability and safety of geotechnical structures. Traditional methods for estimating lateral earth pressures, such as Rankine and Coulomb theories, provide valuable insights but often rely on simplifying assumptions that may not accurately reflect the complexities of granular soil behavior under different loading conditions.

In recent years, the discrete element method (DEM) has gained prominence as a powerful numerical approach for simulating the behavior of granular materials. This method, based on the concept of modeling particles as independent elements interacting across contact points, can provide a more detailed understanding of the mechanics involved in lateral earth pressure. The aim of this thesis is to investigate, using DEM, the lateral pressures of a granular soil in different states: at rest and in the active and passive states.

The thesis is structured into five chapters. The first chapter provides an overview of some fundamental aspects relating to the behavior of granular soils and lateral earth pressures, discussing key concepts and existing theories underlying the analysis of these pressures.

The second chapter discusses the principles of the discrete element method, highlighting its advantages over continuum-based approaches, and detailing its implementation for the simulation of granular materials.

The third chapter focuses on the development of the intergranular friction model used in this work. Friction is a key ingredient in the macromechanical response of granular materials. This model should help improve the fidelity of simulations and provide a better understanding of how frictional forces influence lateral pressure behavior.

The fourth chapter presents an investigation of the lateral pressure at rest in a granular soil by means of the discrete element method. This chapter highlights the underlying physics involved in the variation of lateral earth pressure when the soil is subjected to loading – unloading cycles.

Finally, the fifth presents an analysis of the lateral earth pressure in both active and passive states. By examining various scenarios and loading conditions, this chapter aims to demonstrate how DEM can provide a better understanding of the estimation of lateral earth pressures.

Chapter 01

GRANULAR SOILS

1.1. Introduction

Soils, in general, are complex mixtures of mineral grains resulting from chemical (oxidation), physical (temperature variations, freezing, etc.), and mechanical (erosion) weathering of rocks [1]. In geotechnical engineering, soils are typically classified based on grain size for granular materials (gravel, sand) and plasticity indices for cohesive soils (silt, clay). According to various classifications found in the literature [2], cohesive soils (fine soils) have particle sizes smaller than 20 µm. Their behavior is influenced by intergranular forces (such as electrical forces and Van der Waals forces...) that produce cohesion, as well as moisture content (capillarity). In contrast, granular soils (coarse soils) have particle sizes greater than 20 µm and lack chemical bonding, resulting in low cohesion.

From a modeling perspective, two distinct models of soil behavior can be identified: the continuous model, which assumes that the soil is a continuum characterized by stress - strain relationships, and the discrete model, which treats soil as a medium composed of multiple independent elements (granular soils), where macroscopic behavior is governed by the microscopic interactions of the particles.

In the context of this study, the term "granular soil" refers both to the discrete nature of the soil and to grained soils and all materials are considered non-cohesive soils.

Granular soils are commonly found in various geological settings and are characterized by their discrete particle nature. Here are some locations where granular soils can be encountered:

- Riverbeds and Floodplains: Granular soils, such as sands and gravels, are often deposited in
 riverbeds and floodplains through alluvial processes. These areas typically contain alluvial
 deposits that can vary significantly in composition and grain size due to sediment transport
 by water.
- Coastal Areas: Beach environments feature granular materials like sands, shaped by the action
 of waves and currents. Coastal dunes also consist of granular soils that have been formed by
 wind erosion and deposition.

• *Construction Sites*: During excavations for foundations or other civil engineering projects, granular soils may be encountered at varying depths. Their properties are essential for assessing stability and load-bearing capacity.

• *Natural Landscapes*: Granular soils can be found in natural landscapes such as deserts, where wind action creates sandy terrains, and in arid regions where erosion exposes underlying granular materials.

Granular soils exhibit distinctive behaviors. There is often a significant gap between the macro-scale properties of the soil and the individual characteristics of the grains. The structure of granular soils typically consists of a framework formed by larger particles, with smaller particles filling the pores between them. These smaller particles can move within these pores under the influence of hydraulic or mechanical forces. A mass of this material remains stable solely due to intergranular contact forces.

1.2. Physical characteristics of a granular soil

The macroscopic properties of a granular soil are closely linked to its particle characteristics, such as mineralogy, particle geometry, dimensions, particle size distribution, density and stiffness. They also depend on the structure of the material, its pore content, and the contents of the pores (e.g. air, water, etc.)

1.2.1. The shape descriptors

The shape of the grains is an intrinsic characteristic that plays a major role in the mechanical behavior of granular media. The shape descriptors (sphericity, roundness, roughness and the size distribution) of the grains are the main factors that influence the interparticular forces [3], [4], [5]. Due to the diversity of the minerals entering into their composition and that of the conditions of their formation, granular soils appear as natural materials presenting the most varied grain shapes. At the particle scale, the general shape of the particle is described in terms of sphericity, roundness as opposed to angularity [7]. On a lower scale, that of the asperities; it is the surface state of the particles which is described in terms of roughness, the rounding of the vertices.

1.2.1.1. Roundness and sphericity

The criteria established by Wadell (1932) [8] and Powers (1953) [9], which focus on roundness and sphericity, are commonly used to characterize the morphology of grains. This concept of roundness

and sphericity was initially introduced to describe quartz particles.

The most commonly used definition of the roundness of a particle was proposed by Wadell [10], who defined roundness (ξ) as the ratio of the average radius of curvature (r_c) of the corners on the effective surface (S_g) of the particle to the radius (R) of the maximum inscribed circle in the plane of measurement:

$$\xi = \frac{\iint r_c \cdot ds}{S_a R} \tag{1.1}$$

He also defined a parameter Ψ known as the sphericity index, which characterizes the sphericity of a particle as the ratio of the surface area of a sphere with the same volume as the grain (Ss) to the effective surface of the grain:

$$\Psi = \frac{\pi^{\frac{1}{3}} (6S_S)^{\frac{2}{3}}}{S_q} \tag{1.2}$$

Powers (1953) developed a method that illustrates the concept of roundness through photographs. As shown in Table 1.1 and depicted in Figure 1.1, a roundness value close to 1 indicates that the particle's surface has relatively large radii of curvature (in relation to the grain size), while a roundness value close to 0 indicates very high angularity.

Class intervals Grade terms Geometric means Very angular 0.12 - 0.170.14 0.17-0.25 0.21 Angular 0.25-0.35 Subangular 0.30 Subrounded 0.35-0.49 0.41 Rounded 0.49 - 0.70.59 Well rounded 0.7 - 1.000.84

Table 1.1. Roundness Grades (Power 1953)

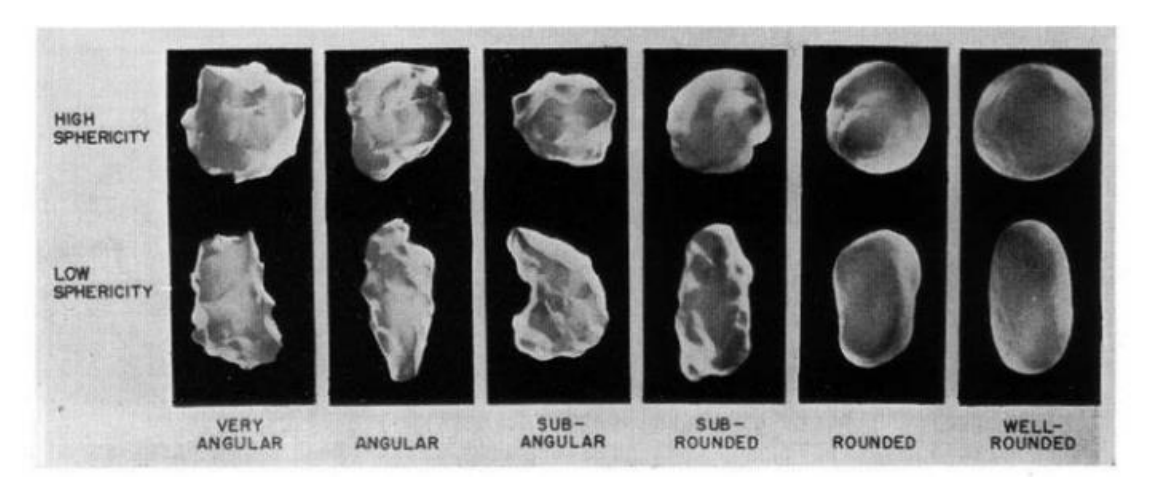


Figure 1.1. Roundness Scale. (Power 1953)

In soil mechanics, the visual determination of the roundness is not always applicable; instead, developed techniques are often used, such as fractal analysis, Fourier methods and image analysis and processing [11][12].

1.2.1.2. Roughness

The roughness of a particle describes the texture in relation to its radius, on a scale that is much smaller than the diameter of the particle. The direct measurement of the roughness is difficult; therefore, it is usually measured in relation to the length of the interparticle contact zone. For a particle rolling on a sliding surface of the same material or of a different material, the roughness controls the viscous friction. Senetakis et al [13] and Sandeep et al [14] measured the roughness of sand quartz minerals using white light interferometry and a Sympatec QicPic laser scanner, and the average roughness was found to be $0.38 \pm 0.19~\mu m$. Similar work was conducted by Yang and Baudet [15] using the power spectrum method. Miura, Maeda and Toki [16] noted that by increasing the roughness of the base on which the sand is piled, the angle of repose also increases; consequently, the formation of a pile on a frictionless base is almost impossible.

1.2.1.3. The particules size distribution

In geotechnical engineering, a soil sample can be defined by its grain size distribution. This distribution provides information about the mass proportions of each particle size present in the material. The presence of particles of different sizes in different proportions can radically alter the arrangement of particles, and consequently play an important role in the mechanical behavior of granular materials [17]. Macroscopic behavior depends on the network of intergranular contacts; consequently, any change in their arrangement also affects the local and macroscopic characteristics of the granular material.

Figure 1.2 illustrates a typical grain size curve for a soil sample. In this figure, the x values represent diameters corresponding to x percent passing. The diameters d10, d30, d50, and d60 are characteristic values of the grain size curve and are used to define:

- Uniformity Coefficient $C_u = d60/d10$: This coefficient characterizes the spread of the grain size distribution curve. A distribution is considered well-graded when the uniformity coefficient $C_u > 3$ and poorly graded when $C_u < 3$.
- Curvature Coefficient $C_c = d_{30}^2/(d10 \times d60)$: This coefficient provides information about the shape of the grain size distribution curve. For example, when $C_u > 3$ for sand, a value of $1 < C_c < 3$ indicates a well-graded distribution.

These particle size characteristics have a major impact on aggregate quality. In the field of civil engineering, these characteristics play an important role in the classification of the materials used. A basic classification of soils according to grain diameter, in accordance with the NF P18-560 standard, is presented in Table 1.2. This classification, along with many others (ASTM, AASHTO, MIT) [1], is found in the literature and distinguishes two types of soils: granular soils, which are the focus of this study, and fine soils.

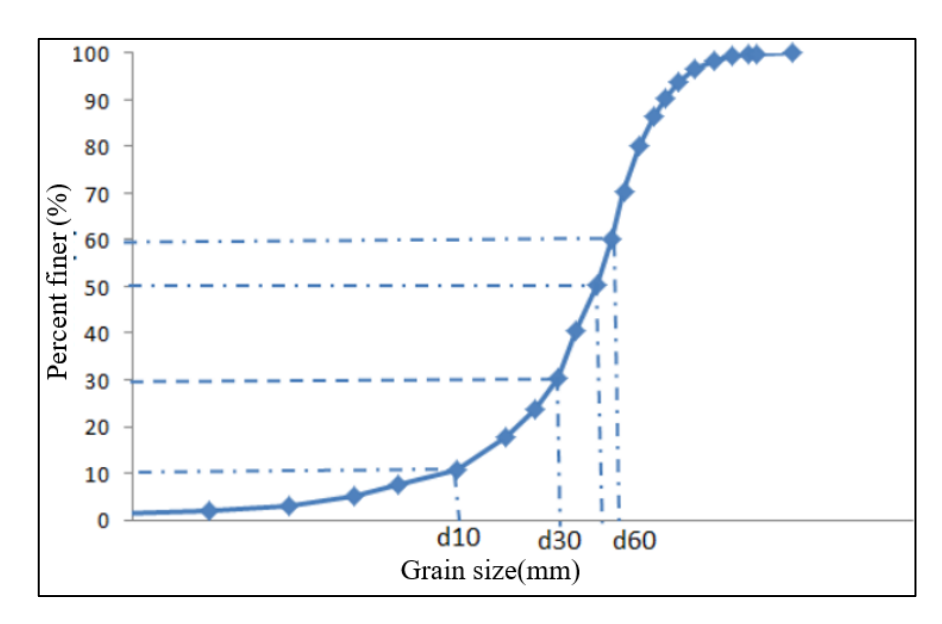
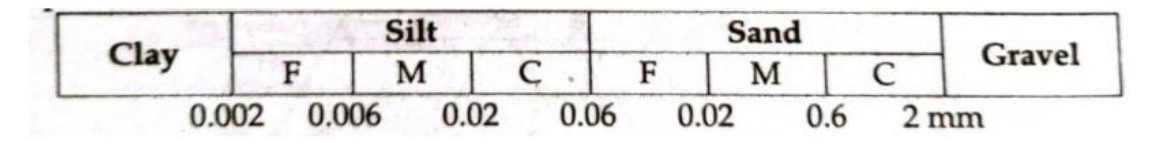


Figure 1.2. Typical granulometric curve.

Table 1.2. MIT System of soil classification. F = Fine, M = Medium, C = Coarse.



1.2.1.4. Density of a granular media

The relative density of a soil can be defined by several parameters, including compactness, porosity, and void ratio. It reflects the quantitative distribution of pores within the soil. Considering a soil sample with a total volume of V_T , the volume of solid particles V_S , and the volume of pores V_V , we can express:

Porosity:
$$n = \frac{V_V}{V_T}$$
 (1.3)

Void ratio:
$$e = \frac{V_V}{V_S}$$
 (1.4)

According to Bonneau and Soucher (1994), it is important to distinguish between textural porosity and structural porosity:

- ➤ **Textural porosity** is closely related to the arrangement of the particles constituting the material (sands, clay, etc.). Within this textural porosity, we also distinguish two types of porosity:
 - **Effective porosity**: This is generally used to characterize the entire network of connected pores through which water can flow. The permeability of the material is closely related to this parameter, i.e. effective porosity.
 - **Total porosity** corresponds to both connected and unconnected pores. It significantly influences the soil strength.
- > Structural porosity: it represents the spaces existing between the aggregates of the soil. It is greatly influenced by time and is considered variable throughout the history of the material.

1.3. Mechanical behavior of granular soils

Granular soils are often treated as continuous media when the scale of observation of these soils is large in comparison with the size of the grains of which they are composed. In this case, it is assumed that these materials obey to a constitutive law (or rheological law), thus one can know the response in stresses and strains for a given loading path (in stresses and/or strains). However, obtaining a general constitutive law remains difficult, so we are often limited to particular constitutive laws often linked to specific stress paths. The specification of a stress path is made according to the practical problem treated.

Shear tests are used to characterize the shear strength of materials. The most common tests are the direct shear test and the triaxial test. For the latter, a distinction must be made between compression and extension tests, which differ in terms of stress path and boundary conditions imposed. Although the direct shear test is easier to implement than the triaxial test, it has drawbacks such as the lack of access to stresses on its walls (the same drawback applies to ring shear tests) and the non-homogeneity of stresses in the volume due to an imposed failure surface. In the following, we limit ourselves to describing the mechanical behavior typically observed in granular soils subjected to triaxial testing. The mechanical responses of triaxial extensional compression tests are analyzed in Chapter 5 through a numerical modeling.

1.3.1. Mechanical behavior under compression triaxial conditions

The mechanical behavior of sand is critical for understanding its performance in various geotechnical applications. Triaxial testing is a widely accepted laboratory procedure used to evaluate the shear strength and deformation characteristics of soils, including sands. This section provides a detailed overview of the behavior of sand subjected to triaxial conditions, focusing on the effects of confining pressure, drainage conditions, and loading paths.

1.3.2. Triaxial Test Overview

The triaxial testing involves subjecting a soil specimen to controlled stresses in three dimensions. The samples tested are cylindrical, with a typical slenderness ratio of 2. They are protected by a thin impermeable membrane and placed in a triaxial cell consisting of a cylindrical chamber and an axial piston, as shown in figure 1.3. A hydrostatic pressure known as confining pressure (σ_3) is applied to the sample through a fluid contained in the chamber. The test consists of applying to the sample a confining stress (often isotopically: $\sigma_1 = \sigma_3$), then imposing an axial deformation (ε_1) using the piston, this is the shear phase where $\sigma_1 > \sigma_3$ (σ_1 and σ_3 are illustrated in Figure 1.3, on the right). The deviator stress, noted as q, is expressed in terms of σ_1 and σ_3 as given by equation 1.5. The test can be conducted under different drainage conditions, leading to three primary types: Consolidated Drained (CD), Consolidated Undrained (CU), and Unconsolidated Undrained (UU) tests. Each type provides insights into the mechanical properties of sand under varying stress states.

Consolidated Drained (CD) Test: A test is classified as a consolidated drained (CD) test
when the internal drainage remains open during the phases of isotropic compression (or
confinement) and shear phases. This test is particularly useful for understanding the long-term
behavior of sands under effective stress conditions.



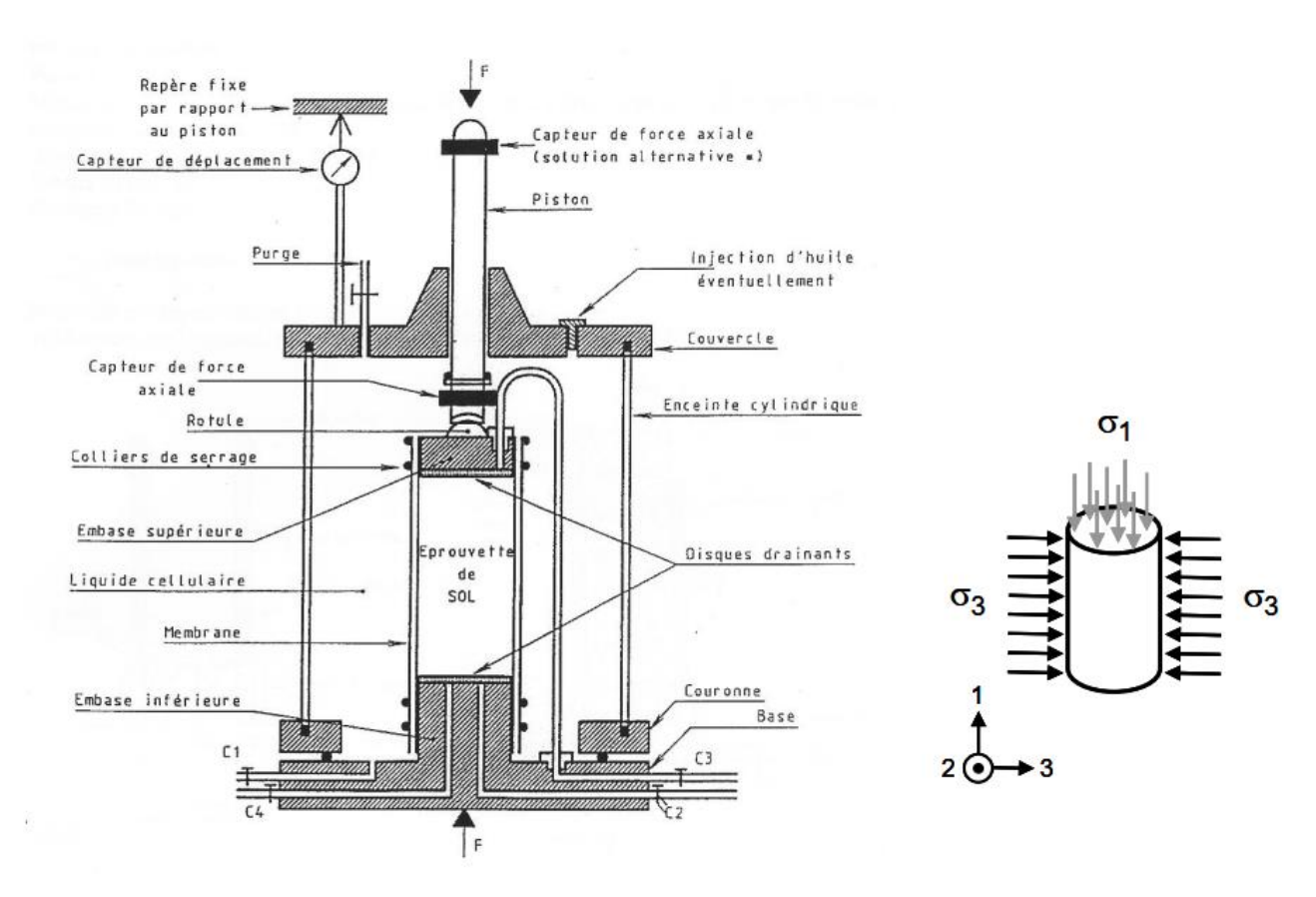


Figure 1.3. scheme of a triaxial cell extracted from the NF P 94-074(on the left) and the stresses on the sample (on the right).

- 2. **Consolidated Undrained (CU) Test**: In this procedure, the specimen is allowed to consolidate under confining pressure (drained), but it is sheared without drainage (during the application of deviator stress). This test is essential for assessing the short-term stability of saturated soils, especially during rapid loading scenarios.
- Unconsolidated Undrained (UU) Test: In this test, the drainage is not allowed during both
 phases of confining and shearing. The test is therefore suitable for evaluating the immediate
 response of saturated soils to rapid loadings.

1.3.3. Stress-Strain Response

In the following we focus on the mechanical behavior of granular soils such as dry sands. For these materials, the typical stress-strain behavior obtained from the compression triaxial test performed on loose and dense samples are presented in Figure 1.4. For an initially dense material, mobilization of the maximum strength occurs at low strain, the strength reaches a maximum value

(peak strength) before decreasing and stabilizing at a value called constant-volume shear stress. For an initially loose sample, peak resistance does not occur, but maximum resistance is reached at higher strain, corresponding to the constant-volume shear stress plateau. This plateau is almost the same for initially dense and loose samples. Regarding the volume deformation, it can be seen that the dense sample initially exhibits a small contracting phase, then becomes dilating throughout the rest of the shearing process: $(d\varepsilon_v/dt > 0)$. The loose sample, on the other hand, shows rapid contracting at the start of shearing $(d\varepsilon_v/dt < 0)$, after which it deforms at almost constant volume.

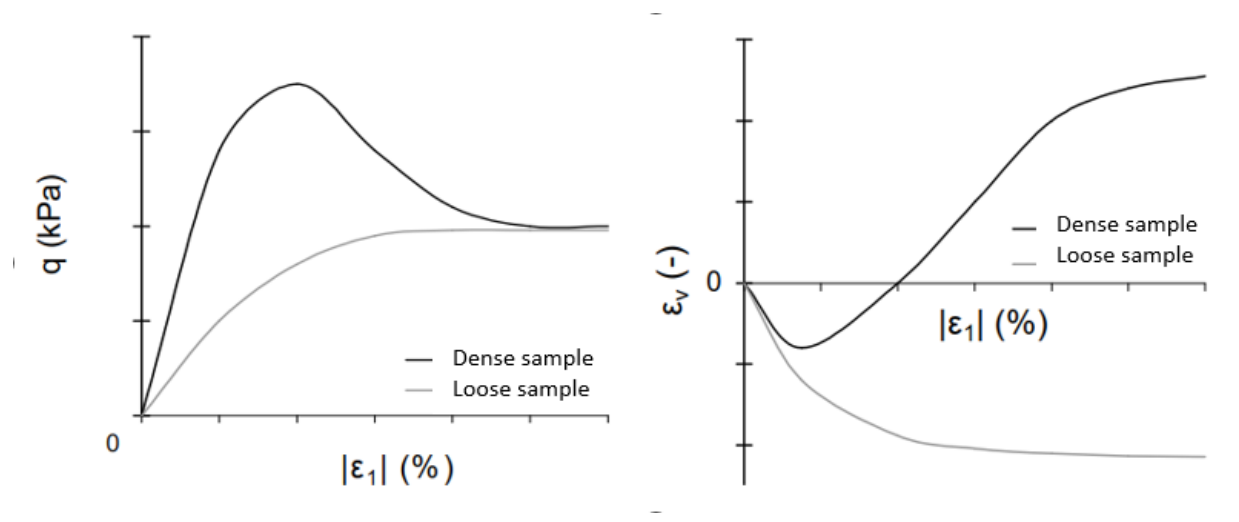


Figure 1.4. Typical stress-strain curves (on the left) and volumetric strain *Vs* axial strain curves (on the right) obtained from conventional biaxial tests.

Figure 1.5 summarizes the main parameters used to characterize the stress-axial strain curves and volumetric strain-axial strain curves. The parameters E_0 and v_0 characterize the initial slope of the stress and volumetric strain curves during their quasi-linear phase, referred to the pseudo-elastic phase. The maximum value reached by the deviator is called q_{peak} , and the "plateau" value for large deformations is q_{res} . This so-called residual value characterizes the critical state. Values of friction angles can also be used to characterize the resistance of a material. For a non-cohesive soil, equation 1.6 provides the relationship between the friction angle φ and the deviator q for any axial deformation. The quasi-linear part of the dilatancy phase is characterized by a dilatancy angle (ψ) defined by Sallam (2004) [18] according to equation 1.7. In the following sections of the thesis, the conventional biaxial tests are CD tests. The notation ε_1 will denote absolute axial strain.

$$\sin(\varphi) = \frac{q}{q + 2\sigma_3} \tag{1.6}$$

$$\sin(\psi) = \left(d\varepsilon_v/d\varepsilon_1\right)/\left(2 - \frac{d\varepsilon_v}{d\varepsilon_1}\right) \tag{1.7}$$

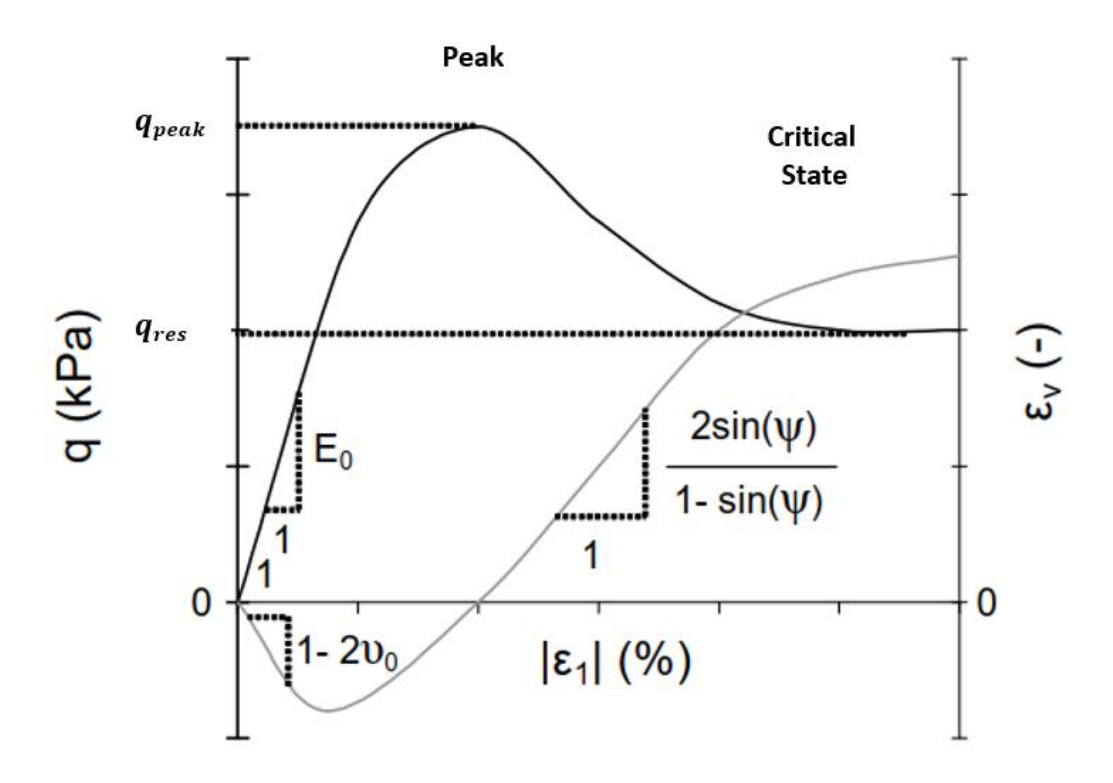


Figure 1.5. parameters characterizing the stress-axial strain curves and volumetric strain-axial strain curves.

1.3.4. Characteristic state

As defined by Schofield wroth 1968 [19], Habib and Luong (1978) [20], it corresponds to the state of the material at its transition from contractive behavior to dilative behavior during shear loading, whether drained or undrained. Scott (1963) [21] showed that the dilatancy of a soil depends on the density of the initial packing. If this density exceeds the value of a critical density, a dilatancy occurs during shearing; if it is lower, contraction occurs (Figure 1.3). This critical density corresponds to large deformations of the soil at constant volume under constant shear stress. According to Bousaid (2004) and Casagrande (1936), the critical density or the critical void ratio of sand depend of the normal stress σ_n .

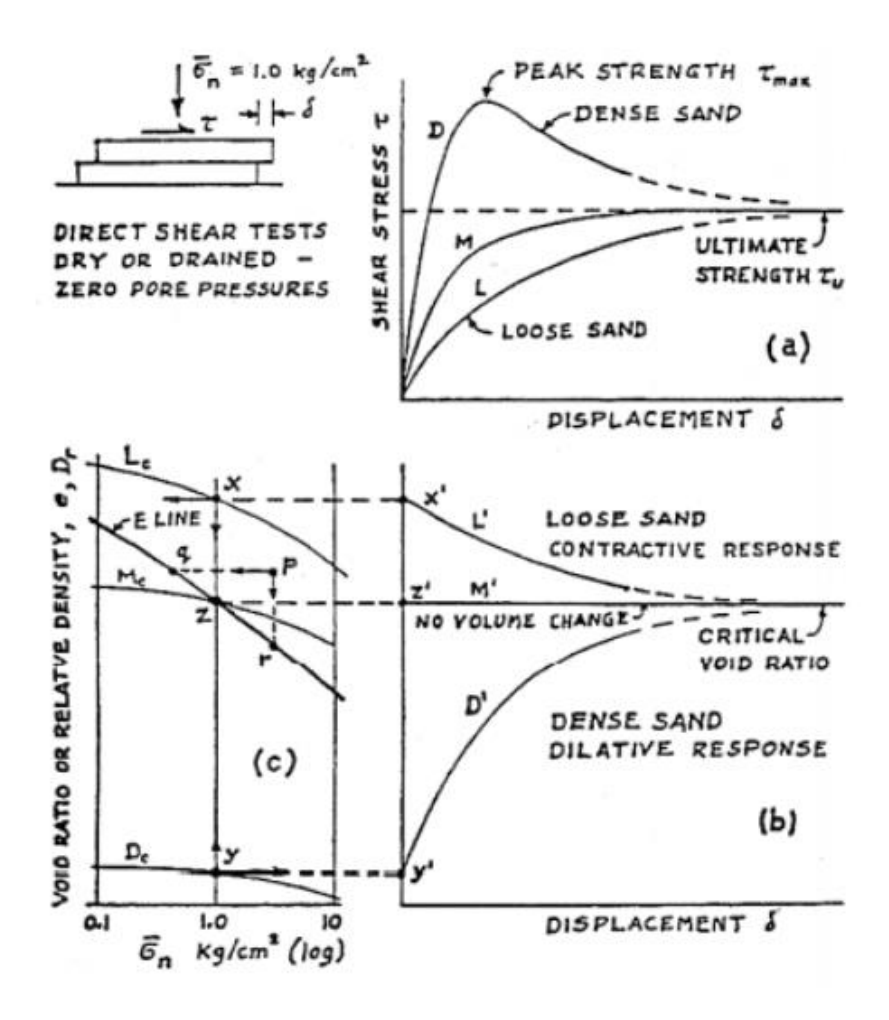


Figure 1.6. Behavior of loose and dense granular materials obtained from a simple shear test [22].

In the case of saturated sand subjected to undrained shear, the tendency toward dilatancy or contractance for a respectively dense or loose state is reflected by a decrease or an increase in pore pressure. Under these conditions, the undrained shear of loose sand, whose initial state is above the critical void ratio, can lead to an accumulation of pore pressures and result in its collapse after losing its strength. This mode of collapse is the phenomenon of liquefaction.

Since Casagrande (1936), there has been a considerable discussion regarding the relevance of critical density under large deformations. Several experiments have been conducted on Hostun sand to investigate critical density [23-25]. The results of [24] and [25] indicate that the critical density is the same for equal mean effective stresses when the strain reaches 30% or 40%, even for different initial relative densities. Experiments on dense sand presented in [24] showed a tendency towards a horizontal asymptote for axial deformations exceeding 30% (figure 1.4). It was concluded that the critical density only becomes apparent after 30% deformation.

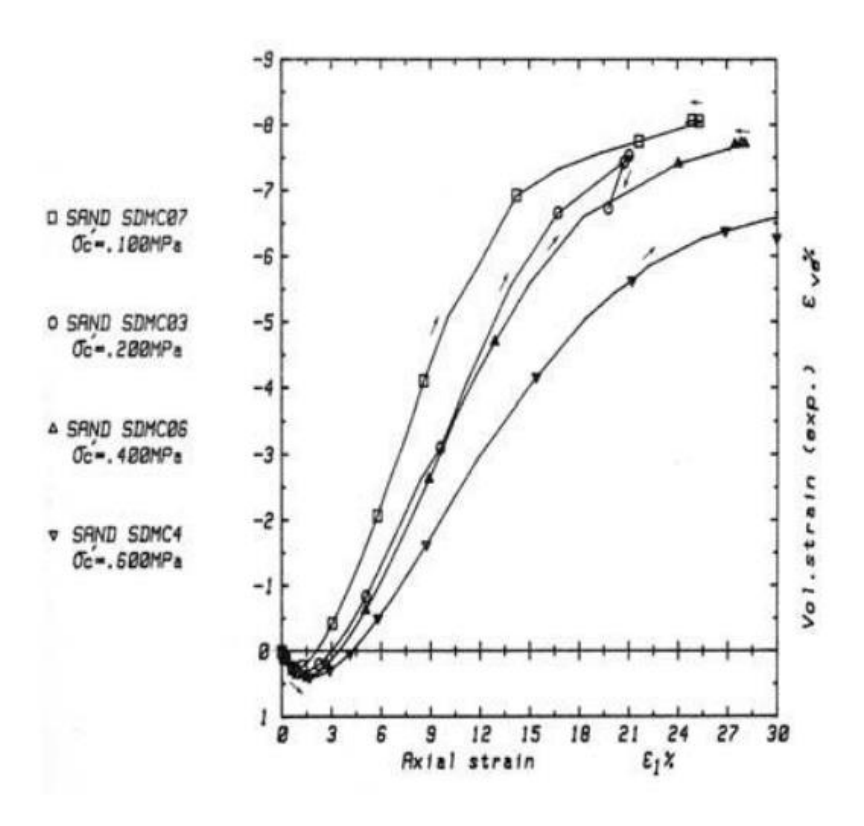


Figure 1.7: Critical state at large deformations [24].

1.4. Conclusion

In this chapter we present a review of the characteristics of granular soils, covering their definitions, physical characteristics and mechanical behavior. Granular soils play a crucial role in geotechnical engineering due to their widespread presence and significant influence on soil behavior and stability.

We began by defining granular soils and discussing their classification according to grain size and shape, which directly affects their physical properties. Key characteristics such as density, porosity and particle size distribution were examined, highlighting how these factors influence the overall behavior of granular materials. We then focused on shear strength, dilatancy, and contraction, illustrating how these behaviors are influenced by factors such as relative density and confining pressure.

Chapter 02

DISCRETE ELEMENT METHOD

2.1. Introduction

Historically, the principles of discrete modeling originated from the foundational paper by P.A. Cundall and O.D.L. Strack (1979) [27]. Around the same time, a similar method known as Molecular Dynamics (MD) was already quite widespread among physicists for calculating particle trajectories at the atomic scale; this approach would later be extended to more macroscopic and granular scales by Allen and Tildesley (1987). An alternative method called Non-Smooth Contact Dynamics (NSCD) was proposed in 1992 by J.J. Moreau and M. Jean [28], based on rigorous mathematical formalism.

Currently, Cundall and Strack's DEM approach remains the most widely used in the world, and its application is becoming increasingly common in both academic and industrial circles. This method, sometimes referred to as DEM-MD (although this name is often debated as it does not concern molecules but solids), is being adopted within the scope of the present thesis project.

2.2. Molecular Dynamics

This method has the advantage of being simple, since it is based on the idea of solving Newton's equation of motion applied to each grain:

$$\sum \vec{F} = m_i \frac{d^2 \vec{x}_i}{dt^2} \tag{2.1}$$

In this expression, m_i is the mass of the grain i, \vec{x}_i is its position vector, and \vec{F} is the resultant of the forces acting on this grain (including contact forces and gravity). An analogous equation can be written for rotational degrees of freedom.

The DEM-MD method is also flexible, as it can integrate all types of forces that can act on grain equilibrium, arising from different physics such as friction, cohesion, cementation, magnetism, hydraulic drag, etc. It is general because it enables a wide variety of situations ranging from quasistatic to violent collisional conditions. In addition, it is very informative since it provides kinematic and dynamic information at the grain scale (instantaneous velocities and contact forces, for example), which remains largely inaccessible to experimental measurement. Thus, discrete simulation is often

likened to "numerical experimentation," although it is important to keep in mind the limitations of this experimental analogy. However, it should be pointed out that the DEM method has a major drawback in terms of its excessively long computation times. For this reason, it is generally applied to the simulation of granular samples of limited size, and its application is often restricted to an academic context. Nevertheless, the constant improvement in computing resources and the development of parallel computing algorithms are enabling it to be used more and more in industry in a truly operational context.

2.2.1. Contact Forces

Contact force models are an essential part of discrete element modeling. An intergranular contact force is commonly decomposed into normal and tangential components, each of which is calculated by a specific model. It is common practice to use simple models to save calculation time.

Consider here the situation where two grains, denoted as i (with center C_i and radius r_i) and j (with center C_j and radius r_j), are in contact at a point C. The points C_i , C_j and C are aligned, and this alignment allows to define a direction \vec{n} called the "normal to contact," pointing from C_i to C_j . The line tangent to both circles and passing through the point C is orthogonal to \vec{n} , defining a direction \vec{s} called the "tangential to contact" (Figure. 2.1). With this reference frame, we can express any contact force applied by grain j on grain i as follows:

$$\vec{F}_{ij} = F_n \, \vec{n} + F_s \, \vec{s} \tag{2.2}$$

The normal F_n and tangential F_s components of the contact force are generally calculated according to different procedures, based on kinematic quantities (positions and velocities of the two grains) or multiphysical parameters.

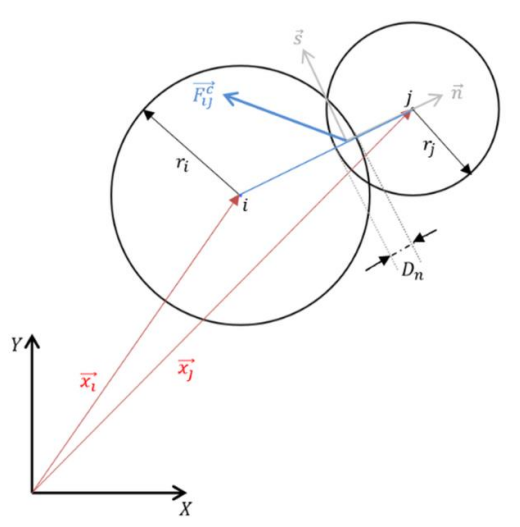


Figure 2.1.: Local contact reference frame

In the general case of contact between two solids, deformation occurs and contact is actually made on a surface instead of a point (e.g., according to Hertz theory). This deformation is generally negligible compared to the size of the contacting solids. Within the framework of the DEM-MD, it is assumed that the grains remain rigid and undeformable but have the ability to slightly overlap, and the contact force is then calculated based on this overlap.

2.2.2. Normal stiffness

Referring to Fig. 2.1, the normal relative distance D_n between grains i and j, referred to as the gap or the overlap is calculated as follows:

$$D_n = \|\vec{x}_i - \vec{x}_i\| - r_i - r_i \tag{2.3}$$

In this expression, \vec{x}_i and \vec{x}_j are the position vectors of the centers of the two grains. When, $D_n > 0$ the grains are not in contact and no repulsive force exists. In contrast, when $D_n < 0$, the grains are in contact and a repulsive force is developed, the greater the overlap, the greater the repulsive force. The simplest model is to consider that this force is proportional to the intergranular overlap, thus the intergranular repulsive force in expressed:

$$F_n = \begin{cases} 0 & if D_n > 0 \\ -k_n D_n & if D_n < 0 \end{cases}$$
 (2.4)

The spring constant k_n is referred to as the "normal contact stiffness". Unlike the Hertz theory where the repulsive force depends the grain material properties, the stiffness k_n is considered as a modeling parameter chosen to ensure efficient modeling. Note that this stiffness must be sufficiently high to ensure that overlap between grains remains limited.

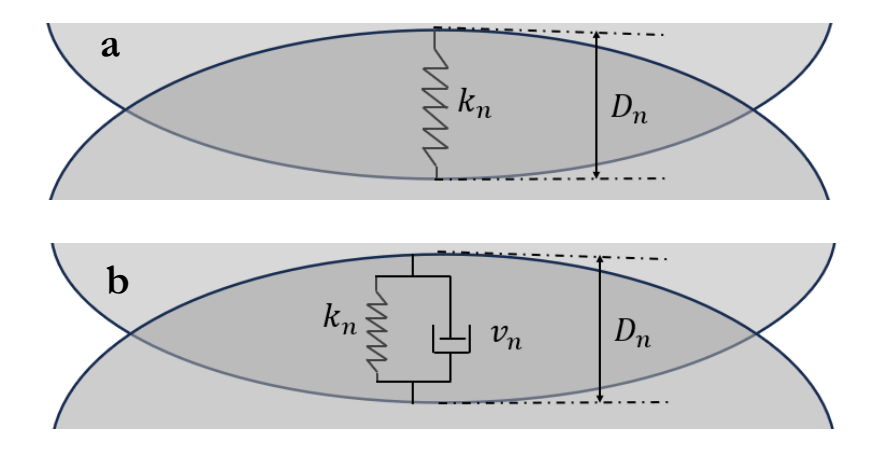


Figure 2.2.: Normal contact law. a. Normal contact stiffness; b. Normal stiffness and viscous damping.

2.2.3. Viscous Damping

The use of an elastic contact cannot reproduce the reality of granular material behavior, as it does not introduce any energy dissipation. However, it is clear that one of the main characteristics of a granular medium is its strong dissipative nature during each interaction between grains. The simplest way to model this dissipation in explicit DEM is to introduce viscous damping in parallel with the normal contact stiffness (Figure. 2.2b). The damping coefficient is denoted as v_n . Specifically, this amounts to applying a force proportional to the relative normal velocity of the grains, directed opposite to this velocity.

On a single impact, this force will be repulsive when the grains move closer together, and attractive when the grains move apart. The viscoelastic normal force model is therefore expressed as follows:

$$F_{n} = \begin{cases} 0 & if D_{n} > 0 \\ -k_{n}D_{n} - v_{n} \frac{dD_{n}}{dt} & if D_{n} < 0 \end{cases}$$
 (2.5)

However, it should be noted that, this formulation has the disadvantage of applying an overall attractive force (including both the spring and the damper) during a certain phase of the contact. Indeed, at the very end of the unloading phase (when the two grains are about to separate), the interpenetration has become very small while the separation velocity is at its maximum. The repulsive force $-k_nD_n$ becomes negligible compared to the attractive force $-v_n\frac{dD_n}{dt}$, and the grains tend to develop a net contact force that restricts their separation. In the absence of cohesion, this force is not physically realistic. To resolve this issue, one can decide to truncate the contact force: we calculate a value of F_n from equation (2.5) and replace it with zero if it is attractive. It is worth noting that, the equation (2.5) involves the quantity $v_n\frac{dD_n}{dt}$, which has not yet been expressed. In equation (2.5), $\frac{dD_n}{dt}$ represents the relative velocity of the grains projected onto the normal direction \vec{n} , which can be expressed as:

$$\frac{dD_n}{dt} = (\vec{V_l} - \vec{V_j})\vec{n}$$
 (2.6)

For grains without rotations, $\vec{V_i}$ and $\vec{V_j}$ represent the velocity vectors of the centers of mass of the grains i and j in the global reference frame, defined by:

$$\vec{V_i} = \frac{d\vec{x_i}}{dt} \tag{2.7}$$

2.2.4. Tangential Stiffness

The calculations of stiffness proposed in the normal direction are made simple by the existence of equation (2.3), which allows us to know the state of compression of the normal spring at any moment based on the positions of the particles. It is known, in particular, that the equilibrium point of the spring corresponds to positions where the grains are perfectly tangent. Such an equation does not exist in the tangential direction, which complicates matters. However, we wish to take advantage of the flexibility of the regularized approach (i.e., involving a stiffness opposing overlap) in the tangential direction as well. For this reason, we imagine that, during overlap, a spring is also set up in the tangential direction, developing a tangential force that adds to the normal forces from the previous sections (Figure. 2.3). By analogy with the normal direction, we refer to the elongation of this spring as D_s .

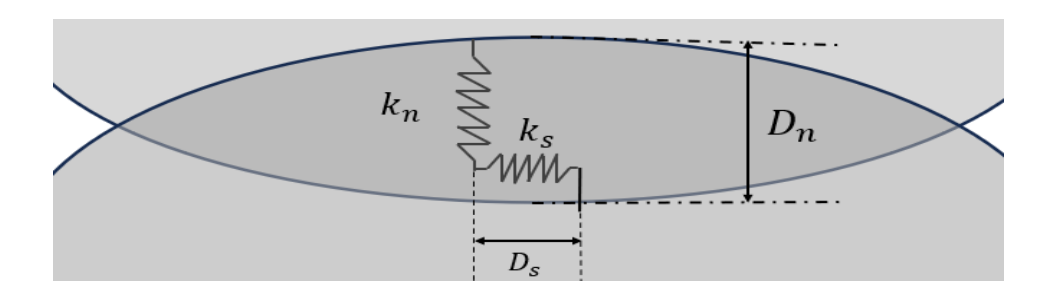


Figure 2.3.: Tangential Contact Stiffness

At a given moment and for a specific position of the overlapping particles, it is impossible to determine the value of D_s , as we do not know the path by which the particles arrived at this configuration: it could be through a purely normal trajectory (in which case we would have $D_s = 0$) or with a certain amount of tangential momentum (in which case we would have $D_s \neq 0$ but it would be unknown). Therefore, we must consider the loading history, rather than solely relying on the instantaneous configuration of the system. Assuming for now that the grains cannot rotate, we must use the following equation, analogous to (2.6).

$$\frac{dD_S}{dt} = (\vec{V_l} - \vec{V_J})\vec{S}$$
 (2.8)

With this equation, we are able to calculate the tangential force by temporal integration of the kinematics of the two grains $(\vec{V_t} \text{ and } \vec{V_j})$, meaning we can account for the loading history, provided that we have defined an initial condition for this integration. This condition is straightforward: we consider that at the moment the grains come into contact $D_s = 0$. In other words, the tangential spring is in equilibrium at the moment the grains first come into contact, and its elongation is integrated over

time based on the relative tangential movements of the grains. We can then establish a tangential contact force:

$$F_{\rm s} = -k_{\rm s}D_{\rm s} \tag{2.9}$$

This equation involves a tangential contact stiffness k_s , which is a numerical regularization parameter just like k_n . If necessary, a tangential viscous damping can also be added v_s .

2.2.5. Friction and Sliding

As in any contact between two solids, one should incorporate the concept of friction into the tangential law. This specifies an upper limit to the magnitude of the tangential force, chosen to be proportional to the value of the normal force. Thus, we define a contact friction coefficient μ , and we constrain the tangential force as follows:

$$|F_S| \le \mu |F_n| \tag{2.10}$$

To impose this condition, we proceed in a manner analogous to that used for the normal force: a tangential force is first calculated from equation (2.9) (which requires prior integration of $\frac{dD_s}{dt}$ to access D_s), and then its absolute value is compared to the upper bound $\mu |F_n|$ (which assumes F_n is previously calculated):

$$F_{S} = \begin{cases} -k_{S}D_{S} & if |-k_{S}D_{S}| \leq \mu |F_{n}| \\ sign(-k_{S}D_{S}) \cdot \mu F_{n} & if |-k_{S}D_{S}| > \mu |F_{n}| \end{cases}$$
(2.11)

In the case where $|-k_sD_s| > \mu |F_n|$, the contact transitions from "adhesion" mode to "sliding" mode takes place. In the first case, the tangential restoring force was entirely associated with the extension of the tangential spring. In the second case, it is limited by the concept of friction, and the particles slide without retaining memory of their initial adhesive contact state. The tangential spring no longer extends; otherwise, its additional elongation would increase the tangential force beyond the threshold value, according to equation (2.9). Consequently, during sliding, we gradually shift the equilibrium position of the tangential spring by setting:

$$D_S = \mp \frac{\mu F_n}{k_S} \tag{2.12}$$

The final contact law takes the form of the rheological model presented in Figure 2.4.

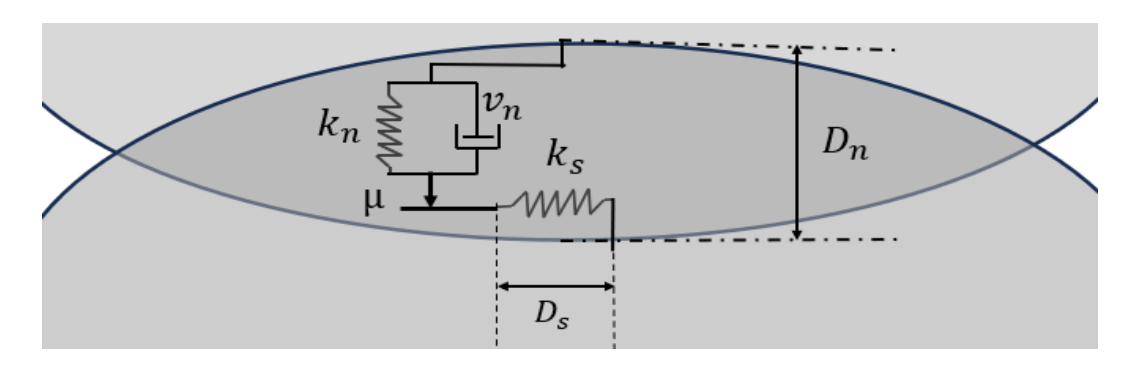


Figure 2.4.: Standard Contact Law

We have thus fully defined the standard contact law for explicit DEM. This includes two numerical regularization parameters (the normal and tangential stiffnesses) and two more physical parameters related to energy dissipation modes in the normal direction (viscous damping) and tangential direction (friction coefficient). Locally, the contact conditions are governed by the overlap distance and the elongation of the tangential spring D_s .

So far, we have made the simplifying assumption that the grains cannot undergo rotation. This assumption needs to be lifted to account for the realistic behavior of granular materials, where the concept of rolling is essential. Indeed, it is possible to have relative motion between the contacting grains while locally maintaining the condition $\frac{dD_S}{dt} = 0$, provided that, the rolling without slipping conditions are met. In this case, the relative tangential velocity is zero, and the tangential spring does not load.

In the general case, we should therefore use the angular velocities of the grains, denoted as \vec{w}_i and \vec{w}_j . For simplicity, we can assume that the grains touch at a single point denoted as C (thus following the schematic of Figure. 2.1). The relative tangential velocity of the particles at their contact point is then given by:

$$\frac{dD_S}{dt} = (\vec{V}_i - \vec{V}_j)\vec{s} - (r_i \vec{w}_i + r_j \vec{w}_j) \wedge \vec{n}$$
 (2.13)

This expression enriches equation (2.8) by taking into account the rotation of the grains. To dynamically address these rotations, it is necessary to define the torques applied to the particles by the tangential components of the contact forces. For particle i, the torque applied by the contact with particle j will be denoted as \vec{T}_i , and is given by:

$$\vec{T}_i = -(r_i. \vec{n}) \wedge (F_s. \vec{s})$$
 (2.14)

The particle rotation and the total torque $\sum \vec{T}_i$ it experiences from all its contacts are then related by a dynamic equation analogous to equation (2.1), which incorporates the inertia I_i of the particle:

$$\sum \vec{T}_i = I_i.\frac{d\vec{w}_i}{dt} \tag{2.15}$$

It should be noted that equations (2.13) and (2.14) are based on the assumption that the grains touch at a single point, which is inaccurate in the context of explicit DEM since small overlaps are allowed. This often results in a slight deviation of the simulated results from the momentum conservation. Depending on the desired accuracy, these errors can be neglected (ensuring that the normal stiffness is sufficiently large to guarantee minimal overlap and limit the amplitude of the deviation), or they can be corrected with appropriate additional terms (see [29]).

2.2.6. Rolling Resistance

The possibility of rolling without slipping was mentioned in the previous section. In classical solid dynamics, this situation corresponds to a limiting case of perfect contact where no energy is dissipated. In the context of granular mechanics, however, it is often useful to challenge this perfection by considering that two grains are not entirely free to roll over one another without dissipating energy. Therefore, rolling resistance is sometimes introduced as resisting torques applied to grains in relative rolling motion. This can serve to represent surface roughness of circular particles or even to incorporate non-circular shapes in the modeling of actual grains (which naturally oppose rolling).

The simplest method to introduce rolling resistance is to apply torques to the contacting grains that are proportional to the rolling velocity \vec{w}' and have opposite signs, which is analogous to the concept of viscous damping defined for the normal force. The relative rolling velocity \vec{w}' of two grains is defined as:

$$\vec{w}' = \frac{r_i r_j}{r_i + r_j} (\vec{w}_i - \vec{w}_j) \tag{2.16}$$

The rolling resistance could be written therefore as:

$$\vec{T}_r = -D_r.\vec{w}' \tag{2.17}$$

where D_r is the rolling damping.

This rolling resistance torque must then be introduced into the equation for the rotational equilibrium of each individual grain (Eq. 2.15). Another approach would be to define a threshold analogous to the friction coefficient μ_r , but adapted for rolling resistance. This would require, similarly to the tangential force, the use of a regulation parameter comparable to a torsional stiffness k_r positioned at the contact point.

2.3. Numerical Resolution

2.3.1. Explicit Resolution Scheme

The numerical resolution of a discrete-element modeling problem is based on the time integration of a system of ordinary differential equations, consisting of equations (2.1) and (2.15) for each particle. Several resolution schemes are available in the literature to address this type of numerical problem. For example, the explicit Newmark scheme (used notably in structural dynamics) or **Gear's predictor-corrector** scheme (used in traditional molecular dynamics). In the same framework, the **Verlet integration scheme**, also known as "**leapfrog**" is most commonly used. This scheme starts from an initial state at time $t_0 = 0$ for which all positions \vec{x}_i and velocities \vec{V}_i are known, defines a time step dt, and progresses incrementally by linearizing the equations of motion. All position and acceleration variables will be calculated at times corresponding to integer values of the time step (i.e., $t_0 = 0$, dt, 2dt, 3dt... etc.), while velocity variables will be calculated at half values of the time step (i.e., t = dt/2, 3dt/2, 5dt/2... etc.).

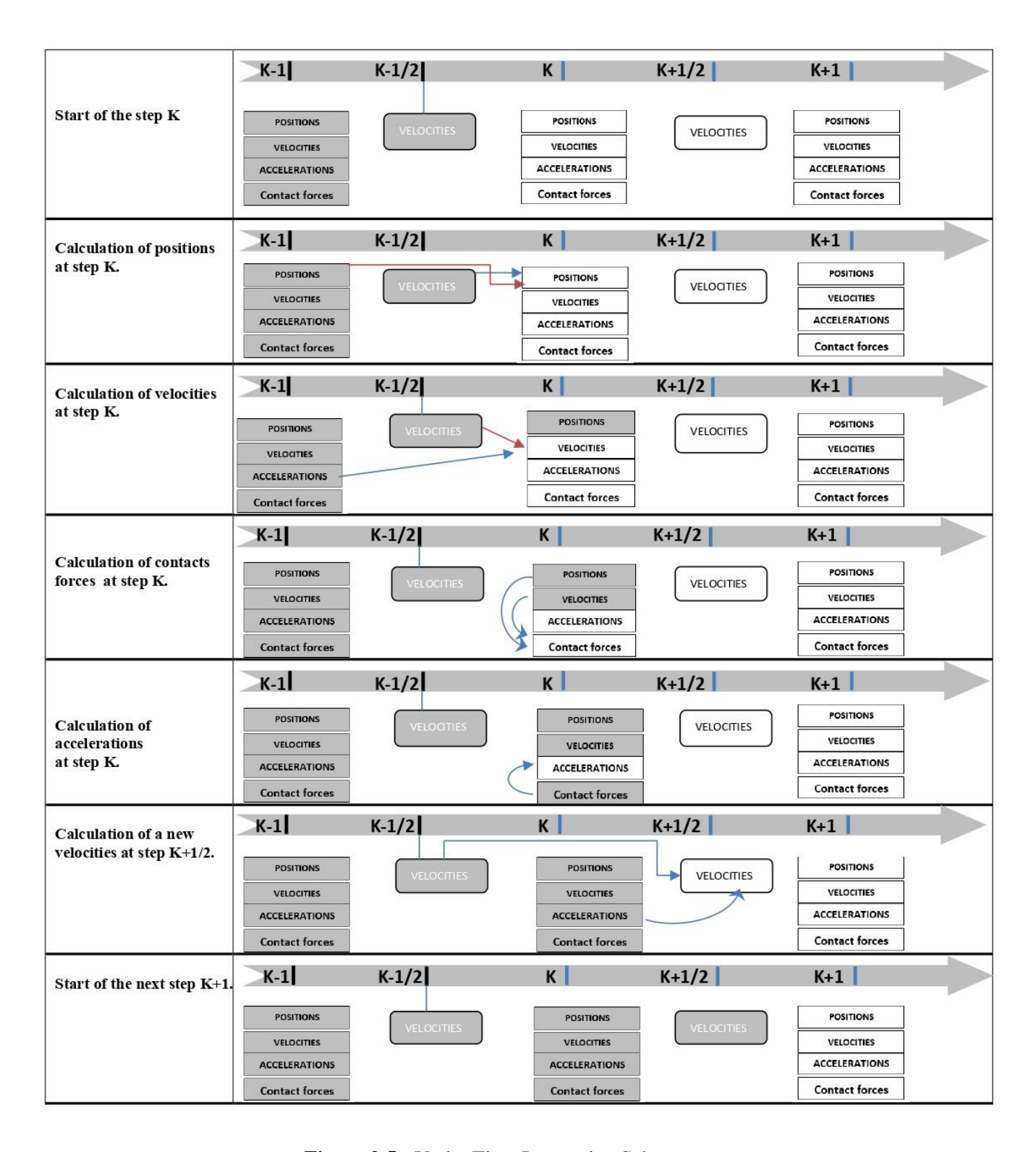


Figure 2.5.: Verlet Time Integration Scheme



In the following, we will denote the position \vec{x}_k and \vec{a}_k acceleration of a particle's center of mass at time t = kdt, and its velocity $\vec{V}_{k+1/2}$ at time $t = (k + \frac{1}{2})dt$. The rotational degrees of

freedom are treated similarly to the translational ones, although they are not detailed here for clarity. The calculations proceed by local linearization of the motion, using the following relations:

$$\vec{x}_k = \vec{x}_{k-1} + \vec{V}_{k-1/2}dt \tag{2.18}$$

$$\vec{V}_{k+1/2} = \vec{V}_{k-1/2} + \vec{a}_k dt \tag{2.19}$$

It is clear that, each quantity is calculated from quantities that strictly precede it in time, which is the definition of an *explicit scheme*. It is also noted that equation (2.19) involves the acceleration at time t = kdt, which is obtained from the fundamental principle of dynamics (2.1), thus, involving the forces applied to each grain at the same instant. These forces are calculated using the equations describing the contact law, depending notably on \vec{x}_k and \vec{V}_k .

When equation (2.19) is used, the position \vec{x}_k is known, but this is not the case for \vec{V}_k (in fact, only $\vec{V}_{k-1/2}$ is known). Before calculating the contact forces and applying (2.19), we therefore resort to the following equation over a half time step:

$$\vec{V}_k = \vec{V}_{k-1/2} + \vec{a}_{k-1}dt/2 \tag{2.20}$$

The scheme, presented in this way, provides an estimate of the new positions of the particles \vec{x}_k based on the old positions \vec{x}_{k-1} . All of these steps are summarized in Figure 2.5.

2.4. Numerical modeling Parameters

Several modeling parameters should be selected in order to perform numerical simulations. In particular, the values of the normal and tangential contact stiffnesses must be defined, as well as the time step used in the integration scheme. The normal stiffness k_n should be chosen so that the overlap distances remain small in relation to the particle diameters. For reasons of simulation speed, which will be explained later, it is also desirable that this stiffness is not too high. It is therefore not desirable to assign it an unreasonably high value to minimize overlaps; on the contrary, low values that do not produce high overlaps should be used.

The value of the normal contact stiffness is linked to the model's critical time step, which is crucial to the stability of the calculations. For stable simulations, the contact phase during the collision of two grains must be well resolved. Indeed, the integration time step must be sufficiently small in relation to the contact duration. Given the normal contact force model presented above, the collision phase of a grain with a plane could be represented by the oscillating system is presented in Fig. 2.6. This is the classic Kelvin-Voigt oscillator, obeys the following differential equation:

$$m\frac{d^2x}{dt^2} = -mg - k_n D_n - v_n \frac{dD_n}{dt}$$
 (2.21)

In this expression, the position parameter x and the interpenetration distance \mathcal{D}_n are related by:

$$D_n = x - r \tag{2.22}$$

If we denote the equilibrium position of the spring as $x_0 = r - mg/k_n$, equation (2.21) can be rewritten as:

$$m\frac{d^2x}{dt^2} = -k_n(x - x_0) - v_n \frac{dD_n}{dt}$$
 (2.23)

The grain of mass m undergoes a damped oscillation around the position x_0 , the expression of which is given by:

$$x(t) = x_0 + A. e^{s_0 t} (2.24)$$

In this expression, A represents the amplitude of the oscillation (which depends on the initial conditions), $s_0 = -\mu_0 \pm \sqrt{\mu_0^2 - \omega_0^2}$ and ω is the natural frequency. The system therefore contains two different time scales, related respectively to stiffness and damping, with characteristic frequencies given by:

$$\omega_0 = \sqrt{k_n/m} \tag{2.25}$$

$$\mu_0 = \frac{v_n}{2m} \tag{2.26}$$

Depending on the values of k_n , v_n and m, several types of behavior can occur. If $\mu_0 \gg \omega_0$ damping dominates and the system does not oscillate; it asymptotically approaches its equilibrium. In contrast, if $\mu_0 \ll \omega_0$ damping is not significant on the scale of one oscillation, and the system oscillates nearly freely with a period equal to $T=2\pi/\omega_0$.

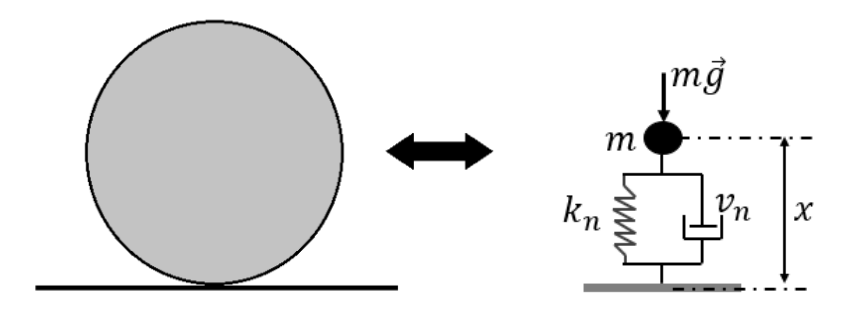


Figure 2.6.: Dynamic equivalent of a Disk Resting on a horizontal surface.

The time integration algorithm must be able to accurately resolve these small rapid movements, and the duration of the time step in the *Verlet scheme* must therefore be chosen in relation to this oscillatory motion. The following rule is generally used:

$$dt = \varepsilon \sqrt{m_{min}/k_n} \tag{2.27}$$

Values of ε close to 1/50 are commonly used, which means that the critical time step dt is chosen to discretize one period of the fastest oscillator in the system (usually corresponding to the particle with the lowest mass) into 50 successive steps.

It is clear that, as previously mentioned, it would be not reasonable to choose a normal stiffness that is too high. While this would limit overlapping, it would lead to a much smaller critical time step (since a stiffer oscillator oscillates faster), resulting in significantly higher computational costs. Therefore, one often has to strike a balance between accuracy (high k_n) and computational cost (low dt) in a simulation, similar to what is done in defining a finite element mesh.

2.5. Modeling Techniques

2.5.1. Neighborhood Detection

In the general explicit resolution algorithm for a discrete problem, update of the grain neighborhood list represent a significant portion of the computational cost of the simulation. This step involves generating a neighborhood list for each particle. This operation relies on a neighborhood detection step, which determines whether it is likely that two particles, i and j, will come into contact in the near future. The notion of "near future" is quite vague, so it is immediately clear that all neighborhood detection methods will depend on arbitrary parameters chosen by the modeler, allowing for a trade-off between computational cost and the assurance of not missing any contacts. In practice, this detection can be performed using a wide variety of methods. These methods stem from an emerging field that extends well beyond granular media, known as "computational geometry", they are commonly used in industries such as computer graphics and video games, as well as in robotics. Here, we will briefly describe only the most widely used methods in the case of circular/spherical particles.

a. Direct Method

It simply involves performing a double loop over all possible pairs of particles and selecting as likely to come into contact all pairs of particles whose distance D_n is less than a distance D_{neig} chosen by the modeler (Figure 2.7). For example, one might take $D_{neig} \cong$ the diameter of the largest

particle in the system. The direct method has the advantage of being very simple to code, but it is relatively expensive in terms of computation time.

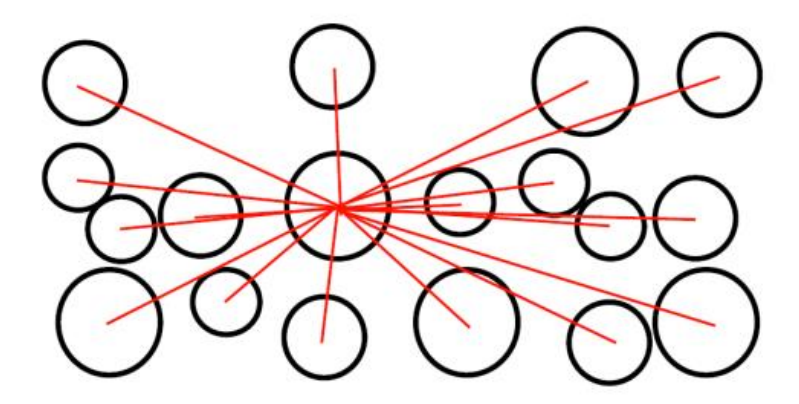


Figure 2.7. Direct Detection Method.

b. Container Partitioning Method

This method involves subdividing the entire system according to a fixed grid (in two or three dimensions depending on the problem), with a given spatial step (Figure. 2.8). Thus, each particle has its center that belongs to a "cell" with an area A (or volume V for 3D), and the identity of this cell can be easily determined from the coordinates of the center in question. Then, for a given particle, the neighborhood list consists of all particles whose centers belong to the same cell and its neighboring cells. The length of the side of the cell can be taken, for example, as $d_{cell} =$ diameter of the largest particle. This method is very efficient, except for materials that are highly polydisperse, for which it tends to form neighborhood lists that are too long. The method can also become very costly if the particles are widely dispersed in space. Nevertheless, it remains the most widely used neighborhood detection method.

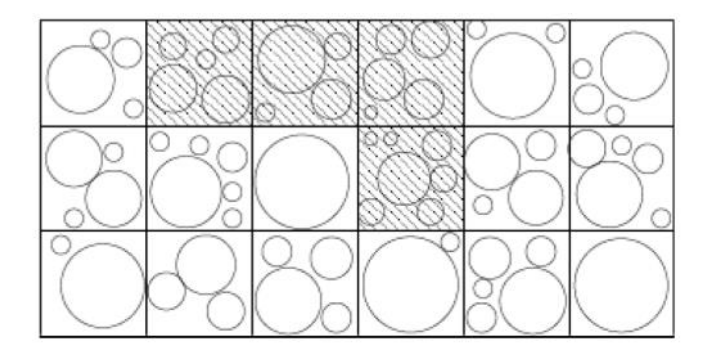


Figure 2.8.: Container dividing Method.

c. Triangulation Method

This method relies on a widely used mathematical tool known as *Delaunay triangulation* (Fig. 2.9). It is a technique that connects a set of randomly dispersed points in space using a network of triangles that are as regular as possible. This results in a tiling of space and a direct relationship between each point and its nearest neighbors. When applied to neighborhood detection, this method is appealing but has the drawback of being computationally expensive, and it may sometimes fail to capture certain neighborhoods if the sample is highly polydisperse. Therefore, it is rarely used in the context of Discrete Element Method (DEM).

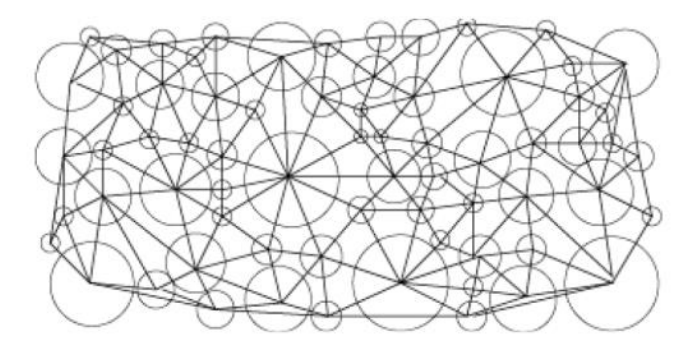


Figure 2.9.: Delaunay Triangulation Method.

It should also be noted that, in addition to the neighborhood detection technique and its potential numerical parameters, the modeler must be very mindful of the frequency at which this operation is performed. This frequency primarily depends on the type of simulation being conducted. If the situation involves grains that move little (quasi-static loading), it is possible to considerably space out the updates of the neighborhood lists, which are generally costly. In contrast, in a highly vibrated medium or disordered flow situation, the geometric configuration of the system evolves very quickly, and this update will need to be more frequent. Therefore, the trade-off between time savings and the risk of missing a collision is a choice made by the modeler.

2.6. Generation of an Initial State (samples creation)

This involves creating a sample that meets the granular material's target conditions in terms of particle size distribution, solid fraction, state of stress, and so on. This is not a trivial problem, however, it can be broken down into two different parts.

On one side, we focus on the positions and diameters of the particles, which allow us to meet the general shape criteria of the sample, particle size distribution, and solid fraction. These are essentially geometric quantities that do not involve mechanics in their definition. Methods based solely on geometry can be used to solve this part of the problem.

On the other side, we focus on the contact forces in the initial sample, which allows us to meet the criteria for the stress state. The presence of contact forces implies the concepts of overlap, contact laws, loading history,... etc. Thus, it appears that, from this perspective, In a recursive manner, the establishment of the stress state of an initial sample for discrete simulation can only be achieved through a prior discrete simulation. However, it is not necessary for this simulation to start from a well-controlled initial state; only its final state is important. The overall approach is therefore as follows:

- 1 Generate an initial sample (positions and diameters of all particles) using a geometric method in the absence of contact.
- 2 Perform a discrete simulation of this sample under certain loads to achieve the desired stress state.
- 3 Finally, perform the desired simulation on this well-controlled sample.

Each of steps 1 and 2 can be extremely costly in terms of computing time, even if they do not yet represent the desired simulation (step 3). Consequently, the aim is generally to use a geometric method (step 1) that limits costs while providing a sample very close to the desired state, thus minimizing the cost of step 2. We will briefly introduce some of these geometric methods

a. Implementation on a Fixed Grid

This method the simplest and fastest of all (Figure 2.10) (it is adopted in this thesis). It involves positioning the centers of the particles on a fixed grid (with rectangular or hexagonal cells), ensuring that the grid spacing is greater than the diameter of the largest particle. This ensures that no overlap occurs in this initial state. The resulting solid fractions are extremely low (especially for highly polydisperse samples), which means that the next step of compacting this sample is always very costly. Therefore, more sophisticated techniques are generally preferred.

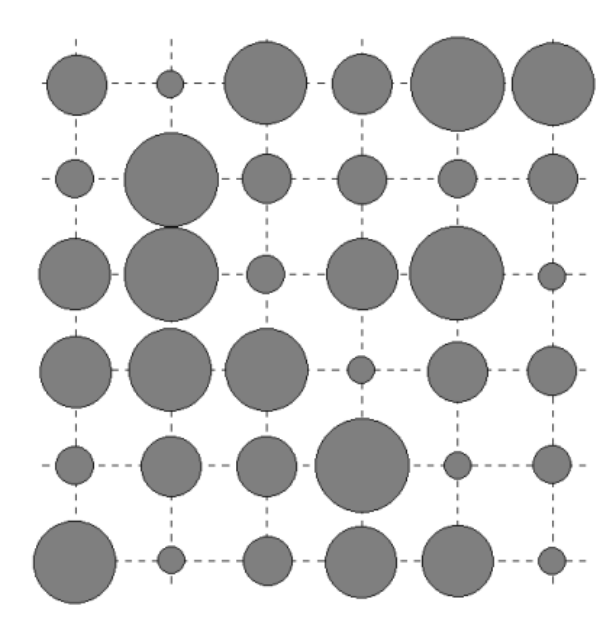


Figure 2.10.: Packing on a Square Grid.

b. Random positioning

This method consists of placing the grains one by one at a random point in the container, ensuring that each time a particle is placed, it does not overlap with the particles already placed. If an overlap occurs, the position is rejected, and another random position is proposed for the particle, followed by a new test, and so on. This method is interesting, especially if care is taken to place the particles in decreasing order of size. However, it can be extremely costly if the sample is large (as each new particle must be tested for overlap with all previous particles), and if a high solid fraction is targeted (the empty spaces become increasingly rare, and the probability of a valid random placement decreases rapidly). Nonetheless, some recent techniques based on the concept of level sets can make these methods very appealing.

c. Constraint Voronoi Partition

It is a method based on creating a constrained *Voronoi partition* of the container to perform the packing (Figure. 2.11). The Voronoi partition is a mathematical tool (conceptually very close to Delaunay triangulation), which divides space into as many polygonal regions (polyhedral in 3D) as there are points, based on a set of points arbitrarily positioned in space. In particular, the polygon corresponding to a given point in the initial point cloud is made up of all the points in space that are closer to this point than to any other point in the initial cloud. Such a polygon/polyhedron is called a "Voronoi cell". A judicious placement (which can be achieved through various methods) of the points in the initial cloud allows for very precise control over the size distribution of the cells. Each cell can

then be filled with a grain, and the particle size distribution will replicate that of the cells. This method has certain analogies with the grid technique but allows for much denser packings.

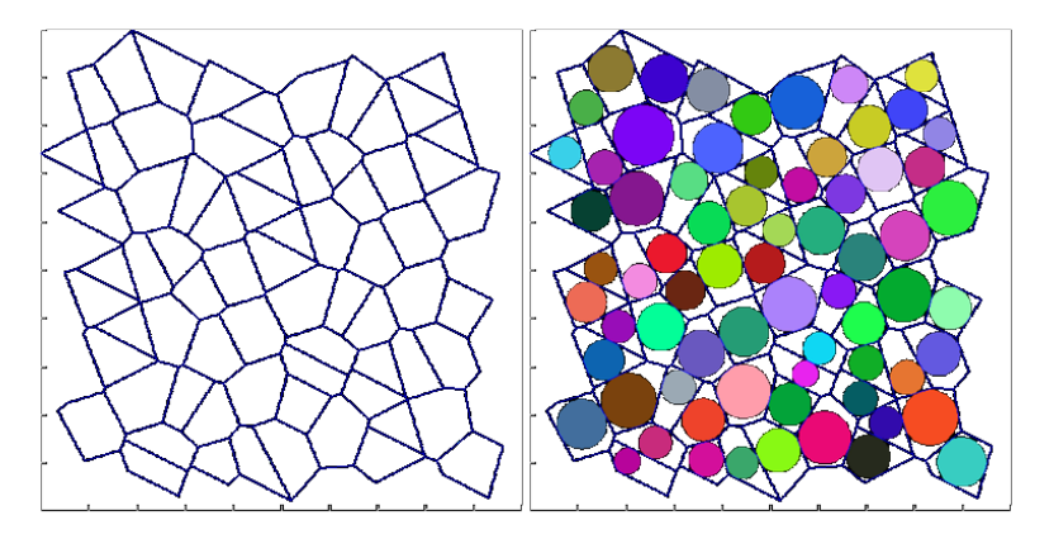


Figure 2.11.: Voronoi Partition and Filling of Cells with Circular shaped Grains.

2.7. Boundary condition

In discrete element modeling (DEM), boundary conditions play a crucial role in simulating the mechanical behavior of materials accurately. Commonly used boundary conditions include rigid friction walls, rigid frictionless walls, periodic boundaries, and flexible membranes [30].

Rigid walls with friction are often used to simulate confinement, providing a positionally controlled edge that can resist shear forces, thus influencing the stress distribution within the material. In contrast, frictionless rigid walls are position-controlled edges that allow particles to slide freely along the edge, which is useful for simulating ideal conditions where friction is negligible. Periodic boundary conditions are utilized to replicate an infinite medium by allowing particles exiting one side of the simulation box to re-enter from the opposite side, effectively minimizing edge effects and enabling the study of bulk material properties. Flexible membranes have gained attention for their ability to mimic real-world scenarios where boundaries can deform under stress. This approach allows for more realistic simulations of materials that experience significant deformation, such as granular materials under triaxial testing. The integration of flexible membranes into DEM not only enhances the accuracy of simulations but also facilitates the investigation of complex behaviors like particle breakage and shear localization, which are critical in understanding granular material mechanics under various loading conditions. By combining these boundary conditions thoughtfully, researchers can create more robust models that better reflect the physical phenomena observed in experiments.

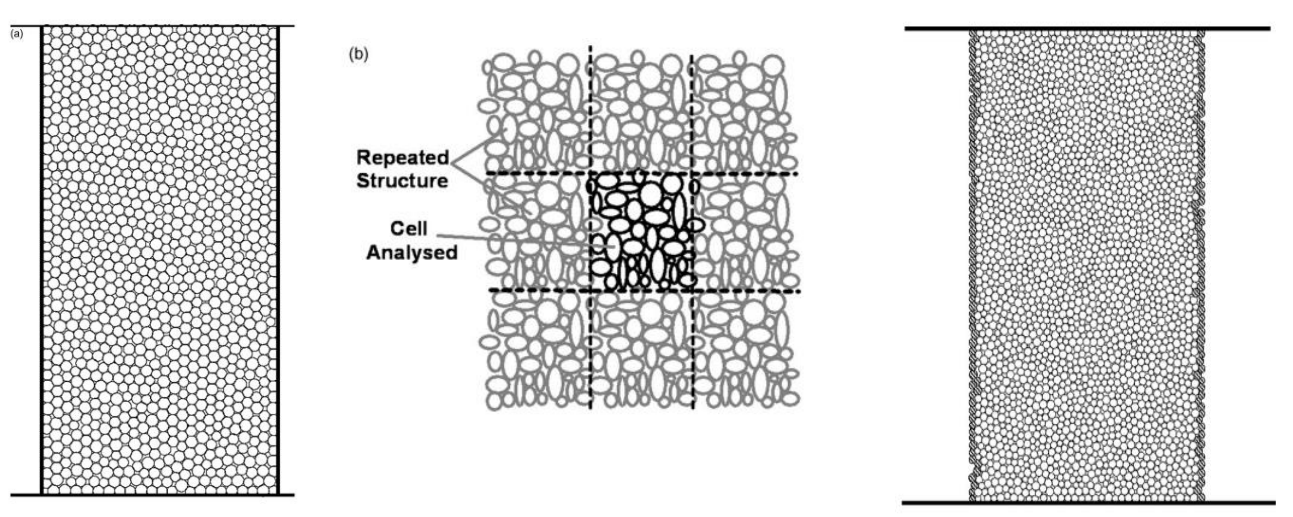


Figure 2.12 Illustration of rigid, periodic and flexible boundaries used in DEM simulations.

(a) Rigid boundary illustration; (b) periodic boundaries (c) flexible boundary [30]

2.8. Representative Elementary Volume

It is generally accepted that the mechanical behavior of a granular material can be assimilated to that of a continuous medium, with behavior defined at each point by a macroscopic constitutive law relating strains to stresses. For this reason, laboratory tests (triaxial, oedometer, etc.) are conducted on soil samples containing a sufficient number of grains, whose size must be small relative to the size of the sample. Obviously, this precaution must also be verified in discrete numerical simulations. One must ensure, by using a sufficient number of particles, that the dimension of the heterogeneities is small compared to the dimensions of the assembly as well as to the applied loading. However, as pointed out by Chareyre 2003 [31], what does "sufficient" mean? How can one assess the validity of simulations?

In the context of studies on heterogeneous materials using multi-scale approaches, this generally translates into defining a Representative Elementary Volume (REV). It is termed "elementary" because it is considered as a material point of the medium, and "representative" because it exhibits mechanical behavior identical to that of the equivalent macroscopic medium: it is the smallest volume for which, according to Cambou and Jean (2001) [32], it is possible to determine a unique behavior law linking stresses to strains. This definition of REV, based on the uniqueness of the behavior, is hardly conceivable in the context of discrete simulations. Indeed, how can one characterize the unique behavior of a granular assembly knowing that, inevitably, the specific initial configurations of a simulation generate as many corresponding "exact" solutions? Variability is inherent in discrete methods, regardless of errors related to the resolution method.

Thus, several authors [32] have focused on characterizing the REV and have attempted to estimate the minimum number of heterogeneities to consider. For instance, based on experimental tests on Schneebeli rolls, [34], showed that, calculating global deformations from the discrete displacement field (also known as kinematic homogenization) depends on the size of the domain over which the calculation is performed. They estimate satisfactory convergence of calculations towards experimentally measured values from a volume equal to ten times the size of the largest element, which would correspond to the REV and confirm analyses already conducted in reference [23]. Nevertheless, because of the variability inherent in the discrete element method (DEM), characterizing the REV on the basis of the dispersion of results seems the most relevant, since it is well established that this variability decreases with increasing particle number, an asymptotic behavior being evidenced in large systems. In [32] for example, it is demonstrated that in two-dimensional simulations, the standard deviation calculated from peak stress values decreases with the number of grains N involved, proportionally to $N^{-1/2}$.

This probabilistic approach has ultimately led experimenters and numerical analysts to characterize the Representative Elementary Volume (REV) based on the results of their simulations: the number of grains to be considered is determined by the fact that differences become negligible from one test to the other. Several samples of the same material must be able to reproduce equivalent mechanical behaviors. This equivalence, of course, is left to the experimenter's judgment. However, in the context of numerical simulations, it's important to bear in mind that the computational cost is directly related to the number of interacting particles.

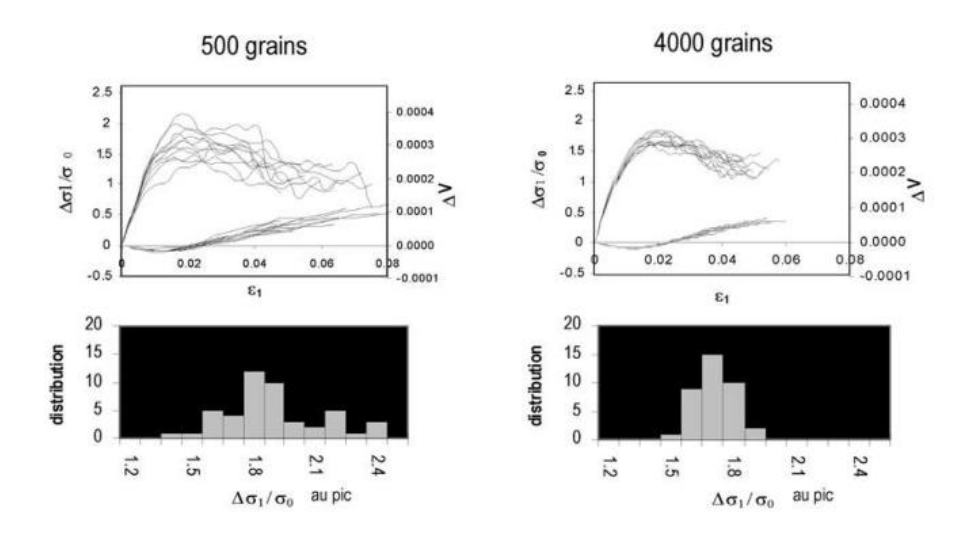


Figure 2.13 Dispersion of the σ - ϵ curves for two samples with identical properties of 500 and 4000 grains subjected to biaxial loading according to [31].

2.9. Usual grain shape models

In DEM, the classical grain shape used is disk in 2D and spherical shaped grains in 3D to optimize computation times during contact detection. In [35], it is shown that these models do not quantitatively reproduce the shear resistance of a non-cohesive soil subjected to triaxial tests. The rolling mechanisms that may develop with spherical elements reduce the shear resistance. Matsushima and Saomoto (2002) [36], showed that more angular elements can increase shear resistance without the mechanism being clearly identified. Several methods have been proposed to address the rolling of grains. These methods are either based on the use of non-spherical elements, which may or may not be convex, or they incorporate specific contact laws that result in partial or total locking of the elements rotations. In contrast, on models composed of spherical elements, the normal contact forces generated within assemblies of non-spherical convex elements contribute to the creation of moments. Many authors have developed 2D polygonal elements, such as [37] or [38], who varied the elongation of the elements and demonstrated that, in contact dynamics, elongated polygons help to limit rotations within the sample. In [39], more complex 2D assemblies of elements whose shape can evolve from a circle to a triangle or a square are proposed, while [40] develop 3D element shapes initially composed of spheres but made convex. These authors develop specific algorithms for contact detection, but no mechanical tests are conducted on these assemblies, and no indication is given regarding the possible anisotropy of the medium. [41] conducted biaxial tests (using a 2D model) and triaxial tests (using a 3D model). The shapes of the tested elements are disks and oval shapes in 2D, and spheres and elongated or flattened spheroids in 3D. they observed that samples composed of perfectly symmetrical shapes (disks and spheres) exhibit lower resistance.

Disk

Sphere

Emeriault and Claquin (2004)

Grain shapes with rolling resistance contacts laws

Contacts laws

Table 2.1. Usual grain shape models.

2.10. Conclusion

In conclusion, this chapter provided a comprehensive overview of the Discrete Element Method (DEM), highlighting its fundamental principles and applications in the study of granular materials. We began with a general description of the DEM, emphasizing its capability to simulate the behavior of discrete particles and their interactions. We explored various contact models that are essential for accurately representing the interactions between particles, including the mechanisms of rolling resistance that influence the behavior of granular assemblies.

The methods for creating representative samples were discussed, illustrating how sample preparation can significantly impact the results of DEM simulations. Boundary conditions play a crucial role in defining the behavior of the modeled system, we presented different approaches to implementing these conditions effectively. Additionally, we addressed the concept of representative volume elements, which is important for ensuring that simulations reflect the characteristics of larger systems. Finally, we reviewed the common grain shapes utilized in DEM, noting how these shapes affect particle interactions and overall system behavior.

Chapter 03

A STICK-SLIP FRICTION MODEL FOR DISCRETE ELEMENTS MODELING

3.1. Introduction

The discrete element method (DEM) is a numerical technique used to simulate the behavior of granular materials by modeling each particle as a discrete entity with its own position, velocity, and contact forces. For the intergranular contact treatment two distinct methodologies can be distinguished, the soft-contact approach [27] and the hard-contact approach [42, 43]. In the soft-contact approach, the particles are modeled as pseudo-rigid bodies with deformation mainly occurring at the contact point, allowing a small particle deformation referred as overlap. This latter is then used to calculate the contact forces modeled via rheological models selected to reproduce the overall behavior of granular media in a given context [44–47].

Intergranular tangential forces are governed by intergranular friction which has a determinant effect on the macroscopic behavior of the simulated material [48–50]. Therefore, the development and calibration of friction models in DEM are essential to ensuring the fidelity and effectiveness of simulations in studying granular systems and complex particle interactions. In this context, many friction models are developed, some of these models are based on Coulomb friction laws [27, 51–53] and others on elastic Mindlin's theory [54–56].

In this chapter we present the dry friction model extended to the stick-slip behavior commonly observed in systems characterized by friction coefficients different in static and dynamic regimes. First, the model is formulated and implemented in a 2D discrete element model. Then, three examples involving a static, quasi-static and dynamic situations are modeled and analyzed in detail to show the effectiveness and robustness of the model.

3.2. Stik-slip motion

When two surfaces are in contact, they are effectively in contact only in certain areas, called asperities [57, 58], Fig. 1, 2. The junctions created by the contacts at the level of the asperities have two behaviors during shearing motion.

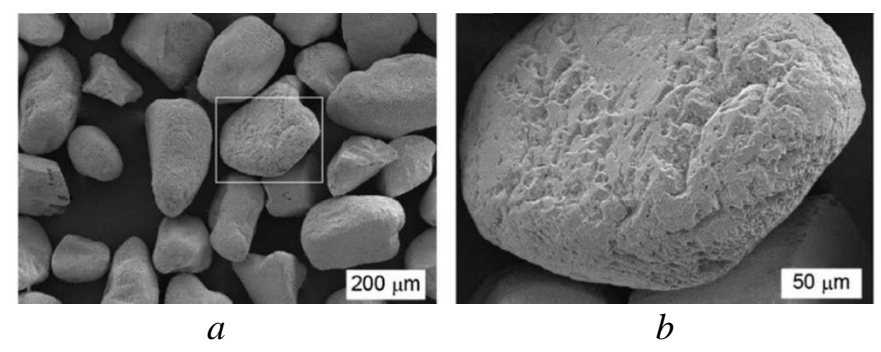


Figure 3.1. Ottawa sands: a – SEM photomicrograph, b – an enlargement image of the framed area in (a) [59]

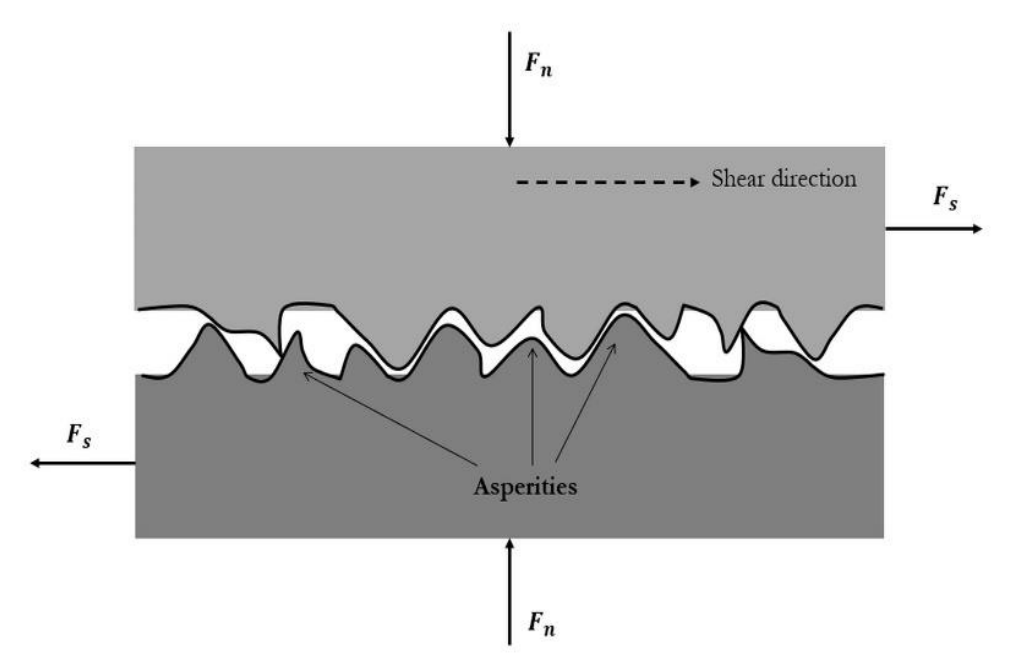


Figure 3.2. Schematic view of the microscopic contact of tow surfaces: F_n – Normal forces, F_s – shear forces

Stick stage: Under the effect of an external force of small amplitude, the links stretch and allow a microscopic relative displacement between the two surfaces in contact. This deformation is «reversible», therefore, if the external force cancels, the deformation disappears, the two solids resume their relative starting position.

Slip stage: Under the effect of external force of amplitude greater than coulomb's threshold $\mu_s F_n$, called the «breakaway force», the deformation is irreversible, the connection created by the asperities break and relative sliding occurs.

Stick-slip motion is characterized by a sawtooth displacement-time evolution. Fig. 3 illustrates the static phase and the kinetic phases involving the stick-slip phenomenon. The motion is bonded by the static friction force $\mu_s F_n$ in the stick phase and the kinetic friction force $\mu_k F_n$ in the slip phase. Where μ_s and μ_k are respectively the static and the dynamic friction coefficients with $\mu_k < \mu_s$.

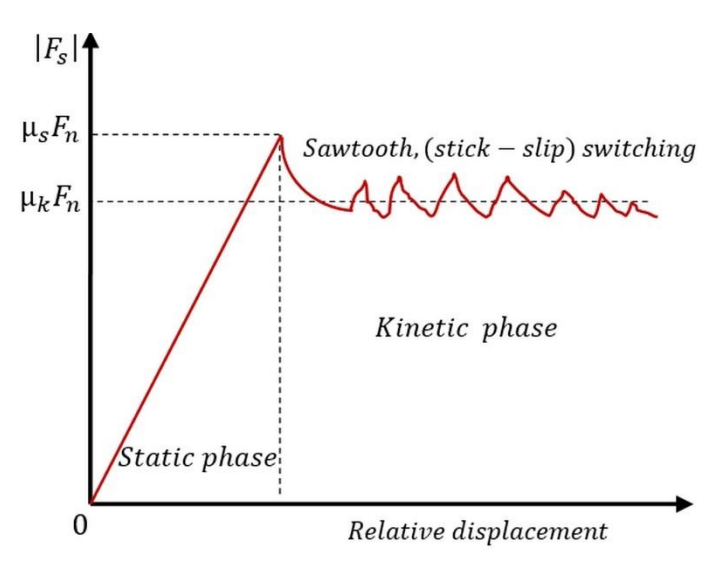


Figure 3.3. Illustrative scheme of stick-slip behavior

A number of factors affect the Stick-slip phenomenon. The most important factors are: the shear velocity and the quantity and nature of asperities of the contact surface. The shear velocity V_s has a very important effect on the frictional force. The experiments show that the average friction force F_s depends on the shear rate. Typically, F_s decreases as V_s increases as shown in Fig. 4.

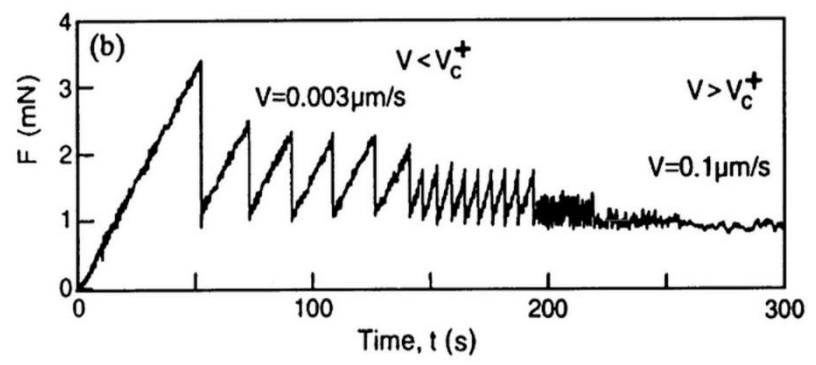


Figure 3.4. Typical evolution of friction force in terms of shear velocity V_c^+ being the critical shear velocity [60].

The critical shear velocity V_s^c is defined as the velocity beyond which the friction force

disturbances due to stick-slip become negligible, above this velocity the relative surfaces motion is referred to as steady sliding [60–64].

3.3. Usual contact models in DEM

In 2D simulation of granular media composed of circular-shaped particles, each grain i is defined by its mass m_i , radius r_i and position $\overrightarrow{x_i}$ and the same for grain j, the deformation of the grains is parametrized by the overlap $D_n = (\overrightarrow{x_i} + \overrightarrow{x_j}) - (r_i - r_j)\overrightarrow{n}$ (Fig. 5). The dynamics of a grain i is governed by second Newton's law, where the equations of translation and rotation are integrated involving all external forces acting on this grain such as contact forces and gravity:

$$m_{i}\overrightarrow{x_{i}} = \overrightarrow{F_{ii}^{c}} + m_{i}\overrightarrow{g} \tag{3.1}$$

The contact force $\vec{F}_{ij}^{\vec{C}}$ defined as the action of the grain j on the grain i can be decomposed into normal and tangential components, \vec{F}_n and \vec{F}_s respectively:

$$\overrightarrow{F_{U}^{C}} = F_{n}\overrightarrow{n} + F_{s}\overrightarrow{s} \tag{3.2}$$

where \vec{n} is the normal unit vector pointed from i to j, and \vec{s} is the tangential unit vector obtained from $a+90^{\circ}$ rotation of \vec{n} .

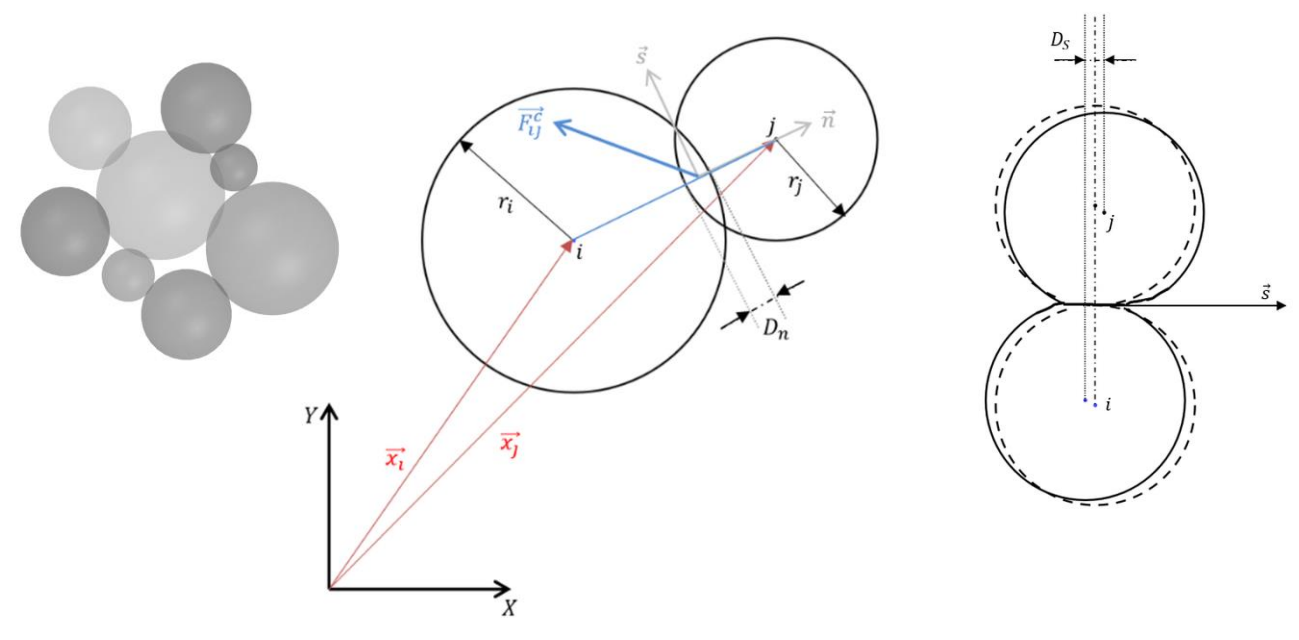


Figure 3.5. Soft-contact particles interaction

For the normal component, particles collusion is commonly modeled with linear visco-elastic model. Where the contacting grains are treated as a harmonic damped oscillator having an effective masse equals to $m_i m_j / (m_i + m_j)$. The natural half-period of this oscillator is considered as the contact duration T_C . This latter is discretized into small time steps dt in order to properly resolve the contact evolution.

Thus, $\overrightarrow{F_n}$ is the sum of the elastic and damping forces:

$$\vec{F}_n = (D_n K_n + \nu_n V_n) \vec{n} \tag{3.3}$$

where K_n is the normal stiffness of the spring and V_n is the velocity of grain i relative to grain j velocity given by:

$$V_n = (\overrightarrow{x_l} - \overrightarrow{x_l})\overrightarrow{n} \tag{3.4}$$

more details about normal force modeling are presented in references [56, 65–68].

The tangential component $\overrightarrow{F_s}$ is often represented by models based on Coulomb's law, due to their simplicity of implementation and short computational time. For dynamic problems, the linear model is the most representative. This model assumes that the frictional force is proportional to the normal contact force according to Coulomb's law. the disadvantage of this model is that the tangential

force becomes undefined if the interparticle shear velocity is zero $(\vec{V_s} = \vec{0})$. For static or quasi-static problems tow models was distinguished. The visco-plastic model and visco-elastic friction model in both the tangential force was limited by coulomb threshold, beyond this threshold an intergranular slip occurs. These models are summarized in Table 1.

Rheologic model	Description	References
	Coulomb friction model: $\vec{F}_s = \mu F_n sign(\vec{V}_s)$ $\mu = \mu_k$, where \vec{V}_s – relative shear velocity	[69–71]
	Visco-plastic model: $\overrightarrow{F}_s = \min(v_s V_s ; \mu F_n) sign(\overrightarrow{V_s})$ $\mu = \mu_k$	[66, 72, 73]
	Visco-elastic model: $\overrightarrow{F}_{s} = \min(K_{s}D_{s} + v_{s}V_{s} ; \mu F_{n})$ $sign(K_{s}D_{s} + v_{s}V_{s}),$ where v_{s} – damping coefficient	[52, 53, 74–76]

Table 3.1. Usual friction model.

3.4. Stick-slip friction model

In this section, the tangential contact model and the calculation algorithm during a contact evolution will be presented in detail. The tangential force is modeled by an elastic spring with a dashpot in series with a slider (Fig. 6). The elastic spring allows to simulate the deformation or the reversible phase (*stick phase*) and the slider defines the Coulomb's threshold characterized by different friction coefficients in static and dynamic regimes.

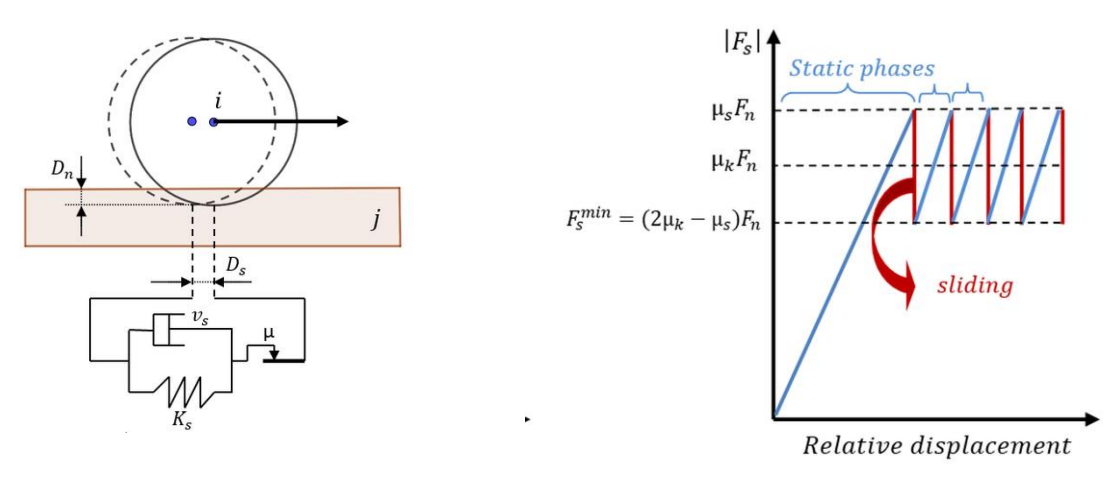


Figure 3.6. Stick-slip friction model

As mentioned in subsection 2.1, stick-slip motion has static and dynamic phases. In the static phase the stick force remains below the coulomb's static threshold $F_s \leq \mu_s F_n$ and the spring deformation is equal to the relative tangential displacement D_s . Therefore, the tangential force is computed as the sum of the elastic force and the viscous force:

$$\overrightarrow{F_s} = (-D_s K_s - v_s V_s) \overrightarrow{s} \tag{3.5}$$

where K_s is the tangential spring stiffness and V_s the relative tangential velocity:

$$\vec{\mathbf{V}}_s = (V_j - V_i)\vec{s} \tag{3.6}$$

During contact evolution D_s increases at each time step (dt) so that:

$$D_s = \sum_{dt} V_s dt. (3.7)$$

Once the tangential force exceeds the Coulomb's static threshold $F_s \ge \mu_s F_n$ the kinetic phase is activated and F_s set to F_s^{min} . In this moment the spring deformation should be adjusted to conform the kinematic friction force:

$$D_s = \frac{F_s^{min}}{K_s}. ag{3.8}$$

Immediately another stick phase will be activated. It should be noted that the lower limit of the friction force F_s^{min} during the stick-slip motion is chosen $(2\mu_k - \mu_s)F_n$ so that the average tangential force is equal to $\mu_k F_n$.

The model implementation can be done according to the diagram in Fig. 7. This diagram indicates that calculation of the shear force begins from the moment contact begins, i. e. $(D_n < 0)$. At this moment, contact duration and shear deformation are initiated to zero (t = 0 and $D_s = 0$). During the contact, the algorithm checks if the stick force is less than the static threshold; if so, it calculates the static friction force using the tangential deformation and maintains the state as «sticking».

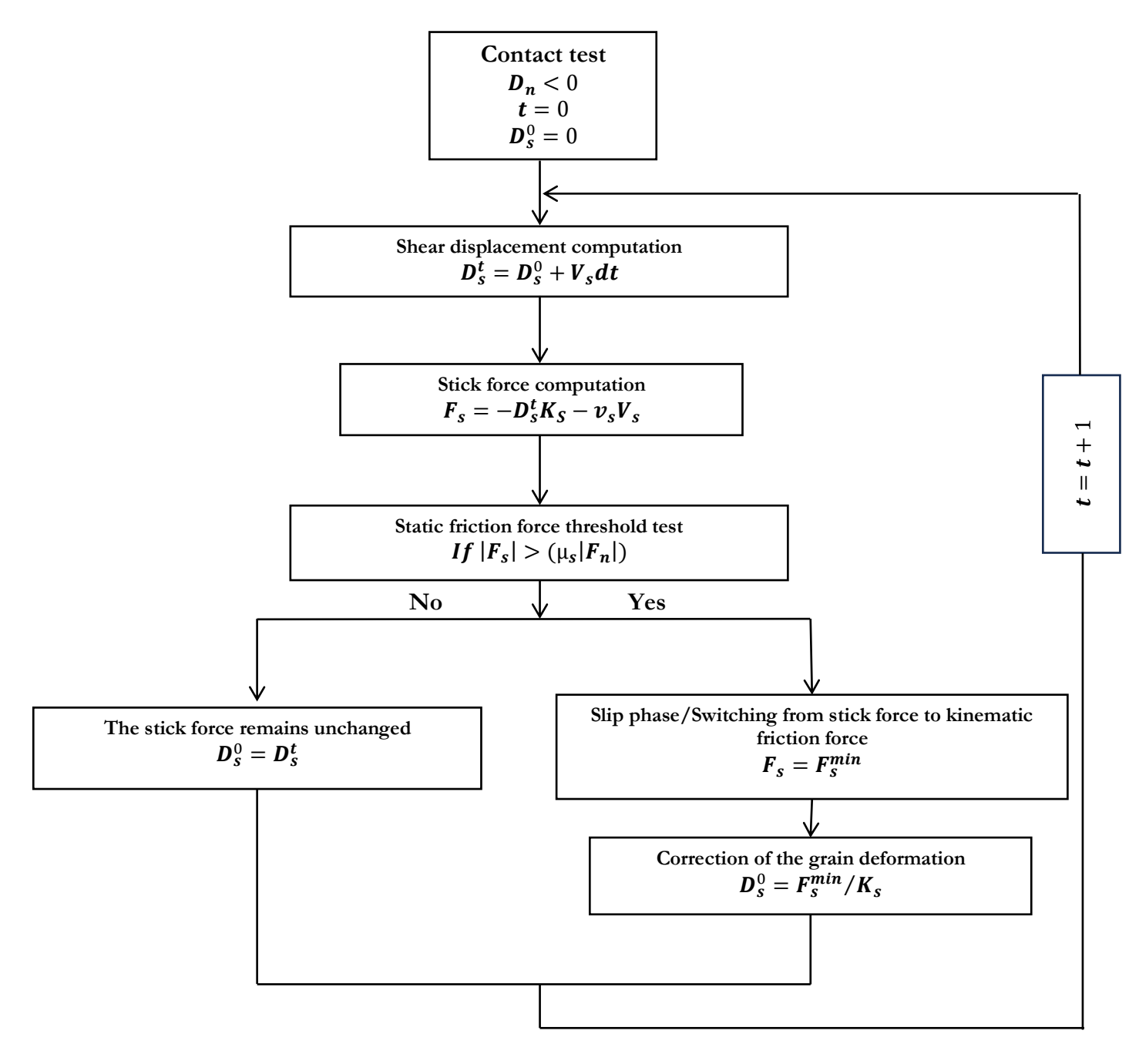


Figure 3.7. The diagram of the model implementation

When the stick force exceeds the static coulomb's threshold, the algorithm transits to the slipping phase, where it calculates the friction force using the dynamic friction coefficient, the friction force drops below the dynamic threshold again, the system returns to the sticking phase. This process is repeated for as long as the contact continues. The Coulomb slip threshold evolves with time, since it depends on the normal contact force, which varies with time.

3.5. Simulations and Discussion

It should be mentioned that, in the following examples, the grains motion is assumed to be a pure translation without rolling, so that the sliding velocity equals to the translational velocity. These examples allow to highlight the friction force evolution.

The common parameters for all simulations are summarized in Table 3.2.

Characteristics	Symbol	Value	Unite
Normal stiffness	K_n	12000000	N/m ²
Tangentiel stiffness	K_s	9600000	N/m ²
Normal viscous damping coefficient	V_n	41.38	kg/s ⁻¹
Tangentiel viscous damping coefficient	v_s	33.10	kg/s ⁻¹
Static friction coefficient	μ_s	0.5	_
Kinetic friction coefficient	μ_k	0.45	_
Gravity	g	9.81	m/s ²
Density of grains	ρ	2600	kg/m ³

Table 3.2. Simulations parameters.

3.5.1. Quasi-static example

A basic example which shows the stick-slip phenomenon consists on a grain translation on a planar surface (Fig. 8), the grain i has a radius r = 0.002 m and mass m_i , it is supported by a planar surface and subjected to a constant horizontal velocity (V=0.00001 m/s), this velocity is selected relatively small in order to observe the stick-slip phenomenon.

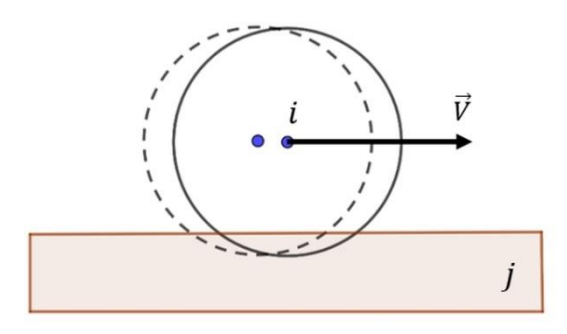


Figure 3.8. Circular shaped grain translating on a planar surface

The friction force and the grain's slippage evolution as function of the relative displacement

between the grain and the planar surface are shown in Fig. 9. For the friction force plot, two main phases are distinguished, a static phase and dynamic phase. In the first one, the relative displacement equals to the grain deformation without sliding. In this case, the friction force increases linearly until reaching the coulomb's static threshold $\mu_s F_n$. In the dynamic phase, the stick-slip phenomenon occurs where the frictional force switches between the static limit $\mu_s F_n$ and the dynamic limit $(2\mu_k - \mu_s)F_n$. During the sticking periods, the frictional force increases linearly to reach the static friction limit, as described in phase 1. However, when F_s reaches the static frictional limit, the grain starts to slip and the frictional force drops to the dynamic friction limit. This drop in frictional force is represented by a vertical line segment in the graph.

As mentioned in the description of the model, the lower limit of the friction force F_s^{min} during the stick-slip motion is chosen so that the average tangential force is equal to $\mu_k F_n$.

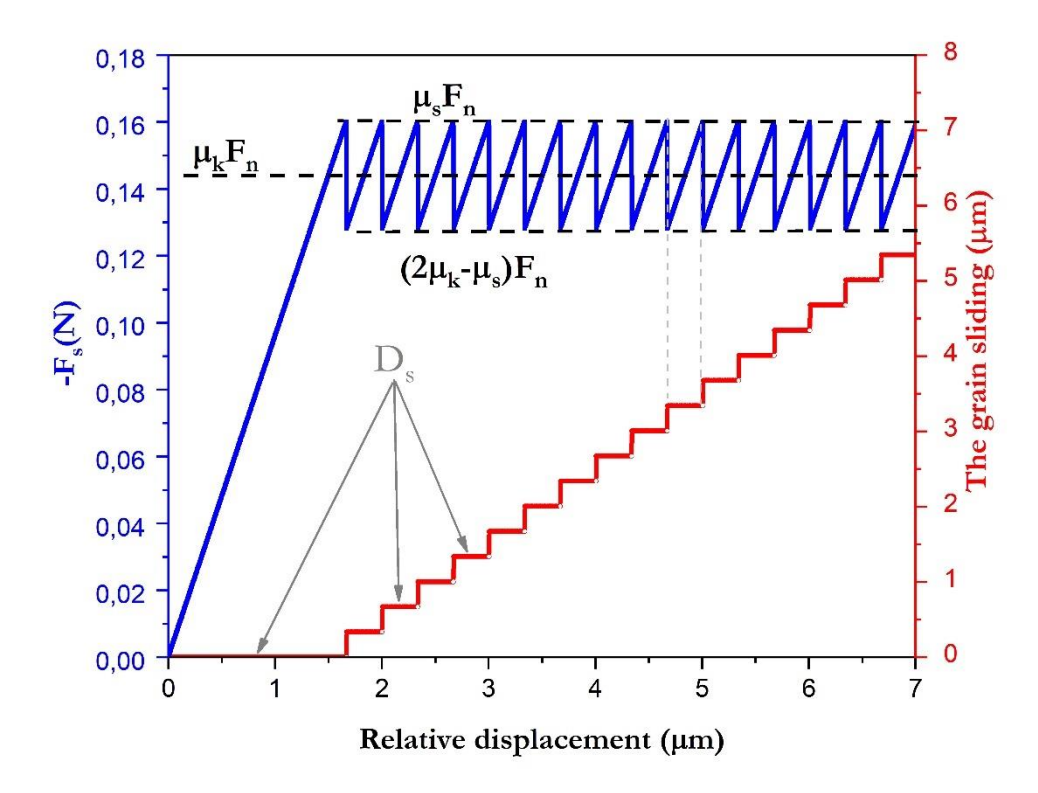


Figure 3.9. The friction force and the grain sliding evolution

During translation, it is noticed that the grain makes sliding jumps presented on the graph by vertical segments (slip segments), and deformation phases presented by horizontal segments (stick segments). during the stick phase there is no sliding between the grain and the planar surface and the

friction force increases linearly as the deformation increases.

3.5.2. Static example

In order to highlight the differences between the friction models presented in subsection 2.2, a simple static problem is simulated. In this problem, two circular particles denoted 1 and 2, with equal radii $r_1 = r_2 = 0.005$ m and masses $m_1 = m_2$, are placed in a rectangular tray (Fig. 10). The length L of the tray is less than the sum of the diameters of the two grains $L < (2r_1 + 2r_2)$. In addition, since the grains are slightly deformable, L is selected sufficiently large so that the normal forces alone cannot support the weight of grain 1.

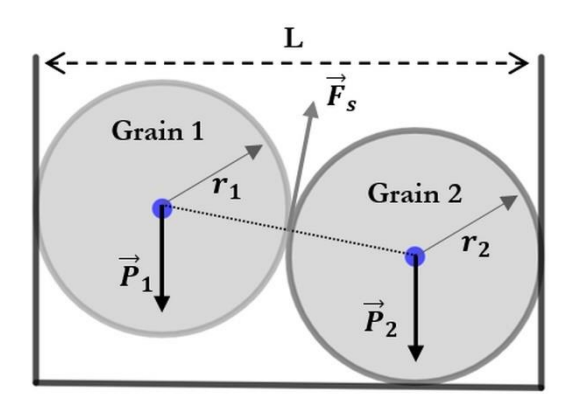


Figure 3.10. Schematic illustration of the static example

Initially, the grains are placed almost in contact. At the instant t = 0, the acceleration of gravity is applied to the system, therefore, the grain 1 moves downwards and the contact forces between the grains develop.

The evolution of the vertical position of the grain 1 for different friction models is shown in Fig. 11.

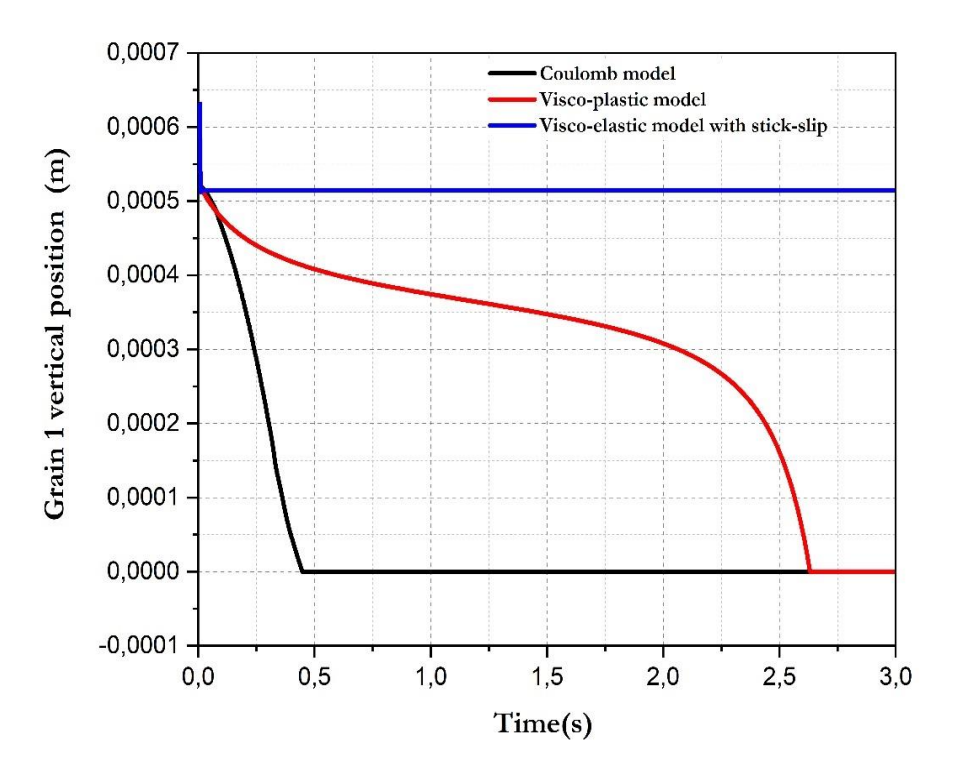
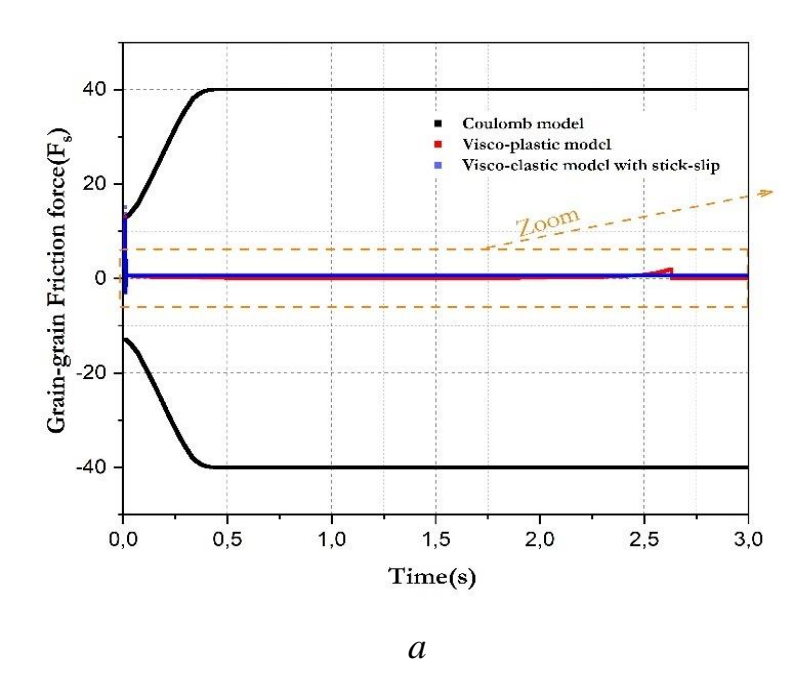


Figure 3.11. Vertical position of the grain 1

It can be observed that both models (coulomb model and the visco-plastic model) exhibit a nonrealistic behavior, in fact the grain 1 can't be supported by the friction forces and reaches at the end the bottom of the tray. Note that the grain displacement has different paths for these two models. Contrarily, for the viscoelastic model with stick-slip, shows a more realistic behavior where the grain 1 is supported by the contact forces in a position above the bottom of the tray.

In order to understand the observed behaviors, the evolution of the grain-grain tangential force with time is plotted in Fig. 12 for the three models.



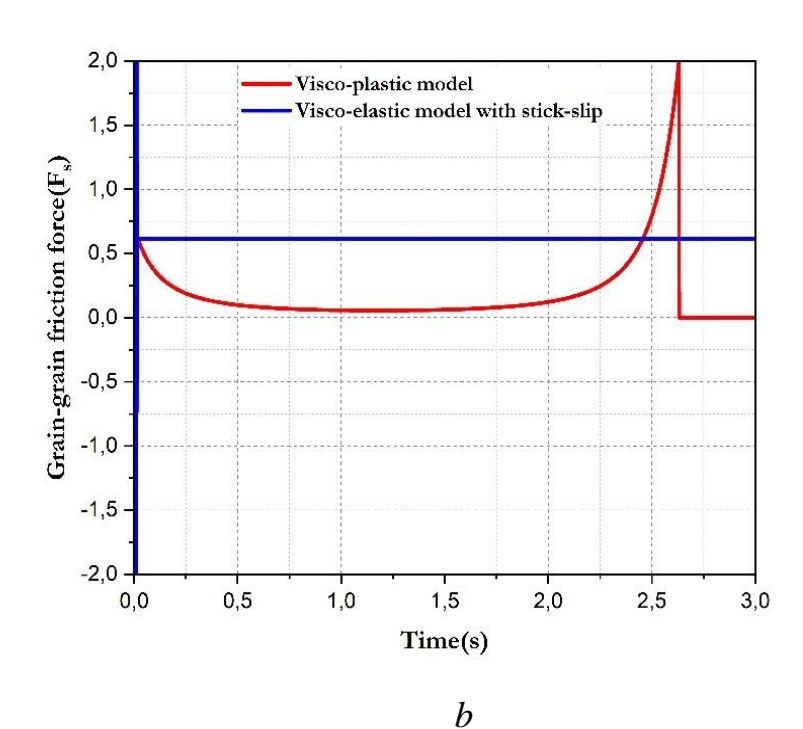


Figure 3.12. Comparison between the presented friction models:

a – coulomb model; b – visco-plastic model

Fig. 12, a shows that, for the coulomb model the tangential force alternates between two equal values of different signs. Since the average of these values is zero, the grain 1 cannot remain suspended above the bottom of the tray. It should be noted that the friction force values correspond to the static Coulomb's threshold that evolves with the grain displacement which induces the increase

in the overlap and consequently the increase in the normal force. Compared to the Coulomb's model the friction force values for the other models are very small. These forces result from the tangential deformation of the grains.

For the visco-plastic model (Fig. 12, b), at the beginning of the test, the grain 1 reaches a certain vertical velocity before the initiation of the contact, which is why

the friction force is initially close to 0.6 N. This latter gradually slows down the grain 1 which decreases the relative tangential velocity to reach a zero value. Consequently, the friction force becomes close to zero and the grain restarts an accelerated downward movement under the effect of its weight. The increase in the velocity produces an increase in the friction force until the instant t=2.65 s, where the grain reaches the bottom of the tray (Fig. 11). Thus, from this moment the velocity of the grain 1 becomes zero. It can be concluded that at a quasi-static regime, the visco-plastic model alternates the movement between accelerated and decelerated, which leads to a continuous movement of the grain.

For the visco-elastic model with stick-slip, the friction force reaches a constant value (close to 0.6 N) from the beginning of the test. This allows to retain the grain 1 locked between the gain 2 and the tray wall under the effect of this force as well as the normal contact force.

3.5.3. Dynamic example

The aim of this example is to show the transition from static to dynamic regime and the effect of the translation velocity on the friction force modeled through the visco-elastic with stick-slip model. In this simulation a particle of weight \vec{P} placed on a non-deformable plate initially horizontal. This plate is then rotated with a constant angular velocity until reaching the coulomb static threshold, i. e. $\tan\beta = \mu_s$ (β – plate inclination). It should be noted that the grain motion is due to its own weight and the grain rotation is locked such that it undergoes only a translation motion as illustrated in Fig. 13. In this way the shape of the grain (circular, rectangular, square, etc.) has no effect on the results, the circular element is chosen, since it is the most common element used in DEM modeling practice.

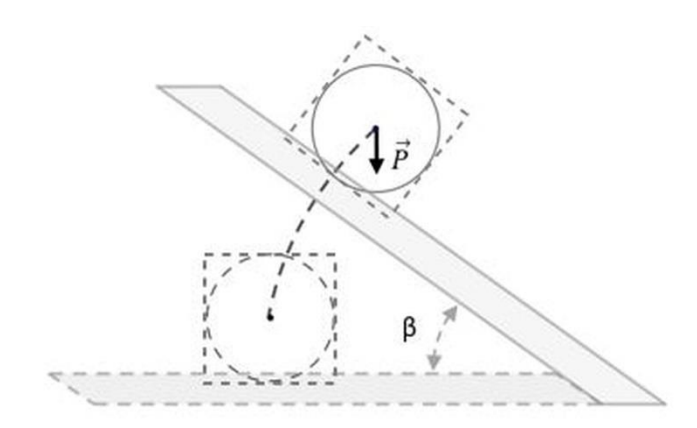


Figure 3.13. Schematic representation of the performed test the grain can undergo only a translation motion, the rotation being locked

Fig. 14, a shows the evolution of the surface inclination angle β and the friction force with time. It is clear that before the motion triggering $tan\beta \leq \mu_s$, β evolves linearly with time since the rotation velocity of the plate is constant. Whereas, the evolution of the friction force follows the sinusoidal form $sin\beta$ given that it is the reaction to the tangential driving force which is equal to $\|\vec{p}\|sin\beta$. When $tan\beta = \mu_s$, F_S reaches the static threshold and the grain starts to slid.

Fig. 14, b shows a zoom of the dynamic part of the test where β is maintained constant such as $tan\beta = \mu_s$. In this case the friction force evolution could be decomposed in three distinct phases: a transition phase, a stick-slip phase, and a steady sliding phase. The transition phase represents the transition from the static equilibrium state to the sliding state. It is notable that, when the rotation of the plate stops, the grain momentum causes a sharply and instantaneous decreasing in the normal force, which causes a sharply decreasing in the friction force. The variation in the tangential force in this phase is due to the variation in the normal force caused by the normal movement of the grain resulting from the sudden stop of the plate.

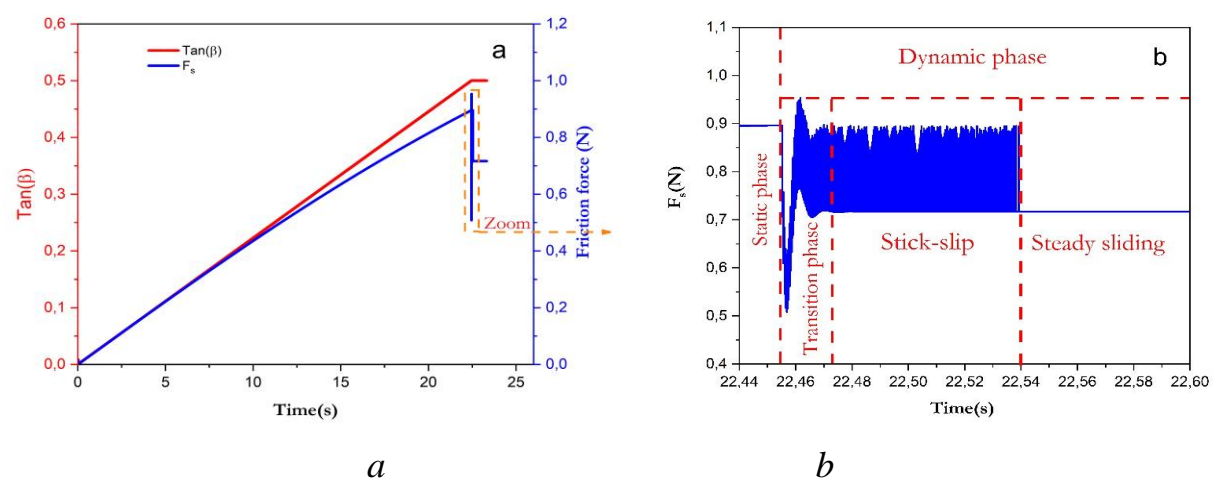


Figure 3.14. Friction force and $tan(\beta)$ evolution: a – with time; b – a zoom of the dynamic part of the test where β is maintained constant such as $tan\beta = \mu_s$

After the transition phase, the grain enters the stick-slip motion and the friction force switches between static and dynamic thresholds as described in example 1. During this phase the average of the friction forces is lower than the static limit, the balance of forces produces a non-zero acceleration, consequently the movement of the grain becomes accelerated. At the beginning of the stick-slip phase, the grain has a low translation velocity and the stick stage is well resolved as illustrated in Fig. 15. Therefore, the average of the friction forces is close to $\mu_k F_n$. With the increase in the translation velocity the stick stage becomes poorly resolved and sometimes undetectable, therefore, the slip stage becomes predominant and the average of the friction forces decreases. As a result, during this phase the friction forces average is decreasing thus the movement acceleration is continuously increasing as shown in Fig. 15.

When the translation velocity is sufficiently high, the stick stages become invisible, the friction force is constant and equals to F_s^{min} , thus the acceleration remains constant (Fig. 15). This is the steady sliding phase, where continuous and smooth motion occurs.

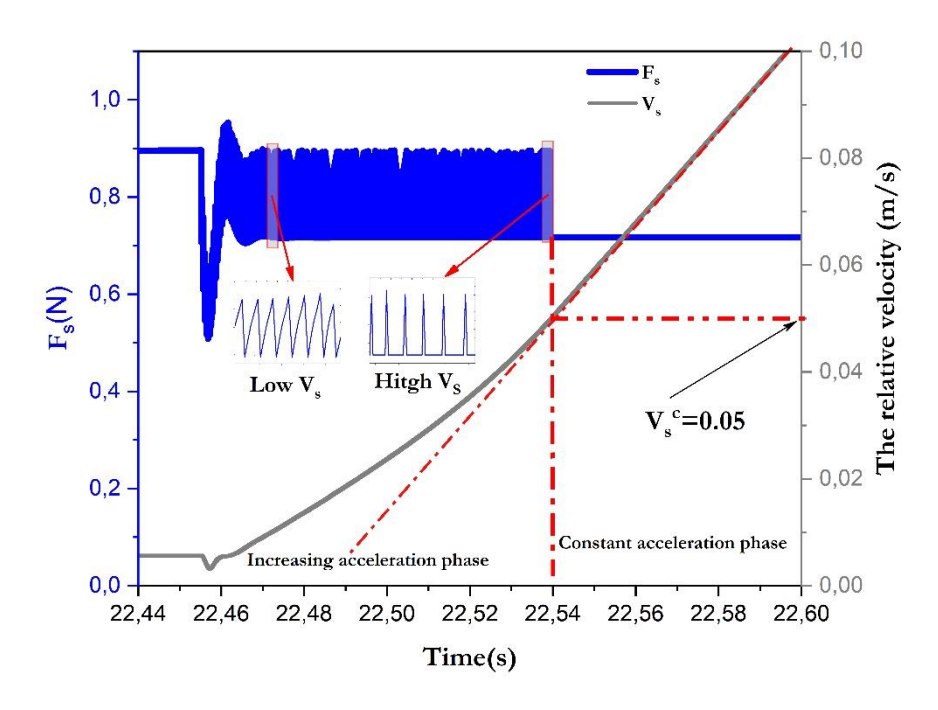


Figure 3.15. Translation velocity evolution

The above behavior is generally in good agreement with what has been observed experimentally as described in Fig. 3.4. Therefore, the friction model presented in this paper captures clearly the effect of the shear rate on the friction force. This latter will be detailed in future research and more parameters should be studied.

3.6. Discussion of results and model

A two-dimensional model of friction that incorporates the stick-slip phenomenon offers valuable insights into the complex interactions between surfaces in contact. In the presented model, the stick-slip behavior is characterized by phases of static friction (stick) followed by sudden motion (slip). These phases are governed by the elastic deformation, the static and dynamic Coulomb friction coefficients. In this research work, numerical tests with details on the evolution of the tangential force with displacement (stick and slip) were carried out. These tests have shown that the model effectively captures the characteristics of static and dynamic intergranular friction. In particular, these tests have shown that formulating the model in the way presented here captures the dependence of friction force on tangential velocity in the case of dynamic sliding, a phenomenon well known from experience. This model could thus contribute, through discrete element modeling, to the understanding of phenomena involved in the mechanics of granular materials. It should be remembered, however, that the precision of numerical modeling results, always depends on the introduced model parameters. For this model, the micromechanical input parameters, i. e. the tangential elastic stiffness and the static

and dynamic friction coefficients, should be well identified in order to achieve efficient modeling.

Besides, in this work, the model is presented in 2D configuration, in which only one deformation variable per contact is required. When considering the extension of this model to 3D discrete element modeling, certain difficulties arise: firstly, the number of contacts increases rapidly with the number of grains; secondly, shear deformation is characterized by three variables per contact. This leads to substantial increases in computational time and memory requirements. The challenge, therefore, is to achieve a simplified 3D formulation of the model that can be less memory- and computation-time-consuming, and this is one of the aims of future work.

3.7. Model application for large scale specimen

One of the experimental methods used to investigate the mechanical behavior of granular materials is the biaxial test. In this test, the soil specimen is subjected to compressive stresses along two axes, allowing for the analysis of shear band formation and material failure under controlled conditions.

In order to test the new friction model under a large-scale granular media, three biaxial tests were performed. in these tests the biaxial apparatus is designed to facilitate precise control over loading conditions and to measure critical parameters such as axial load, lateral pressure, and displacement. The dimensions (height h and length L) of the samples are chosen to respect the ratio h=2L, where h=12 cm and L=6 cm (fig 3.17).

The sample is composed of polydisperse circular shaped particles whose diameters are obtained from the cumulate volume distributions model proposed by Voivret et al [17]. In our simulations, the maximum and minimum diameter values are taken: dmax = 2dmin = 1mm. The grain size distribution curve is shown in figure 3.16. The sample is built by isotropic compression with a pressure of 10 kPa and without gravity acceleration. In order to obtain a dense specimen, the inter-granular friction is set to zero in the isotropic confining step. During the biaxial compression, the friction coefficient is set to the required value.

As recommended by several researchers [31], the model's grains number is taken greater than 4000 particles in order to respect the representative elementary volume.

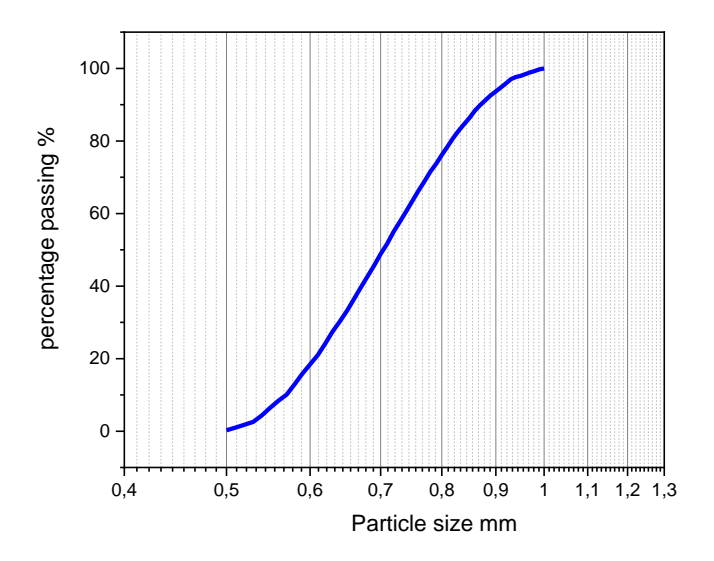


Figure 3.16. Grain size distribution

The discrete elements modeling parameters used in the simulations are summarized in table 3.3:

Table 3.3. Parameters used for Biaxial tests

Characteristics	Symbol	Value	Unite
Normal Stiffness	K_n	12000000	N/m^2
Tangential stiffness	K_s	9600000	N/m^2
Normal viscous damping	v_n	41.38	Kg/s^{-1}
coefficient calculated from a			
restitution coefficient of 0.1			
Tangential viscous damping	v_s	33.10	Kg/s^{-1}
coefficient			
Kinetic coefficient of friction	μ_k	0.4	
Static coefficient of friction	μ_s	0.5	
Gravity	G	0	m/s^2
Max radius of grain	$r_i max$	0.001	m
Density of grains	ρ	2600	Kg/m^3

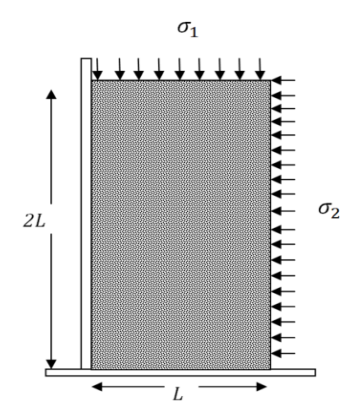


Figure 3.17. Diagram of the performed biaxial compression shear test

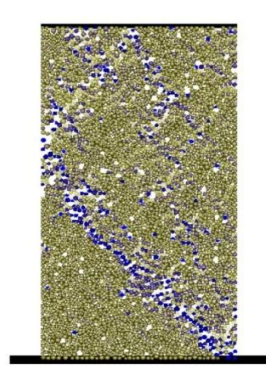


Figure 3.18. A snapshot of a simulated biaxial at failure phase

The blue grains represent the grains with high rolling displacement (shear band)

The evolution of the deviatoric stresses during the three tests are plotted in figure 3.18. as showing in this figure the material presents a deletant behavior.

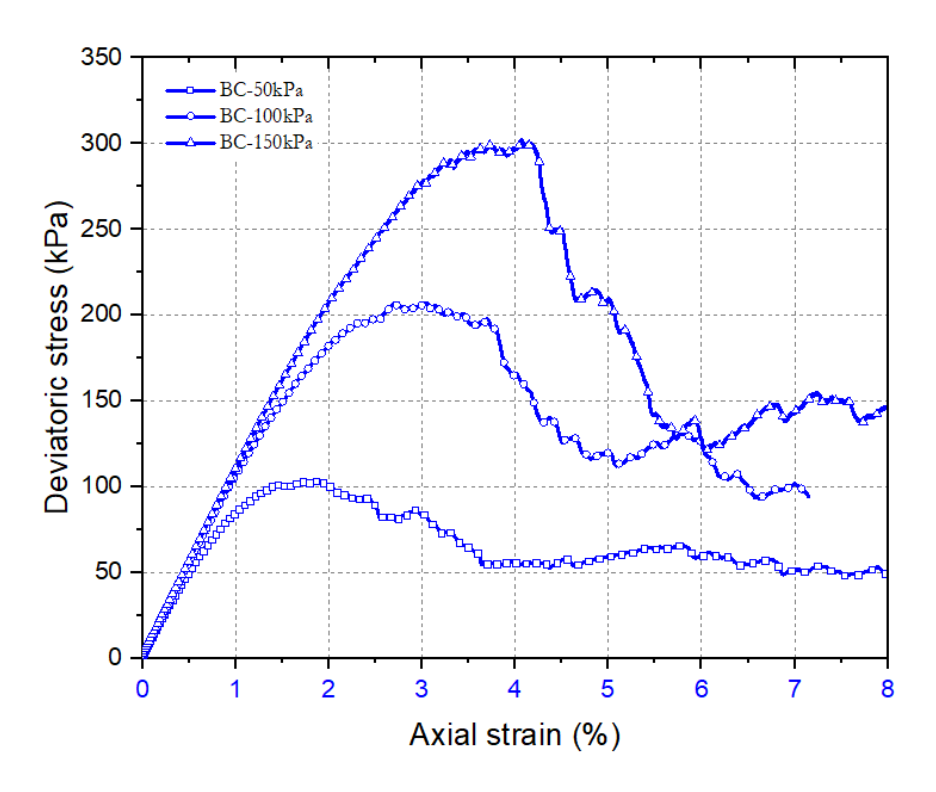


Figure 3.19. Deviatoric stresses Vs Axial strain

To evaluate the shear strength parameters, three shear tests are performed with three different confining stresses (50kPa, 100kPa,150kPa). The deviatoric stress versus axial strain curve obtained from a biaxial test on a dense model material exhibits distinct characteristics that reflect the behavior of dense sand. This curve is composed of three individual curves corresponding to different confinement states. Each curve demonstrates a clear peak, indicating the maximum deviatoric stress that the material can withstand before failure, which is influenced by the level of confining pressure applied during the test. As the confinement increases, the peak deviatoric stress rises, showcasing the material's ability to resist deformation under higher pressures. Beyond the peak, each curve gradually transitions into a critical state, where further axial strain leads to a stabilization of stress, highlighting the material's tendency to reach a consistent state of deformation regardless of additional loading. This behavior is characteristic of dense sands, where increased confinement enhances strength and alters the failure mechanisms, thereby providing valuable insights into the mechanical properties of granular materials under varying stress conditions.

The confining stresses and the corresponding peak deviatoric failure stresses are given in Table 3.4.

Specimen 1 Specimen 2 Specimen 3 (BC-SPC1) (BC-SPC3) (BC-SPC2) **Confining stress 50** 100 150 σ_3 (kPa) Peak failure stress 153 307 452 σ_1 (kPa)

Table 3.4. Data and results of the performed shear tests

As shown in figure 3.19, the volumetric strain versus axial strain graph obtained from the biaxial test on a dense model material reveals important insights into the material's behavior under loading conditions. This graph typically features a distinct pattern characterized by an initial contraction phase, where the volumetric strain decreases as axial strain increases. This phase indicates that the material is compacting under applied stress, a common behavior observed in dense granular materials. As the axial strain continues to increase, the graph eventually shows a transition to a dilatant phase, where volumetric strain begins to increase, reflecting the material's tendency to expand as it approaches its critical state. The transition point marks a significant change in the internal structure of the material, where particle rearrangement leads to an increase in volume despite ongoing axial deformation. This behavior is indicative of dense sands, where the interplay between compaction and dilation is crucial for understanding their mechanical response under varying loading conditions. Overall, this volumetric strain curve complements the deviatoric stress curve by providing a comprehensive view of the material's response to stress, highlighting its complex behavior during deformation.

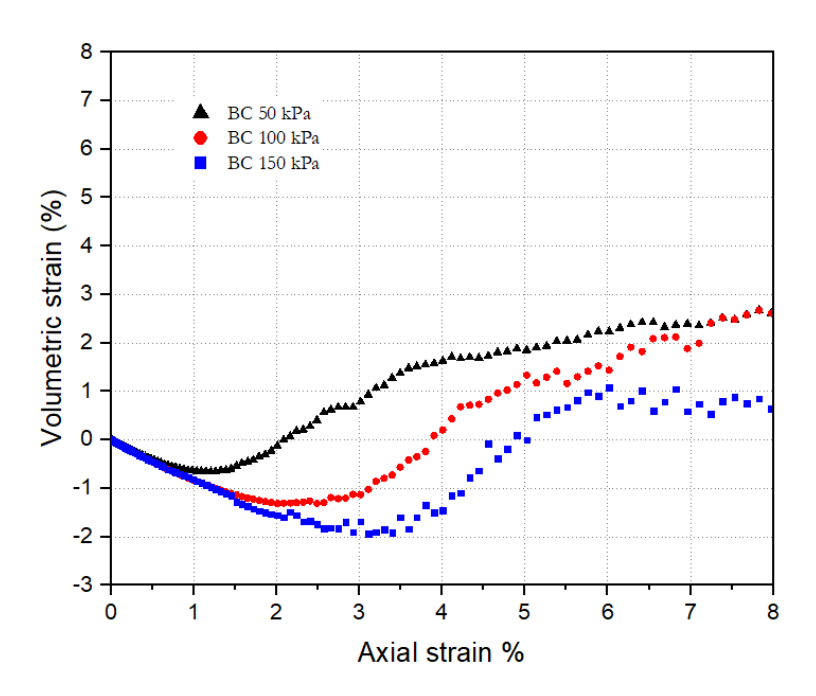


Figure 3.20. Volumetric deformation Vs Axial strain.

The peak failure stresses are used to plot the Mohr circles and consequently the envelope curves at failure in both cases peak and critical state as shown in (Fig. 3.20.).

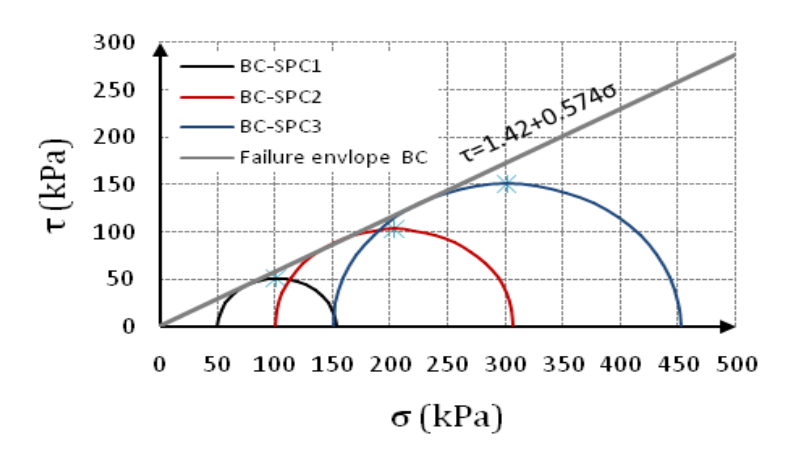


Figure 3.20. Mohr circles and envelope curve at peak failure.

Peak friction angle (ϕ'_p) obtained from the diagrams of Figure 3. 20 is 29.86°, whereas the cohesion (C) has a negligible value. The macroscopic shear strength parameters of the simulated granular material are therefore listed in table 3.5:

Table 3.5. Macroscopic shear strength parameters of the material obtained from a biaxial test.

ø ′ _p	C(kPa)	
30°	0	

The results obtained show that the model is well implemented in the calculation code and that the behavior of the material model behaves well like dry sand.

3.8. Conclusions

Discrete element modeling is a powerful tool for simulating the different phenomena and behaviors related to the granular materials. The micro-macro relationship is governed by the appropriate choice of rheological models at the intergranular contact's level. In this work a dry friction model for DEM soft contact modeling is formulated and analyzed. The model is based on the regularized Coulomb friction model accounting for the stick-slip behavior. Various numerical validation tests have been designed and carried out, the first test explored the quasi-static regime, in which it is shown that the model successfully depicts the alternating periods of sticking and slipping. The second example focused on the static regime, where it is demonstrated that the model operates robustly for zero shear rate cases. Such a performance is crucial for applications where objects remain stationary and are subjected to gradually increasing forces. The third example combined both static and dynamic regimes. Through this example, it is shown that the model effectively captures the variation of the friction force with the shear rate.

In conclusion, the biaxial test conducted on the dense model material serves as a critical evaluation of the proposed intergranular friction model within the framework of the Discrete Element Method (DEM). This experiment was designed to rigorously assess the effectiveness and accuracy of the friction model in simulating the behavior of granular materials under controlled loading conditions. By applying varying levels of confinement and measuring the resulting stress and strain responses, we were able to gather valuable data that highlight the model's performance in predicting key mechanical properties such as shear resistance and volumetric changes. The insights gained from this biaxial testing not only validate the proposed friction model but also enhance our understanding of particle interactions and their influence on the overall behavior of granular assemblies.

Chapter 04

APPLICATION OF DEM TO THE ANALYSIS OF LATERAL EARTH PRESSURES AT REST IN DRY GRANULAR SOILS

4.1. Introduction

The lateral earth pressure coefficient at rest (K_0) is defined as the ratio of the horizontal effective stress to the vertical effective stress in a soil deposited under zero horizontal displacement (as would be the case of a natural accumulating sediment). Terzaghi (1923) expressed K_0 in terms of a so-called "mobilized" internal friction angle (ϕ_{mah}) :

$$K_0 = \frac{1-\sin\phi_{mob}}{1+\sin\phi_{mob}} \tag{4.1}$$

 (ϕ_{mob}) is a friction angle less than the effective limit state friction angle (ϕ) . However, this angle (ϕ_{mob}) is still difficult to quantify.

Subsequently, given that this coefficient (K_0) is involved in the design of many underground structures, it has been the subject of much interest. The first outstanding theory on the subject is due to Jacky in 1944 [77], who obtained a simplified relationship between K_0 and the effective internal friction angle (ϕ') for a normally consolidated soil, known by the expression:

$$K_0 = 1 - \sin \emptyset' \tag{4.2}$$

Even if this relationship is not theoretically sound since it connects a parameter of zero horizontal strain state (K_0) to a parameter of failure state (ϕ) , it remains widely used in practice engineering to this day due to its simplicity and the acceptable results it provides for a wide range of situations.

Later, it was shown that lateral earth pressure is affected by many factors, namely void ratio or packing density, confining pressure, stress history, sample preparation (fabric) and particles properties including shape, angularity and inter-particles friction or roughness. A large number of experimental studies have been carried out to show the effects of the different factors on K_0 for

granular soils. These studies have mainly been carried out using oedometric devices equipped with means for measuring lateral pressure, or using the triaxial device with a controlled strain path in order to maintain zero radial strain. The main conclusions that can be drawn from these studies may be as follows: (1) K_0 seems to decrease with the increase in the relative density, generally the denser the sand the lower the K_0 value [78], [79], [80], [81], [82] and [83]. However, this finding is contradicted by the results of certain studies [84][85]. (2) To assess the effect of fabric on K_0 , different sample reconstitution methods were used, including air pluviation, water pluviation and wet tamping.

Generally, it is found that the method of preparation, i.e. the fabric, affects the K_0 values. It seems that pluviation methods result in higher K_0 compared to tamping methods [80], [81], [86]. However, [87], [88], [89] showed that samples prepared by tamping exhibit more expansion than samples obtained by pluviation, therefore they have greater Poisson's ratios and consequently greater K_0 values. This conclusion contradicts the first findings. (3) The particle surface roughness has relatively small effect on K_0 , whereas the particle shape and angularity have significant effects [82]. (4) For normally consolidated sands, the Jaky equation based on the soil's internal friction angle, may still accepted as an approximation of K_0 [82], [86], [90]. In general the use of the critical state friction angle (ϕ'_{cv}) gives a better approximation of K_0 compared to the peak friction angle (ϕ'_P) . However, a large number of studies indicate that the experimental values of K_0 are far from those given by Jaky equation [78], [80], [82], [83], [90] and [91]. This could be attributed to not taking into account all parameters having an effect on K_0 . (5) For overconsolidated sands, the coefficient K_0 increases with the increase in of overconsolidation ratio, but depends on the stress path, i.e. loading or unloading. Based on a large number of experimental results, Mayne and Kulhawy (1982) [92] obtained a well-known relationship for this case, expressed as follows:

$$\begin{cases} K_{0l} = (1 - \sin \emptyset') & Loading (normally consolidated) \\ K_{0ul} = (1 - \sin \emptyset') OCR^{\sin \emptyset'} & Unloading (overconsolidated) \end{cases}$$
 (4.3)

Where K_{0l} and K_{0ul} are the lateral earth pressure coefficient at rest during loading and unloading phases, respectively.

Later, Zeng and Ni (1999) [93] improved this relationship to accommodate more experimental results, giving the relationship:

$$\begin{cases} K_{0l} = a(1-\sin\emptyset') & Loading (normally consolidated) \\ K_{0ul} = a(1-\sin\emptyset')OCR^{bsin\emptyset'} & Unloading (overconsolidated) \end{cases}$$
 (4.4)

Where a and b are parameters dependent on soil particle properties, such that a adjusts K_0 for normally consolidated soil and b adjusts the variation of K_0 with the overconsolidation ratio, they proposed to set $b = \frac{a}{2}$.

The discrepancies between certain experimental results highlight the complexity of the problem. Thus, in order to better understand the origin of K_0 at the particle scale and taking into account the discrete nature of granular materials, several researchers have attempted to understand the problem using discrete element modeling. Yun et al [94] carried out discrete element simulations to highlight the effects of intergranular friction and grain shape on K_0 . For this purpose, they used the PFC3D 4.0 code with spherical grains as well as sphere clusters to simulate the grain shape of natural sands. They concluded that changing the friction coefficient adequately captures the variation of K_0 during loading and unloading cycles for the glass beads.

Whereas, in order to capture the evolutions of K_0 observed experimentally for natural sand, it is necessary to use grain clusters. Lopera Perez et al [95] studied the one-dimensional vertical compression of an idealized soil through discrete element modeling using a modified version of the Lampps open source code. They found that K_0 increases with the increase of the void ratio, which is explained by: for dense samples (low void ratio), the contacts are oriented more horizontally, which reduces the transmitted horizontal stresses resulting from the vertical pressures. On the contrary, for loose samples, the distribution of contact orientations is rather isotropic, which increases the transmitted horizontal stresses. Khalili et al [96] have performed a discrete elements micromechanical analysis of the oedometric compression up to high stresses. The used material is made of slightly polydisperse beads with Hertz - Mindlin elastic - frictional contacts. They found that for dense samples, the coordination number depends on the sample packing procedure, but changes little with compression cycles. In addition, they mentioned that the reversibility of the behavior is much more pronounced for the used model than that of natural sands. They attributed this result to the possibility of plasticity and damage of sand grains, which is not supported by the numerical model used. Gu et al [97] used DEM to study the one-dimensional (1D) compression (oedometer) test to determine K_0 of granular soil at different void ratios and confining pressures. The samples used are built by pluviation in a cubic mold with smooth and non-deformable walls. The void ratios are varied in different ways; by changing the coefficient of intergranular friction during pluviation or by removing grains after deposition. They found that K_0 of specimens prepared by different methods may be quite different even if the void ratio and vertical stress are the same. On the other hand, based on the analysis at the particulate level, they indicated that the coordination number of the soil is a dominant

parameter on the K_0 . In addition, using the friction angles obtained from triaxial tests on the same material model, they found that using of peak friction angle in the Jaky's equation better predicts the numerically calculated K_0 compared to critical friction angle.

Chen et al [98] carried out numerical simulations of oedometric compression of granular materials using the discrete element method with focusing on the effect of particle shape. They used the open-source discrete element code, SudoDEM to model ellipsoids and superballs shaped particles. Their work led to the conclusion that the anisotropy of normal contact forces has a more significant effect on K_0 compared to the anisotropy of contacts and grain shape.

As a conclusion to the above literature review, it may be seen that the parameters influencing K_0 and the relative underlying physics are far from well understood, prompting a revisiting of the subject. This is the context of the present work, it is an investigation of the lateral earth pressure at rest coefficient K_0 for a cohesionless dense soil (sand) through a discrete elements modeling. A 2D modeling of an oedometric test with controlled vertical displacement is first carried out. Then, the variation of K_0 as well as some micromechanical parameters such as contact orientations, number of contacts and intensities of normal contact forces with the stress history is analyzed. The evolution of the effect of stress history on K_0 and fabric anisotropy as a function of intergranular friction is also demonstrated using a simple assembly of grains.

4.2. Discrete Element Method

The discrete element model used in this work is based on the molecular dynamics method developed for granular media by Cundall and Strack [27]. This method assumes that the grains of the material are independent elements that interact through contact forces. The overall deformation of the material results from the relative displacement of the elements. The movement of each element is governed by Newton's second law which takes into account contact forces and external forces such as gravity. In molecular dynamics, elements are assumed to be slightly deformable, thus contact forces are calculated explicitly in terms of grain deformations. Each contact force $(\overrightarrow{F_{tJ}})$ has two components one is normal to the contact area and the other is tangential. In this work, the simple viscoelastic model (Fig.1b) is used to calculate the normal contact force, therefore $F_n = (-\delta_n K_n - v_n V_n)$, where K_n is the normal elastic stiffness, v_n is the viscous damping coefficient and V_n is the normal velocity of the grain j with respect to the grain i. For the tangential contact force (F_s) , it is calculated through a damped elastic perfectly plastic model (Fig.1b), so it is expressed $F_s = \min(K_s \delta_s + v_s V_s; \mu |F_n|)$, where K_s is the tangential stiffness, v_s is the tangential viscous damping

coefficient, V_s is the tangential velocity of the grain j relative to the grain i at the contact point, μ is the friction coefficient and δ_s is the tangential contacting grains deformation.

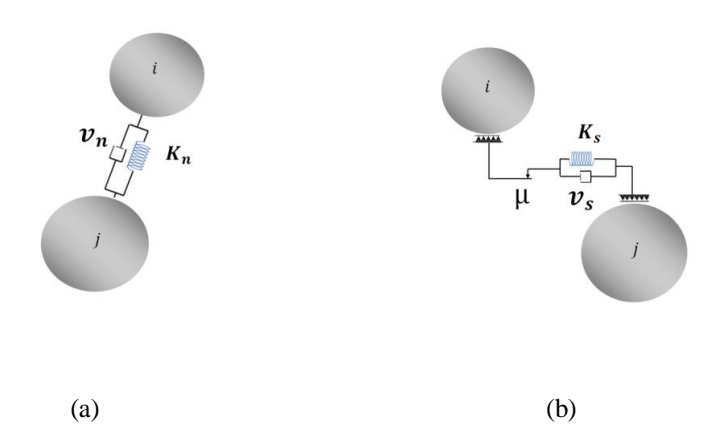


Figure 4.1. Grain interaction force models.

(a) Normal force model, (b) Tangential force model.

In this work, the grains are assumed to be circular in shape, in order to approximate the rolling resistance that naturally exists in reality, a simple rolling resistance model is integrated. It is assumed that the normal contact force is shifted from the contact surface center in the rolling sens (Fig.4.2.).

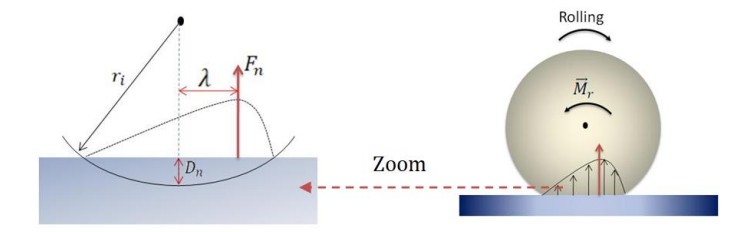


Figure 4.2. Illustration of the rolling resistance model.

The rolling resistance moment is therefore calculated by:

$$\vec{M}_r = -\lambda \, F_n \frac{\vec{w_l}'}{\left\| \vec{w_l}' \right\|} \tag{4.5}$$

Where $\overrightarrow{w_i}'$ is the relative angular velocity of grain i, it is expressed in the general case of rolling of grain i on grain j by: $\overrightarrow{w_i}' = \overrightarrow{w_i} - \overrightarrow{w_j}$, and λ is the normal force shift given by:

$$\lambda = \psi \sqrt{r_i^2 - (r_i - \frac{\delta_n}{2})^2}$$
 (4.6)

 ψ is a coefficient that controls the position of F_n . In all simulations we adopted $\psi = 0.5$.

Finally, it should be noted that for the following applications, a C++ code is developed using the contact force models described above.

4.3. Model properties

4.3.1. A description of the simulated oedometer

The 2D simulated oedometer cell is shown in Figure 4.3, the left and right walls of the cell are fixed and smooth to simulate the K_0 condition. During the tests, the vertical stress (σ_v) is applied through a horizontal undeformable plate placed above the sample inside the cell. This stress is adjusted by a servo-controlled vertical displacement of the plate.

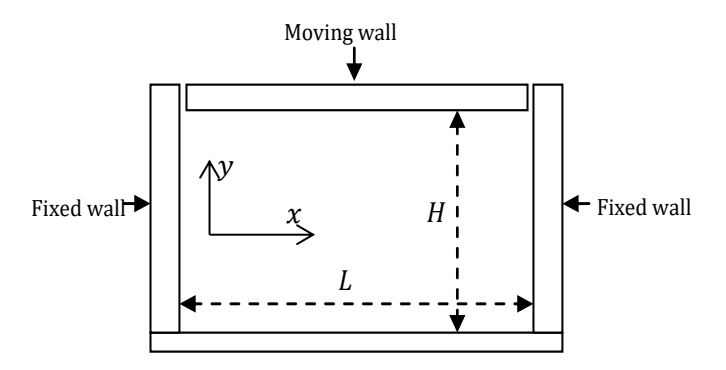


Figure 4.3. Diagram of the simulated oedometer

It should be remembered that in laboratory oedometric tests, it is recommended to use cells having a diameter/height ratio greater than 2.5 in order to minimize the effects of soil friction on the side walls [99]. This condition is not necessary in the simulations since the friction on the lateral walls can be eliminated completely in the numerical model.

4.3.2. Microscopic sample properties

The sample is composed of polydisperse circular shaped particles whose diameters are obtained from the cumulate volume distributions model proposed by Voivret et al [25]. In our simulations, the maximum and minimum diameter values are taken: dmax = 2dmin = 1mm. The grain size distribution curve is shown in figure 3.16(see chapter 3). The sample is built by isotropic compression with a pressure of 10 kPa and without gravity acceleration. In order to obtain a dense specimen, the inter-granular friction is set to zero in the isotropic confining step. During the oedometric compression, the friction coefficient is set to the required value.

As recommended by several researchers [26], the model's grains number is taken greater

than 4000 particles in order to respect the representative elementary volume.

The simulation parameter are taken the same as for the biaxial test described in the previous chapter.

4.3.3. Macroscopic geotechnical parameters

In order to compare the numerical results with empirical formulas based on the soil's internal friction angle, biaxial compression tests (BC) are carried out on same material. The used BC samples are built under the same conditions (see chapter 3).

Peak friction angle (ϕ'_p) and cohesion (C) are estimated through the biaxial tests. The macroscopic shear strength parameters of the simulated granular material are therefore listed in table 4.3:

Table 4.1. Macroscopic shear strength parameters of the material obtained from a biaxial test.

φ ′ _P	C (kPa)		
30°	0		

4.4. Evolution of K_0 under oedometric loading

The lateral earth pressure at rest have the expression $K_0 = \frac{\sigma_h}{\sigma_v}$, where σ_h and σ_v are components of the average intergranular stress tensor. For static or quasi-static problems in granular media, the average stress tensor is expressed by [27]:

$$\sigma_{ij} = \frac{1}{V} \sum_{n_c=1}^{N_c} F_i^{n_c} L_j^{n_c}$$
 (4.7)

Where i and j define the computed component of the stress tensor at the center of the volume V, N_c being the total number of contacts in the volume V, $F_i^{n_c}$ is the i component of the interaction force at the contact n_c and $L_j^{n_c}$ is the j component of the vector \vec{L} connecting the centers of the two contacting grains (branch vector). The stress components involved in K_0 expression are $\sigma_h = \sigma_{xx}$ (i, j = x, x) and $\sigma_v = \sigma_{yy}$ (i, j = y, y).

4.4.1. Evolution of K_0 for a one loading-unloading cycle

In order to evaluate the effect of the loading history on K_0 , an oedometric test on a normally consolidated sample with one loading-unloading cycle is simulated. During the test, horizontal and vertical stresses as well as K_0 are continuously calculated. Figure 4.4 shows a plot of the evolution of

 K_0 during the test. For comparison, the empirical equations (4.3) and (4.4), relating K_0 to the soil's internal friction angle and the over consolidation ratio are plotted on the same graph.

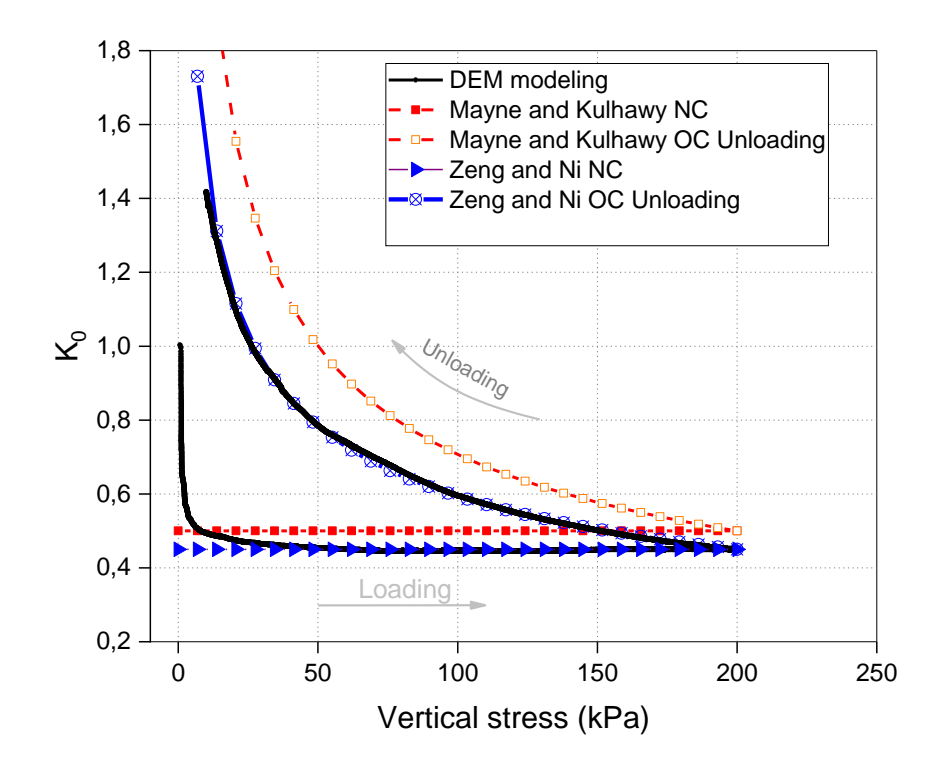


Figure 4.4. Evolution of K_0 for one loading-unloading cycle, K_0 computed using DEM model and empirical formulas.

For the DEM model, during the loading phase, the soil remains normally consolidated. It may first be noted that the stress state is initially isotropic (K_0 =1). As vertical stress increases, K_0 decreases rapidly, reaching a plateau where it becomes almost constant, although a slight increase can be observed with increasing load. This plateau corresponds to the situation of a normally consolidated soil.

It may be noted that for this situation, K_0 obtained from the DEM model is slightly lower than that calculated by Jacky equation, shown in the figure as the Mayne and Kulhawy equation for the normally consolidated (NC) case. A similar result was obtained in the work of Gu et al [21] through a DEM model with spherical elements. Note that in their work, the internal friction angle was also determined from a discrete element model of the triaxial test.

In the unloading phase, the soil becomes overconsolidated, with the overconsolidation ratio (OCR) increasing as the vertical stress decreases. It is clear that during this phase, K_0 increases according to a non-linear shape. The K_0 curve obtained from the DEM model is very similar to that of [16] (Eq.4.3),

the shift that can be observed between the two curves results from the loading phase. Besides, we noticed that the variation of K_0 according to our DEM model, can be reproduced almost exactly for both loading and unloading phases, by equations similar to those of [17] (Eq. 4.4), but with fitting coefficients a = 0.9 and b = 0.8.

4.4.2. Evolution of K_{θ} for a three-cycle loading

In order to show the effect of cyclic loading on K_0 , the same sample is subjected to three loading-unloading cycles, where the maximum vertical stress is set to 200kPa. Figure 4.5 shows the evolution of K_0 during the three loading cycles.

For the first cycle loading phase, the behavior of the soil is similar to that described in the previous section, where K_0 rapidly tends to reach its value of normally consolidated state. For the following cycles, the evolution of K_0 during the loading phases is rather progressive compared to the first cycle, but at the end of loading, when the sample becomes normally consolidated, the same value is reached for all cycles. For the unloading phases, these curves show that even for the same overconsolidation ratio (at the same vertical stress), K_0 is greater in the unloading phases than in the loading phases. Furthermore, it is noted that in the unloading phases, K_0 is greater in third cycle than in the first and second cycles, this could be attributed to a non-reversible evolution of contact orientations following loading and unloading cycles.

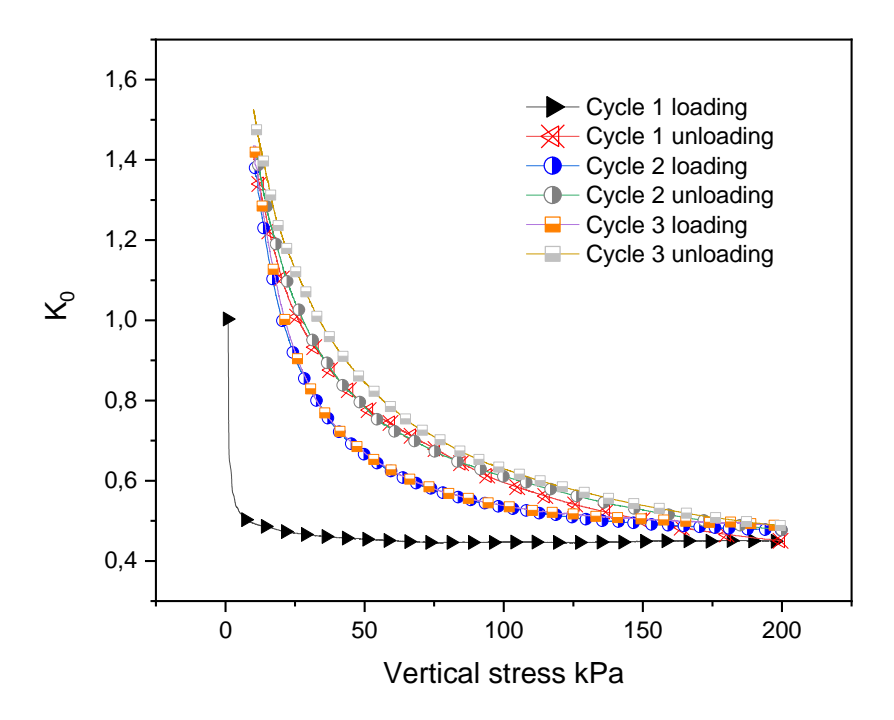


Figure 4.5. Evolution of K_0 for three loading – unloading cycles.

4.5. Effects of micromechanical parameters on K_0

DEM modeling enables monitoring the sample structure at the particle scale. This section presents the evolution of some micromechanical parameters and their effect on K_0 during the loading and unloading phases. We focus namely on the contacts orientations, the number of contacts and normal contact force intensities.

4.5.1. Contact orientations and contact number

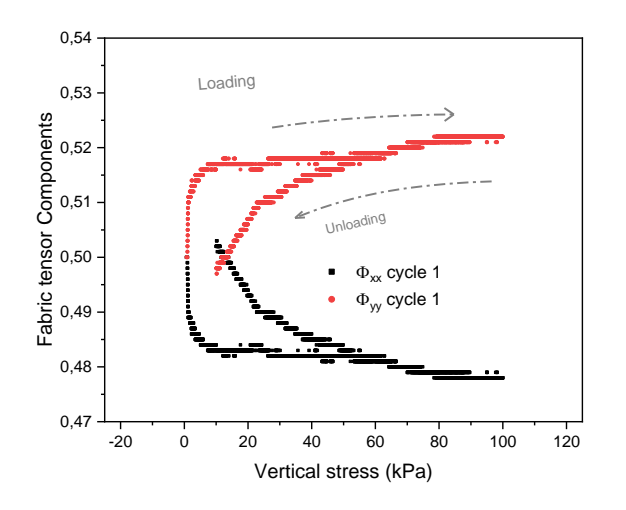
The orientation trend of contacts in a granular deposit can be described by the fabric tensor [28], [29], [30] (Φ_{ij}) defined as:

$$\Phi_{ij} = \frac{1}{N_c} \sum_{n_c=1}^{N_c} n_i \, n_j \tag{4.8}$$

Where N_c is the total number of contacts and n_i is the i component of the contact's normal unit vector. The fabric tensor is symmetric, its diagonal components vary between 0 and 1 ($0 \le \Phi_{ij} \le 1$, for i = j). In 2D case this tensor has three components denoted Φ_{xx} , Φ_{yy} and Φ_{xy} , that define the average orientation of the contacts in the material. In the following, we refer to *horizontal contact*, when the unit normal vector of the contact is oriented in the vertical direction. Conversely, *horizontal*

contacts are those whose unit normal vectors are oriented vertically. In the case where the contacts are rather horizontal (x-direction), Φ_{yy} is greater than Φ_{xx} , the opposite happens when the contacts are rather vertical (y-direction). In all cases the sum of these two components is $1 (\Phi_{xx} + \Phi_{yy} = 1)$. The ratio $F = \frac{\Phi_{xx}}{\Phi_{yy}}$ describes the structural anisotropy and is usually referred to as the *degree of fabric anisotropy*, for an isotropic fabric state $F \approx 1$.

The evolution of the fabric tensor components Φ_{xx} and Φ_{yy} and the degree of anisotropy F during a loading-unloading cycle with a maximum load of 100kPa are shown in figures 4.6a and 4.6b respectively.



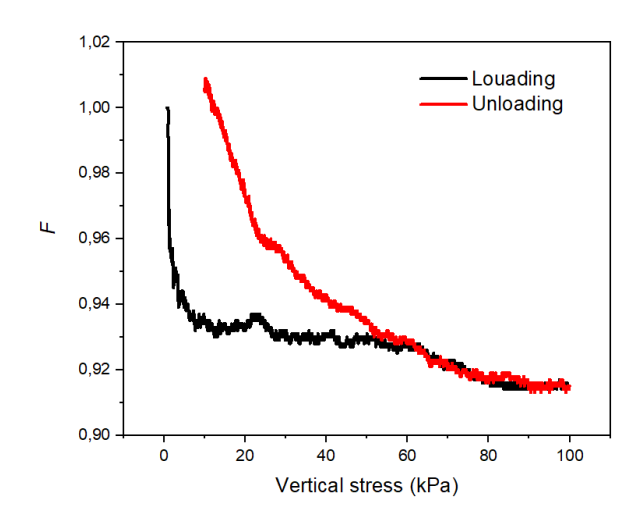


Figure 4.6. Fabric properties of the sample during the loading-unloading cycle.

(a) Fabric tensor components vs vertical stress, (b) Degree of anisotropy vs. vertical stress

These figures show clearly that the sample is initially isotropic ($\Phi_{xx} = \Phi_{yy} = 0.5$; F = 1). With load variation, we note the following key points: (1) during the loading phase Φ_{xx} decreases and Φ_{yy} increases, indicating that the horizontal contacts become more weighty compared to the vertical contacts. The sharp variation at the start of loading reflects a *transition phase* between the isotropic compression state characterizing the initial sample and a state where vertical stress is more dominant. This may indicate that normally consolidated granular deposits subjected to gravity are naturally

characterized by a structural anisotropy where horizontal contacts are more dominant. (2) In the unloading phase, the opposite occurs: Φ_{xx} increases and Φ_{yy} decreases, but more gradually. This indicates that vertical contacts become increasingly weighty, until they become more dominant towards the end of the unloading phase (i.e. $F = \frac{\Phi_{xx}}{\Phi_{yy}}$ becomes greater than 1) even though the sample remains vertically compressed. This may indicate that vertical contacts are more frequent in overconsolidated deposits, and may even be more dominant than horizontal contacts, depending on the overconsolidation ratio.

The observed variation in fabric tensor components under vertical compression may result from the opening of vertical contacts (i.e. a decrease in their number), a change in the orientation of existing contacts towards the horizontal, even without a significant change in the total number of contacts, or a dominant increase in horizontal contacts. In order to explore the influence of these possible scenarios, we proposed to plot the evolution of the number of contacts in the different directions during the loading-unloading cycle. To simplify the presentation of results, only curves for quasivertical contacts (with normal unit vectors between 0° and 10°) and quasi-horizontal contacts (with normal unit vectors between 80° and 90°) are presented (Fig.4.7). As they correspond to extreme directions, these two orientation intervals show the most pronounced variations and have the greatest influence on the evolution of the fabric tensor.

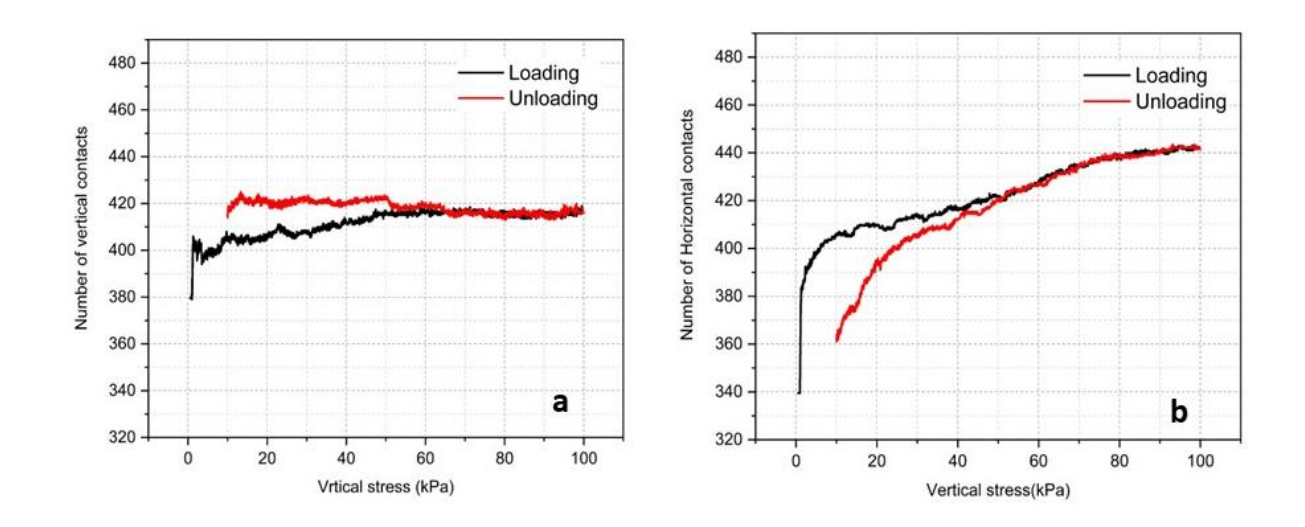


Figure 4.7. Evolution of horizontal and vertical contact numbers in terms of vertical stress for a loading-unloading cycle

normal unit vectors between 0° and 10° , (b) normal unit vectors between 80° and 90°

The plots show that in the loading phase, the number of contacts for both orientations increase with the applied stress. This increase goes essentially through three stages; first for vertical stress below 10kPa, contact numbers increase sharply, with a more significant increase for horizontal contacts. This stage is related to the transition phase, where vertical pressure leads to the closure of essentially horizontal contacts. This explains the rapid decrease in K_0 in this phase, since the increase in horizontal contacts leads to an increase in horizontally oriented friction forces. In the second stage where the vertical stress is between 10kPa and 50kPa, the number of contacts increases almost equally in both directions, resulting in a minor variation in the degree of structural anisotropy (Fig.4.6b). The invariability of K_0 in this stage (see Fig.4.4), reveals an increase in horizontal stress proportional to that of vertical stress. This increase may be attributed to the noted increase in the number of vertical contacts, and possibly to the increase in normal forces on these contacts. In the third stage (vertical stress above 50kPa), the number of vertical contacts reaches a plateau while horizontal contacts continue to increase, resulting in a significant change in the degree of structural anisotropy (Fig.4.6b). In this stage, the steadiness of K_0 even with a stable number of vertical contacts, indicates an increase in normal forces on the vertical contacts.

Based on this discussion, we can conclude that, (1) during the loading phase, the number of contacts increases, but differently according to their orientation, with horizontal contacts increasing more in response to the applied vertical stress. (2) The influence of the increase in the number of contacts on K_0 is only noticeable in the first transition phase (vertical stress below 10kPa). (3) Due to the relatively small change in the number of vertical contacts after the transition phase, we can understand that loading is also accompanied by a change in the normal forces exerted on the contacts, keeping K_0 almost constant after the transition phase.

In the unloading phase, the number of horizontal contacts decreases at a rate comparable to that of the loading phase. On the contrary, there is a slight increase in the number of vertical contacts. These changes explain the increase in the degree of structural anisoropy (Fig. 4.6) and induce an increase in horizontal stress and consequently an increase in K_0 .

The number of contacts in the different directions for the initial state and after the loading-unloading cycle is illustrated in Figure 4.8 by a rose diagram representing the number of contacts per direction. The interval of contact orientation angles from 0° to 180° is divided into segments of 10° each, in which the number of contacts is counted.

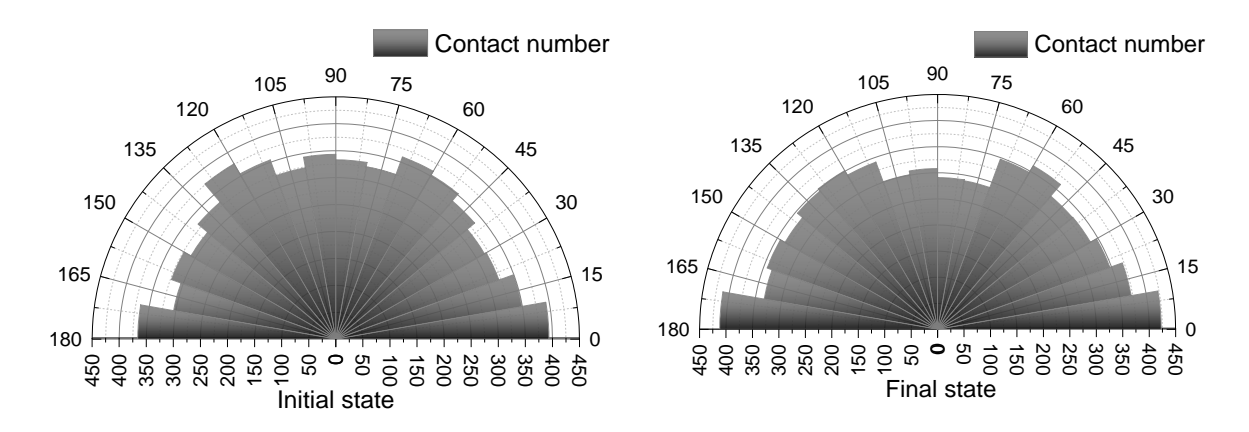


Figure 4.8. Rose diagram of number of contacts per direction, (a) in the initial state, (b) After a loading-unloading cycle.

These two diagrams show that in the initial state, there is an almost isotropic distribution of contacts, whereas after the loading-unloading cycle, vertical contacts become more prevalent, as can be noted on the graphs in figure 4.7.

4.5.2. Normal contacts forces intensities

Similar rose diagrams representing the contact normal forces intensities according to their orientation for the initial state and after the loading-unloading cycle are represented in figure 4.9.

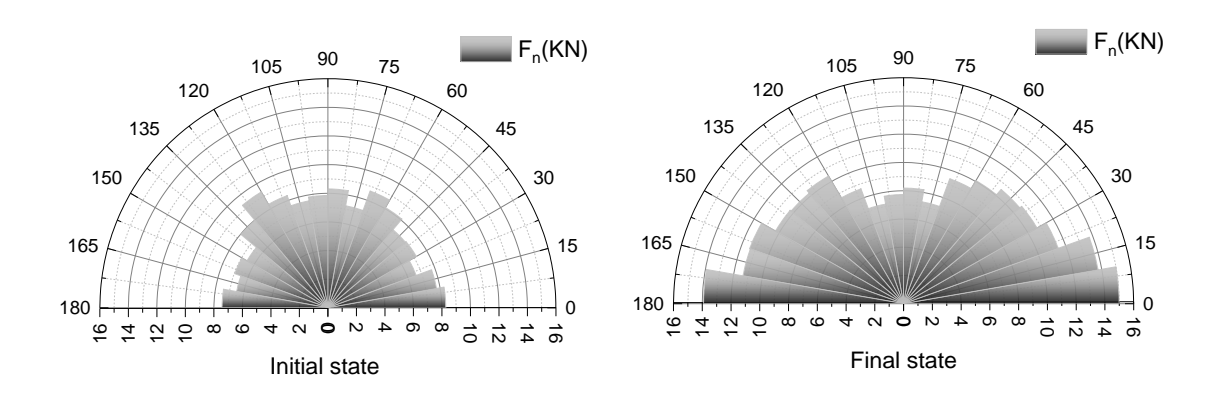


Figure 4.9. Normal contact forces rose diagram.

Again, these diagrams show that in the initial state, there is an almost isotropic distribution of normal

forces intensities at contacts. However, after the loading-unloading cycle, it is shown that the vertical forces return to their initial values, while the horizontal forces increase substantially, which explains the significant increase in K_0 . Compared with the diagrams in figure 4.8, it can be seen that the increase in horizontal forces is much more pronounced than the corresponding vertical contacts. This may indicate that the anisotropy of the fabric tensor can give a qualitative description of the K_0 trend that depends on the dominant direction of the contacts, i.e. K_0 is low when the dominant direction of the contacts is horizontal, on the contrary K_0 is high when the dominant direction of the contacts is vertical. However, from a quantitative point of view, the value of K_0 is governed by the intensity of the forces acting on the contacts.

4.5.3. A demonstration of the effect of intergranular friction on K_0 in the overconsolidated state

This section aims to demonstrate the effect of intergranular friction on K_0 in the overconsolidated state using a simple grain assembly. We consider the example of three grains symmetric assembly subjected to an oedometric loading-unloading cycle, depicted in Figure 4.10. We analyze the evolution of lateral pressure coefficient (K_0) and the degree of anisotropy (F) with the vertical stress variation. Two cases are considered; frictionless and rough grains (Fig. 4.10).

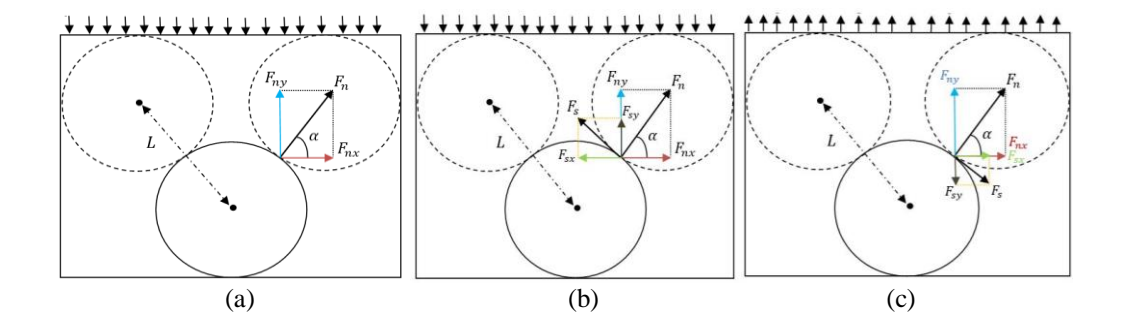


Figure 4.10. Force diagrams; (a) Frictionless grains, loading and unloading phases, (b)Rough grains during loading phase, (c) Rough grains during unloading phase.

4.5.4. Analytical description

a. Frictionless grains

In this case the friction forces are zero, the interaction force is normal to the contact and its components are $F_{nx} = F_n \cos \alpha$ and $F_{ny} = F_n \sin \alpha$ (Fig 4.10 a.).

Using equation 15 and taking account of the problem's symmetry, the at rest lateral earth pressure coefficient K_0 can be expressed:

$$K_0 = \frac{\sigma_{xx}}{\sigma_{yy}} = \frac{N_c F_{nx} L_x}{N_c F_{ny} L_y}$$

$$\tag{4.9}$$

With $N_c=2$ contacts, $L_x=L\cos\alpha$ and $L_y=L\cos\alpha$, it follows therefore:

$$K_0 = \frac{\cos^2 \alpha}{\sin^2 \alpha} \tag{4.10}$$

On the other hand, from equation 16 the degree of structural anisotropy is:

$$F = \frac{\Phi_{xx}}{\Phi_{yy}} = \frac{n_x^2}{n_y^2} = \frac{\cos^2 \alpha}{\sin^2 \alpha}$$
 (4.11)

It is clear that in this particular case K_0 and F are similarly expressed in terms of the contact orientation $K_0 = \frac{\cos^2 \alpha}{\sin^2 \alpha} = F$. Therefore K_0 depends only on the degree of anisotropy F, it does not depend on the contacts number, the applied loading stress and stress path (loading or unloading). It should be noted that when α tends towards zero K_0 becomes infinite, this is the case of grains forced on the same alignment. On the other hand, when α tends towards 90° K_0 becomes zero, this corresponds to the case of a stack of bricks for example. It should be highlighted that for a granular material the average orientation of the contacts is far from these two extremums, i.e. the degree of anisotropy (F) varies around 1.

b. Rough grains

The friction forces are tangent to the contact, they change their directions according to the stress path (loading or unloading) (Fig. 4.10b and Fig. 4.10c). The force diagrams show that in the loading phase the friction force increases the vertical component and decreases the horizontal component of the contact force. The opposite happens in the unloading phase. The ratio $K_0 = \frac{\sigma_{xx}}{\sigma_{yy}}$ is then greater in the unloading phase than in the loading phase. Thus, the force anisotropy depends on the stress path.

4.5.5. Numerical simulations

The idealized example of three grains described above is simulated numerically. The sample is first confined with isotropic pressure of 10kPa, then subjected to an oedometric loading-unloading cycle.

(Fig 4.11) shows snapshots of the simulated example in the two states; the isotropic confining and the oedometric compression states.

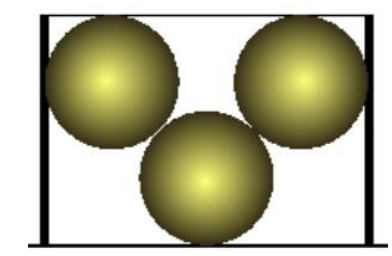


Figure 4.11. The simulated example.

The evolution of the degree of structural anisotropy F versus the vertical stress increase is shown in Figure 4.12.

This plot shows that the degree of structural anisotropy increases with increasing vertical stress and decreases with decreasing vertical stress. For a friction coefficient of zero, this occurs along the same path. However, in the presence of friction, a transient locking phase (see figure 4.12) occurs when the shear force is below the Coulomb friction threshold, forming a loading-unloading loop. In this example, such variation of the degree of structural anisotropy with vertical stress is obvious, given that: (1) the number of contacts remains unchanged (2 contacts) and (2) the contacts tend to become vertical as the load increases. Note that this last statement should be valid for all contacts of any granular deposit subjected to increasing vertical compression.

If we return to the granular deposit considered above, on the contrary, it has been observed that the degree of structural anisotropy decreases with increasing vertical stress. As the change in direction of existing contacts should not lead to a decrease in the degree of structural anisotropy, this demonstrates that the decrease is mainly due to the dominant increase in horizontal contacts.

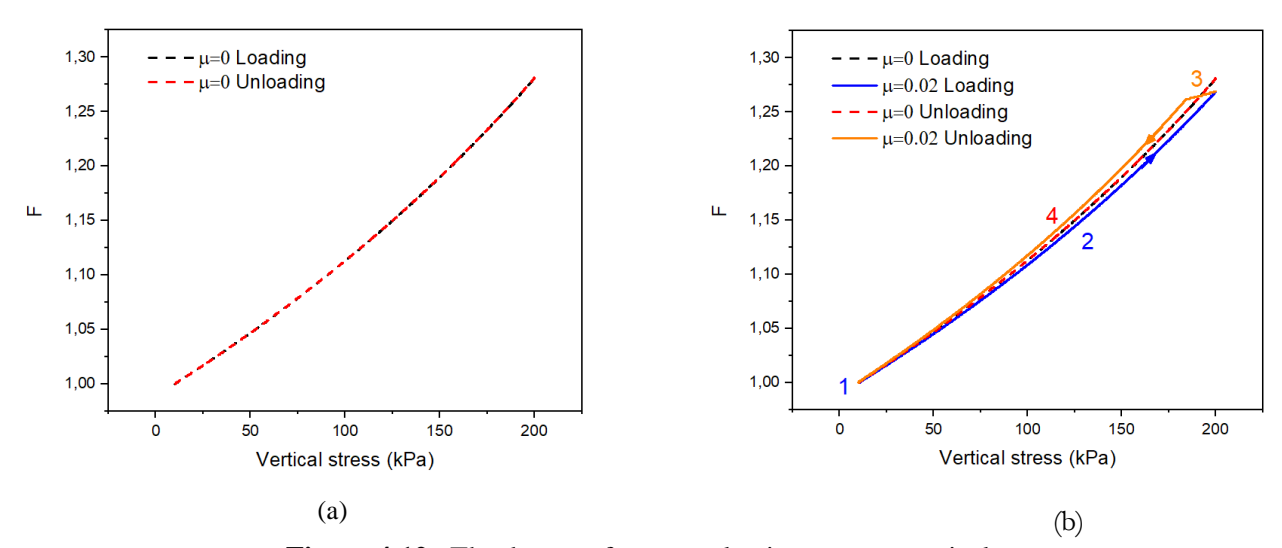


Figure 4.12. The degree of structural anisotropy vs vertical stress, (a) frictionless grains, (b) grains with friction.

This figure shows that for frictionless grains, the degree of structural anisotropy increases with vertical stress increase and decreases with vertical stress decrease on the same path. However, for rough grains (with friction), the variation of F follows two different paths during the loading and unloading, due to the presence of the friction forces. As a result, the F variation follows a loop for a loading-unloading cycle.

Figure 4.13a shows the evolution of K_0 for a loading-unloading cycle in case of low intergranular friction coefficients ($\mu=0$, $\mu=0.02$). Again, for rough grains, K_0 evolves following a loop shape during the loading and unloading cycle. The branches of the loops of Figures 4.12b and 4.13a may be described as follows:

- (1) Loading with a frictional force below the coulomb's slip threshold; in this case, there is no sliding, the change in the contacts orientation is negligible, F remains almost constant, K_0 decreases given that the vertical stress increases while the horizontal stress undergoes little variation.
- (2) Loading with a frictional force close the coulomb's slip threshold; the load increasing produces an intergranular slip, F increases as contact orientation tends towards the vertical. K_0 increases proportionally to F (according to Eqs.4.10 and 4.11).
- (3) Unloading with a frictional force less than the coulomb's sliding threshold; in this phase, the frictional force changes direction by passing through zero, the sliding is locked, the change in the contacts orientation is negligible, F remains almost constant, K_0 increases since the vertical stress decreases while the horizontal stress undergoes little variation.

(4) Unloading with a frictional force close to the coulomb's slip threshold; the load decreasing produces an intergranular slip, F decreases as contacts orientation tends towards the horizontal. K_0 decreases proportionally to F (according to Eqs4.10and 4.11).

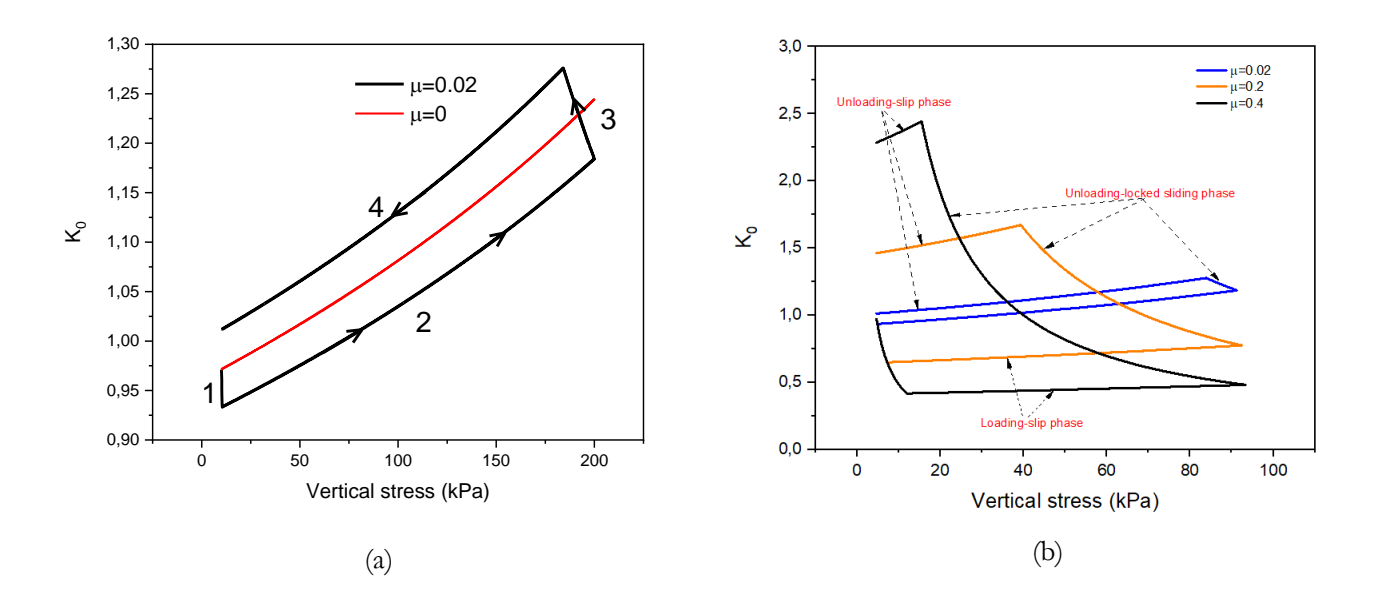


Figure 4.13. Evolution of K_0 in terms of the applied vertical stress. (a) Low friction coefficient, (b) Different friction coefficients.

Figure 4.13b shows the variation of K_0 in terms of the applied vertical stress for different coefficients of friction under a loading-unloading cycle. This figure indicates that when the friction coefficient increases, the loading sliding phase exhibits little change, the unloading locking phase becomes more significant and the unloading sliding phase decreases, consequently there is a residual slip maintained in the system after unloading. In soil mechanics this effect results in the increase of the over-consolidation ratio. It is worth noting that for natural soils, intergranular friction is relatively high i.e. $\mu \ge 0.4$, thus friction forces become a determining parameter on K_0 for an overconsolidated soil as illustrated by Figure 4.13b. Besides, the loops corresponding to the high friction coefficients of figure 4.13b explain well the effect of stress history on K_0 in the oedometric experiment, plotted in Figure 4.4.

4.6. Summary discussion

The coefficient of lateral earth pressure at rest (K_0) is an important quantity in geotechnical engineering, as it is involved in the design of many geotechnical structures. Research on the subject

has indicated that this coefficient is influenced by various material and state factors, but complete agreement on the effect of some factors on this coefficient is still lacking. Using 2D discrete element modeling, we aim in this work to contribute to a better understanding of the underlying physics involved in this coefficient, focusing in particular on the effect of loading history on this coefficient. Single-cycle and multiple-cycle oedometer tests are carried out on a granular sample, and an analysis of macromechanical and micromechanical parameters is performed. For a single-cycle test, obtained results showed that the shape of variation of K_0 with applied vertical stress is very similar to that given by the well-known Mayne and Kulhawy (1982) empirical formula. From a quantitative point of view, applying fitting coefficients to this empirical formula, as proposed by Zeng and Ni (1999), gives a perfect match between numerical and empirical results as shown in Figure 4.4. For a three-cycle loading-unloading test, it is shown that in the overconsolidation state, K_0 evolves according to a loop composed of two loading and unloading curves, with the loading curve always below the unloading curve. Furthermore, it is shown that K_0 in the unloading phase increases slightly as the loading cycles progress (Fig4.5).

Micromechanical analysis has shown that in the normally consolidated state, for an isotropic stress state, contact orientation is also almost isotropically distributed. The slightest deviation from stress isotropy quickly leads to significant anisotropy in the fabric tensor describing the orientation of contacts in the sample, with contacts perpendicular to the load direction becoming more dominant. For the oedometer test, as the load is vertical, horizontal contacts and, accordingly, horizontal friction forces increase rapidly at the start of loading (Fig. 4.6 and Fig.4.7), resulting in a sharp decrease in K_0 (Fig.4.4). During unloading, the sample becomes increasingly overconsolidated, with vertical contacts becoming more frequent and may even become more dominant than horizontal contacts (Fig. 4.6). The increase in vertical contacts leads to an increase in horizontal stress and, consequently, an increase in K_0 (Fig.4.4). Besides, it is shown in this analysis that the change in the fabric tensor is mainly due to the differential change in the number of contacts in the different directions as the load varies. Thus, the isotropic change in the number of contacts does not influence the fabric tensor and is not expected to have a significant effect on K_0 .

The rose diagram plotting the number of contacts per direction showed that there is a change in contact orientation between the two states; before and after a loading cycle (Fig.4.8). However, this change appears too small to be the only cause of the significant variation in K_0 . On the contrary, the rose diagram representing the intensity of normal contact forces per direction, showed a significant change (Fig.4.9). Thus, it is concluded that the increase in K_0 between the initial state and after a loading cycle results, in addition to the change in contact orientation, from a change in the intensity of the forces acting on these contacts. Therefore, the anisotropy of the fabric tensor can give

a qualitative description of the K_0 trend, which depends on the dominant direction of the contacts, i.e. K_0 is low when horizontal contacts are dominant and K_0 is high when vertical contacts are dominant. However, from a quantitative point of view, the value of K_0 is also influenced by the intensity of the contact forces in the different directions.

An analysis of the effect of intergranular friction is carried out using a simple three-grain model. This analysis showed that the change in orientation of existing contacts acts in the opposite direction to the observed change in fabric tensor for a granular sample subjected to oedometer loading (Fig. 4.12 vs Fig. 4.6b). This confirms that the differential variation in the number of contacts per direction is the main cause of the change in fabric tensor in the granular sample (Fig. 4.6). This analysis also explained the formation of a loop according to which K_0 changes during a loading-unloading cycle. This loop results from locking and sliding phases in the contacts depending of tangential force level with respect to the Coulomb sliding threshold as illustrated by Figure 4.13. This shows that the evolution of K_0 highlighted in the oedometer test is due to intergranular friction, such a parameter has therefore a determining effect on K_0 for an overconsolidated soil.

4.7. Conclusion

It is well known that the lateral earth pressure coefficient at rest (K_0) depends on the load to which the soil has been subjected during its history, i.e. its state of consolidation.

This chapter aims to understand the particle-scale physics involved in cyclically loaded granular soil and its effect on K_0 . To this end, a 2D discrete element modeling of a cyclic oedometer tests is performed. One-cycle and three-cycle tests are simulated and the resulting macromechanical and micromechanical parameters are analyzed.

The obtained results showed that the evolution of K_0 with loading is in good agreement with that of the will-known empirical formulas derived from experience. In addition, the three-cycle test showed that K_0 in the unloading phase increases slightly as the loading cycles progress. This may be attributed to the grain arrangement, which leads to more overconsolidation with increasing loading cycles.

Analysis of the variation of certain load-dependent micromechanical parameters, namely the fabric tensor, number of contacts and contact forces, allows the following main conclusions to be drawn:

- The evolution of the fabric tensor, which describes the relative distribution of contact orientations, as a function of load is mainly due to the differential variation in the number of contacts in the different directions.

- For an isotropic stress state, the distribution of contact orientations is almost isotropic, the deviation of the stress isotropy, even small, leads to a significant deviation from the isotropy of contact orientations.
- For a normally consolidated sample i.e. for the first cycle loading phase, horizontal contacts are more dominant, this increases horizontal components of friction forces and leads to a decrease of K_0 .
- For an overconsolidated sample, vertical contacts become more frequent, which increases horizontal components of contact normal forces and leads to an increase of K_0 .
- K_0 is not only influenced by the dominant orientation of the contacts, but it also depends on the intensity of the forces acting on these contacts.
- By using a simple three-grain model, it is highlighted that the evolution of K_0 according to a loop for a loading-unloading cycle in the oedometer test, is ultimately governed by intergranular friction. Such a parameter has therefore a determining effect on K_0 for an overconsolidated soil.

Chapter 05

APPLICATION OF DEM TO THE ANALYSIS OF THE ACTIVE AND PASSIVE LATERAL EARTH PRESSURES IN DRY GRANULAR SOILS

5.1. Introduction

Determination of active and passive earth pressures is a routine process in the design of geotechnical structures such as retaining walls and bridge abutments. Factors that influence the magnitude of the lateral earth pressures have been reported by Duncan and Mokwa (2001)[100]. For rigid retaining structures, soil properties (cohesion and internal friction angle), mode of wall movement, soil-wall roughness, and wall shape are considered the most influential parameters. Traditionally, the design of retaining structures was executed by using the limit equilibrium method where the earth pressures acting on the wall are derived from the classical earth pressure theories i.e., Rankine (1857) [101] or Coulomb (1776) [102]. Both the active and passive earth pressures are characterized by the active earth pressure coefficient (K_a) and the passive earth pressure coefficient (K_p) , which are dependent mainly on the internal friction angle of backfill soil (φ) , the friction angle of the soil-wall interface (δ) , the slope of the backfill and the wall geometry. In Rankine's earth pressure theory, the retaining wall is assumed to be smooth whereas Coulomb's theory considers the soil-wall friction. Many researchers have studied the earth pressure problems using various methods such as the limit equilibrium method, the method of stress characteristics, and the limit analysis method. Other studies also show that the retaining wall movement mode (translation or rotation) has a significant effect on lateral earth pressures distribution [103]. In addition to the theoretical approach [104-108] and the experimental approach [103] [109-118], numerical simulation has emerged as an effective alternative to study earth pressure distribution with greater flexibility to deal with a variety of boundary conditions and backfill material behaviors. In this context, the finite element method (FEM) was the most widely used [119–124].

Active and passive earth pressure problems are accompanied by localized deformation and failure. Deformation in granular materials tends to be localized along concentrated bands, known as shear bands. Modeling this localization phenomenon is important, as many engineering structure

failures are characterized by the formation and propagation of shear bands [125–130]. This is one of the difficulties of finite element modeling, given that this method is based on continuum mechanics, which relies on material behavior laws that need to be updated with the state of the material [131]. The DEM, because it is based on the theory of discrete mechanics, has obvious advantages for solving problems involving large deformations and failure [27] [132]. In addition, when dealing with the soilwall interface, the friction coefficient between the wall and sand particles can be given, this is very simple and the meaning is clear [133].

In this chapter, we use DEM to analyze the active and passive lateral pressures generated by a cohesionless granular soil on a vertical, smooth retaining wall. Simulation results are compared with those of Rankine theory.

5.2. Rankine limit states

Using the Mohr-Coulomb model, Rankine's theory describes the limit states of failure in a mass of soil subjected to displacements imposed on its edges. Consider a point in a normally consolidated granular soil mass at rest between smooth planes (Fig. 5.1a). In this situation, the principal directions are oriented along the vertical and horizontal axes, with the maximum principal stress being the vertical stress resulting from self-weight, and the minimum principal stress being the lateral earth pressure at rest. These two stresses are related by a proportionality relationship:

$$\sigma_{h0} = K_0. \, \sigma_{v0} \tag{5.1}$$

Where K_0 is the coefficient of lateral earth pressure at rest.

This state of stress is represented in figure 5.1b by a Mohr circle with the soil's Mohr envelope curves.

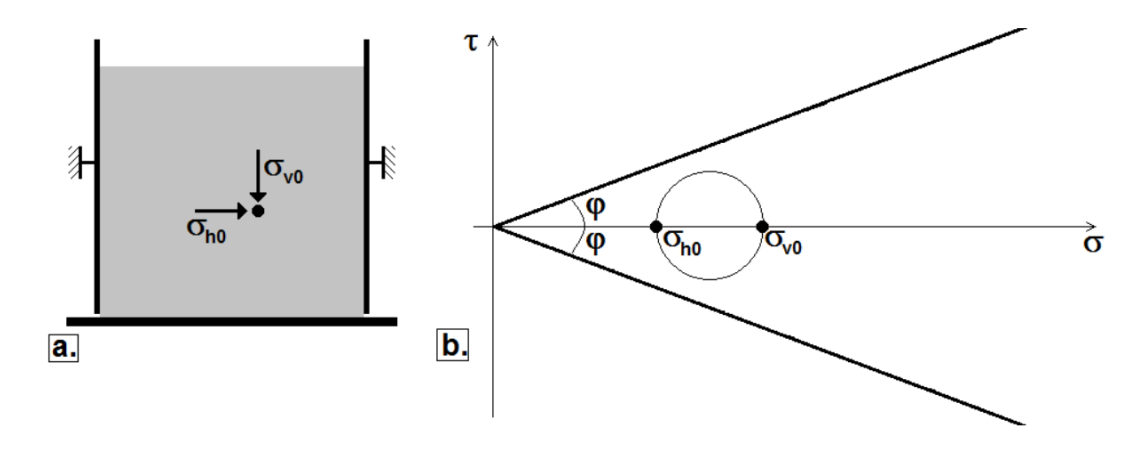


Figure 5.1.: a. Stress state in a normally consolidated soil mass resting between smooth planes; **b.** Corresponding Mohr circle and envelope curves

If one of the container's side walls is gradually moved outwards, the soil will progressively relax (Fig. 5.2a): the vertical stress will remain unchanged ($\sigma_v = \sigma_{v0}$), but the horizontal stress will gradually decrease (successive circles in Fig. 5.2b. However, Mohr's envelope indicates that this stress cannot decrease indefinitely without leading to material failure, as Mohr's circle eventually becomes tangent to the envelope lines: the material thus becomes in a state of failure and "follows" the side walls by applying a constant horizontal stress denoted σ_h .

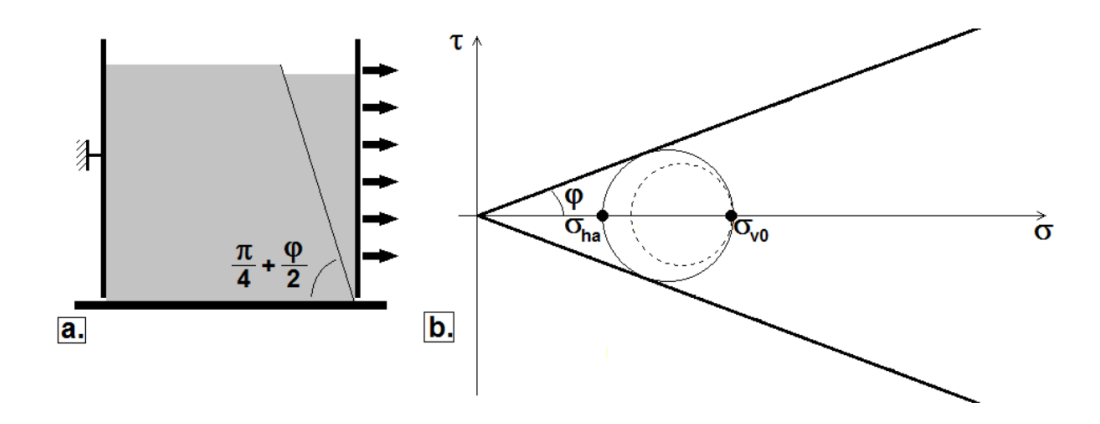


Figure 5.2.: Active limit equilibrium. a. Failure shape; b. Corresponding Mohr circles.

In this case, the soil is in "active limit equilibrium", or "active state", the horizontal and vertical stresses are related by:

$$\sigma_{ha} = K_a.\,\sigma_v \tag{5.3}$$

The coefficient K_a is referred to as the "active state earth pressure coefficient". Using the Mohr plane (Fig. 5.2b), this coefficient can be directly related to the soil's angle of friction as follows:

$$K_a = tan^2(\frac{\pi}{4} - \frac{\varphi}{2}) \tag{5.4}$$

In the active state, a slip line develops, and a 'wedge' of material detaches from the mass to follow the moving wall (Figure 5.2a).

Figure 5.3 illustrates the failure surface and the detached soil wedge, obtained from physical reduced-model modeling combined with the image correlation technique.

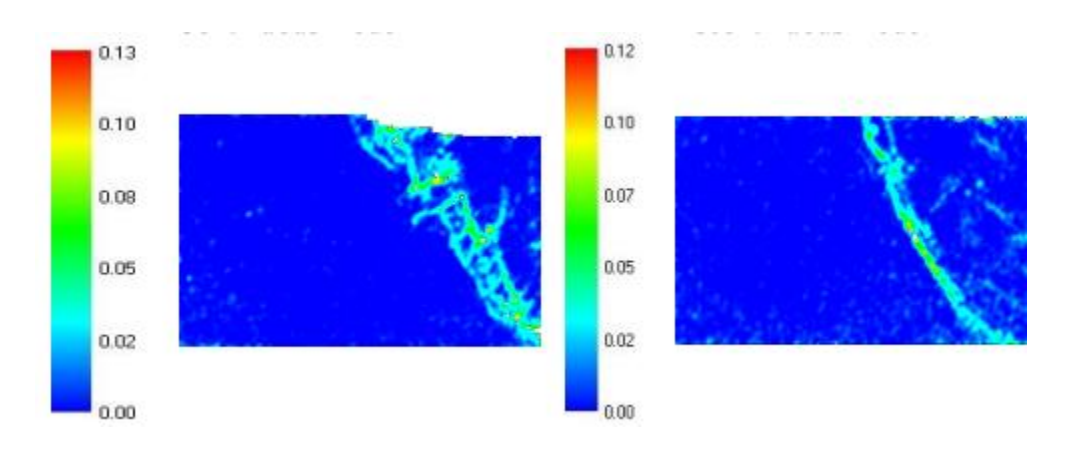


Figure 5.3: Experimental failure mode in active limit state [134].

In another situation, if the side wall is moved from its resting position towards the soil mass (Fig. 5.4a), the material becomes compressed. The vertical stress does not change but, in contrast, the horizontal stress progressively increases. It passes through a state of isotropic stress (Fig. 5.4), then as it exceeds the vertical stress, it becomes the maximum principal stress. As this stress increases, Mohr's circle becomes tangent to the envelope lines, and a new state of failure is reached, it is the "passive state". Horizontal stress reaches a maximum value expressed as:

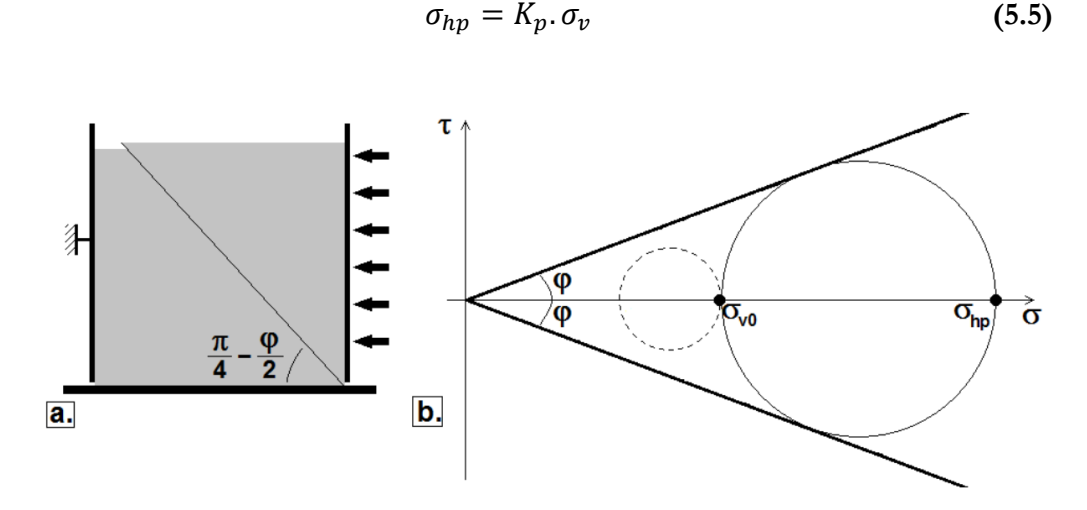


Figure 5.4. Passive limit equilibrium. a. Failure shape; b. Corresponding Mohr circles.

The coefficient K_p is referred to as the "passive state earth pressure coefficient". Using the Mohr plane (Fig. 5.4b), this coefficient can be directly related to the soil's angle of friction as follows:

$$K_p = tan^2(\frac{\pi}{4} + \frac{\varphi}{2}) \tag{5.6}$$

At passive state, a slip line different from that of active state develops, and a 'wedge' of material (with a significantly larger volume) detaches from the mass and moves with the wall (Figure. 5.4a).

5.3. Lateral forces on a vertical wall

In the design of retaining walls, the resultant of the lateral earth pressures on the wall is an important information. This resultant does not change significantly if it is calculated using the Coulomb or Rankine method. In addition to the value of the lateral earth pressure resultant, its point of application is an important design issue. Rankine's method gives the resultant at one third of the wall height from the base. For a backfill with a horizontal surface and without overload (Fig. 5.5a), the resultant lateral pressure P, which is equal to the area of the load diagram, is assumed to act at a height of H/3 above the base of the wall, H being the height of the surface subjected to pressure.

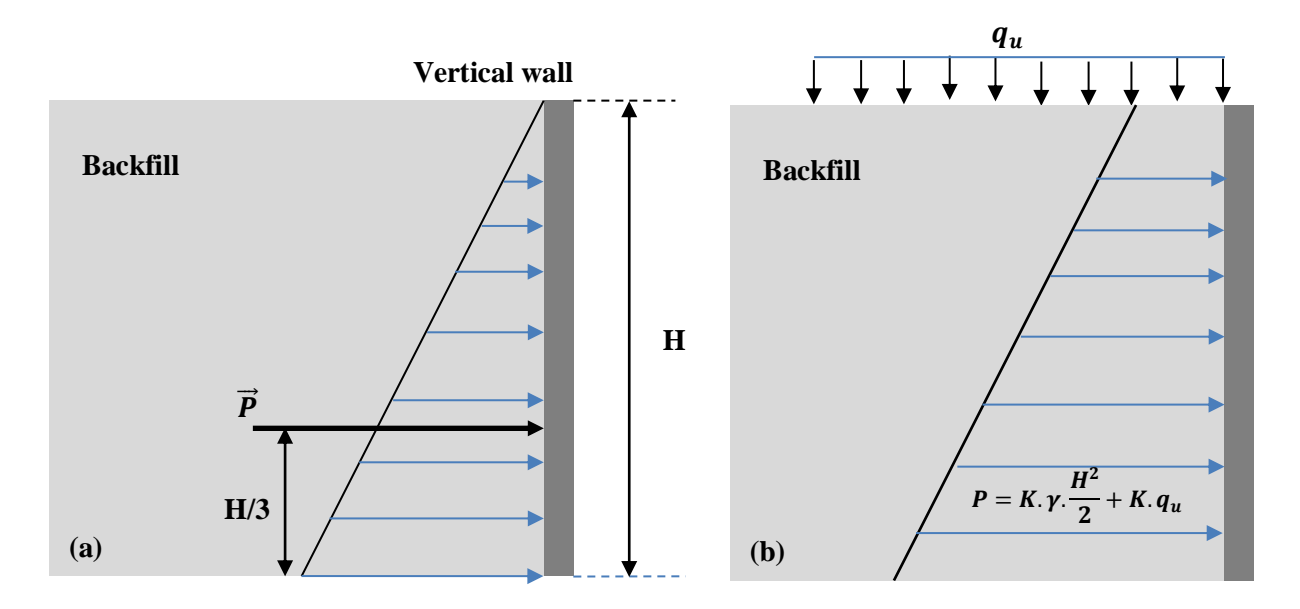


Figure 5.5: lateral pressure distribution acting on vertical wall:(a) without surcharge, (b) with uniform surcharge.

The lateral pressure is obtained by integration as follows:

$$P = \int_0^H K. \gamma . y. dy \tag{5.6}$$

Where γ is the specific weight of the sample.

At rest state:

$$P_0 = K_0 \cdot \gamma \cdot \frac{H^2}{2} \tag{5.7}$$

Active state:

$$P_a = K_a \cdot \gamma \cdot \frac{H^2}{2} \tag{5.8}$$

Passive state:

$$P_p = K_p. \gamma. \frac{H^2}{2} {(5.9)}$$

For a backfill with a horizontal surface and with an overload intensity q_u per unit area (Fig. 5.5b), the vertical pressure increment at any depth will increase by q_u . The increase in the lateral pressure due to this surcharge will be $(K \times q_u)$. Hence lateral pressure at any depth is given by:

$$P = K.\gamma.\frac{H^2}{2} + K.q_u {(5.10)}$$

5.4. Active and passive pressure mobilization displacements

As mentioned above, the active and passive states are reached after the development of the shear surface; this development phase requires minimal wall displacements. Figure 5.6 illustrates the variation in lateral earth pressures as a function of wall displacement, with S_a and S_p being the displacements corresponding to the passive and active states respectively.

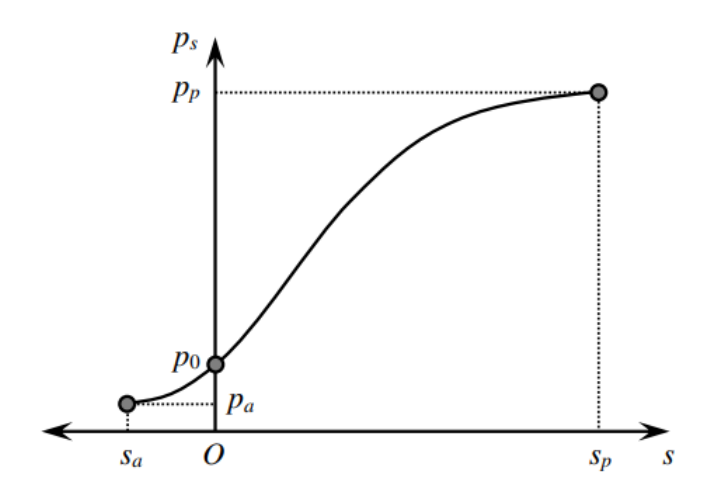


Figure 5.6: Variation of earth pressure with displacement

Terzaghi (1934) [111] experimentally investigated the magnitude of displacement required to reach plastic equilibrium in the active state (S_a). He concluded that this displacement was around H/1000 (H: height of a retaining wall) for dense sandy soils and slightly greater than H/1000 for cohesive-frictional soils. Later, several studies focused on estimating this displacement [135-137]. Experimental studies show that the main factor influencing this displacement is soil density. [138] report that in translational mode, the wall displacements required to achieve a passive state for loose and dense embankments are 8.9% and 6.8% of wall height, respectively. Different values of S_a and S_p are shown in the table 5.1, where S_a , S_p are displacements required to mobilize the full active and passive earth pressure respectively.

	Clough and Duncan (1991)			Becker and Moore (2006)		
Type of backfill	s_a	s_p	s_p/s_a	s_a	s_p	s_p/s_a
Dense sand	0.001H	0.01H	10	0.001H	0.02H	20
Medium sand	0.002H	0.02H	10	_	_	_
Loose sand	0.004H	0.04H	10	0.004H	0.06H	15
Stiff cohesive		_	_	0.01H	0.02H	2
Soft cohesive	_	_	_	0.02H	0.04H	2
Compacted silt	0.002H	0.02H	10			_
Compacted lean clay	0.01H	0.05H	5			_
Compacted fat clay	0.01H	0.05H	5	_	_	_

Table 5.1. Approximate Displacement Required to Mobilize Active and Passive Earth Pressures

Note: H = height of wall.

5.5. Discrete element modeling of passive and active earth pressure test

5.5.1. Model dimensions

Figure (5.7) shows the model used to model lateral earth pressure in the active and passive states. The retaining wall is modeled as a smooth rigid wall with a height of 6 cm. The width of the model is deliberately chosen to be large enough to avoid the influence of the fixed wall on the formation of the shear surface for both active and passive states.

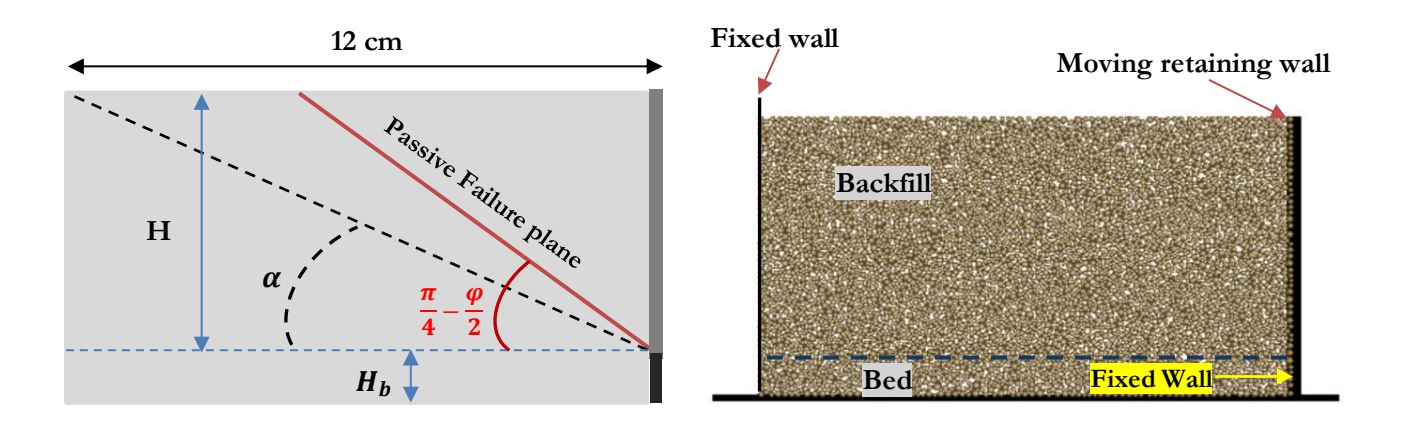


Figure 5.7: Model dimensions and boundary conditions.

In the passive state, the fracture surface can drop below the wall base, as shown in Fig. 5.8. For this reason, and to avoid the influence of the model base on the free development of the fracture surface, the base of the moving wall starts at a height $H_b = 0.5cm$ above the model base.

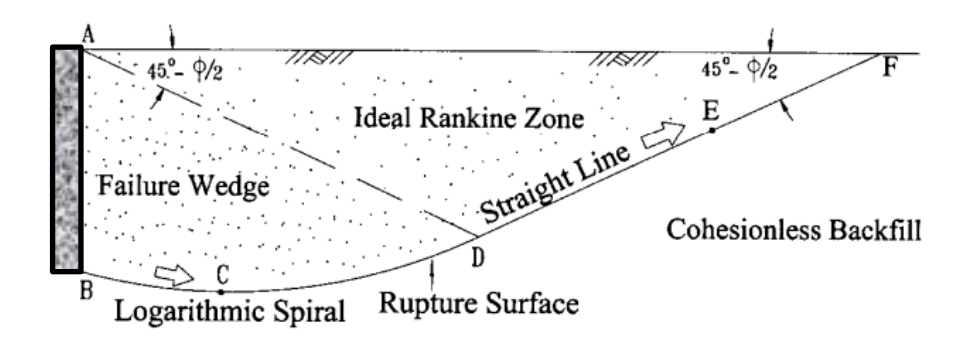


Figure 5.8: Passive wedge calculated with Terzaghi's log-spiral method [117].

5.5.2. Backfill properties

The Backfill is composed of 4500 polydisperse circular shaped particles, with the same physico-mechanical proprieties as described previously (see chapter 3). The Backfill is built using the fixed-grid method, then subjected to a uniform loading (q_u) via a flexible chain of 120 grains (Fig. 5.9) that have the same radius $r_c = 0.5mm$ and a higher specific weight determined from the target load. A model for flexible fibers consisting of series of spheres proposed by Kalonji and Jean-François (2012)[139] was used, where the grains are connected by elastic springs whose stiffnesses are typically governed by simple contact models (figure 5.10).

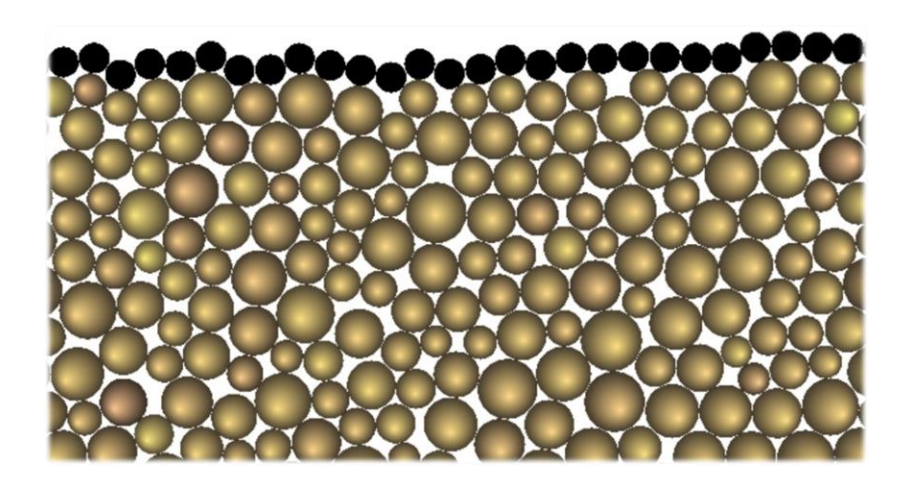


Figure 5.9: Snapshot of the backfill with flexible load chain above (black disks).

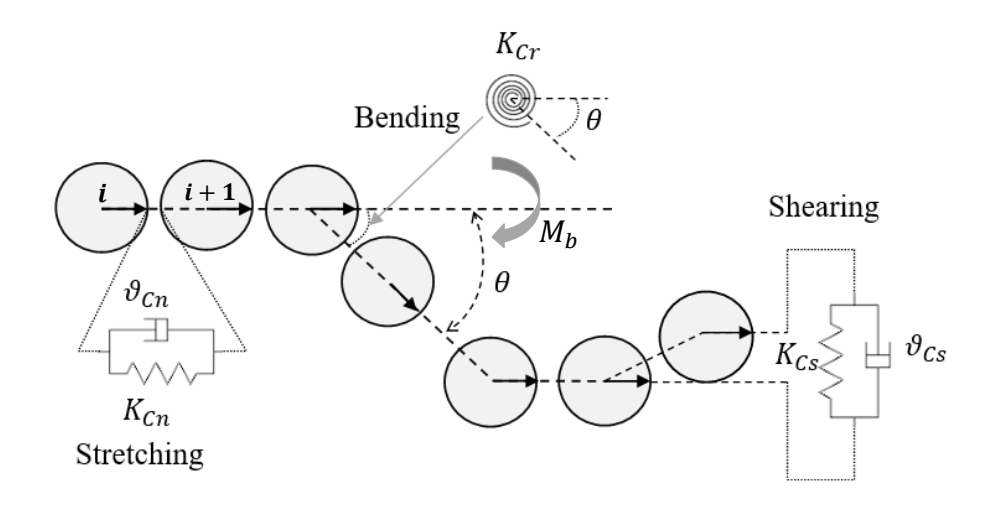


Figure 5.10: Flexible chain contact's model.

The models used in this work to calculate the interaction forces between the chain grains are as follows:

• Normal force

$$F_{cn} = -\delta_n K_{Cn} - \vartheta_{Cn} V_n$$

• Shear force

$$F_{cs} = K_{Cs}\delta_s + \vartheta_{Cs}V_s$$

• Bending moment

$$M_b = K_{Cr}\theta$$

Where δ_n is the normal overlap between two successive grains, δ_s is the relative tangential displacement described previously in chapter 3 and θ being the angle of relative rotation between two grains with respect to the initial rectilinear state. The spring stiffness and damping coefficients for each contact model are shown in Table 5.2.

Table 5.2. microscopic flexible chain grains parameters

Characteristics	Symbol	Value	Unite
Normal stiffness	K_{Cn}	1200000	N/m^2
Tangentiel stiffness	K_{Cs}	960000	N/m^2
Normal viscous damping coefficient	$\vartheta_{{\cal C}n}$	41.38	kg/s^{-1}
Tangentiel viscous damping coefficient	$artheta_{\it Cs}$	33.10	kg/s^{-1}
Bending resistance stiffness	K_{Cr}	0.5	_
Gravity	g_c	Variable	m/s^2
Density of grains	ρ	2600	kg/m³

The specific weight of the flexible chain grains is increased by increasing the gravity acceleration (g_c) applied to each grain until the target pressure is reached. The uniform load is thus calculated as follows:

$$q_u = \frac{120\pi r_c^2 \cdot \rho \cdot g_c}{120 \times 2 \times r_c}$$
 (5.11)

$$q_u = \frac{\pi r_c \cdot \rho \cdot g_c}{2} \tag{5.12}$$

With: $r_c = 0.0005m$ and $\rho = 2600Kg/m^3$ so:

$$q_u = 2.041 \ g_c \tag{5.13}$$

It should be noted that, to obtain a normally consolidated sample, we first create a sample under isotropic compression without intergranular friction, i.e. under equal vertical and horizontal stresses ($\sigma_v \approx \sigma_h = 5kPa$), hence $K \approx 1$. Next, the sample is subjected to the desired vertical stress by gradually increasing g_c . In this phase, the vertical edges are kept fixed, i.e. horizontal displacement is prevented. Figure 5.11 shows the evolution of the lateral pressure coefficient as a function of the vertical stress applied across the flexible chain. It can be seen that from a vertical load of 15 kPa, the ratio between horizontal and vertical stresses is close to the value 0.5, then it stabilizes around this value even if vertical stresses continue to increase.

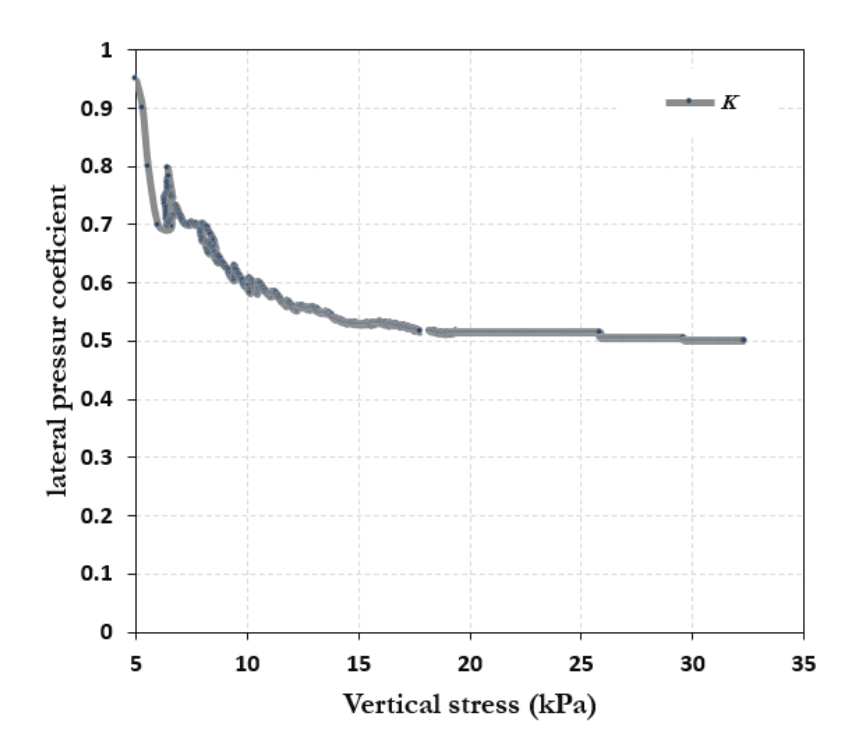


Figure 5.11: lateral pressure coefficient variation under a variable vertical stress.

5.6. Lateral earth pressure distribution at rest

To plot the distribution of lateral earth pressures at rest, we subdivided the backfill into five layers of equal thickness (Fig. 5.12), then calculated the lateral pressure acting on the wall through each layer. This pressure is calculated as the sum of the normal forces in the grain-wall contacts in each layer, divided by the layer thickness. In this application, the flexible chain grains gravity g_c is set to $15000 \, m/s^2$ which give a vertical pressure $q_u = 30 \, kPa$.

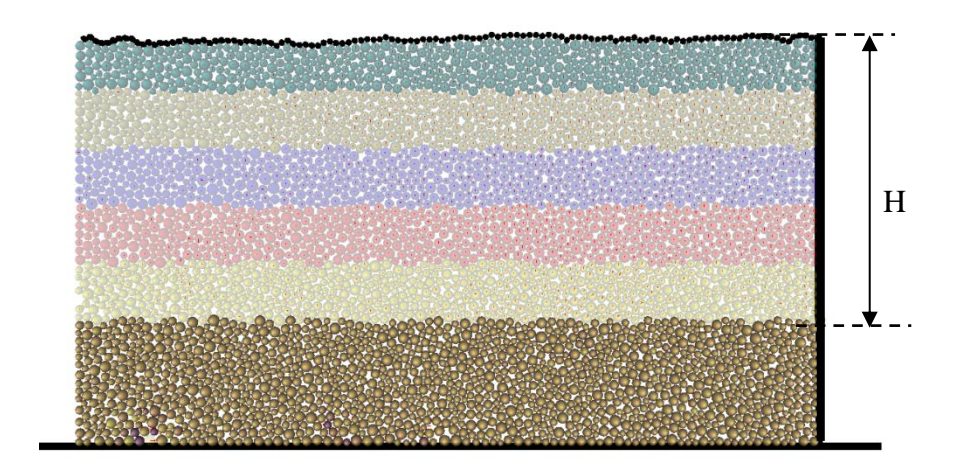


Figure 5.12: Backfill decomposition into 5 layers.

The lateral pressure distribution acting on the retaining wall at-rest is presented in figure 5.13. It is clear that the distribution of lateral pressures at rest is almost constant, indicating that stresses due to overloading are dominant. The resulting average lateral pressure is 15 kPa, giving a coefficient of lateral pressure at rest:

$$K_0 = \frac{\sigma_h}{\sigma_v} = \frac{15}{30} = 0.5$$

Terzaghi (1943) indicated that arching may play a role in the distribution of loads on retaining structures. Although the term arching has been accepted in geotechnical literature, the concept is not linked to the formation of a physical arch, but rather to a stress distribution in which the stiffer components of the system attract more loads. Arching means that stresses are transferred from the plastified zones to the elastic zones of the soil.

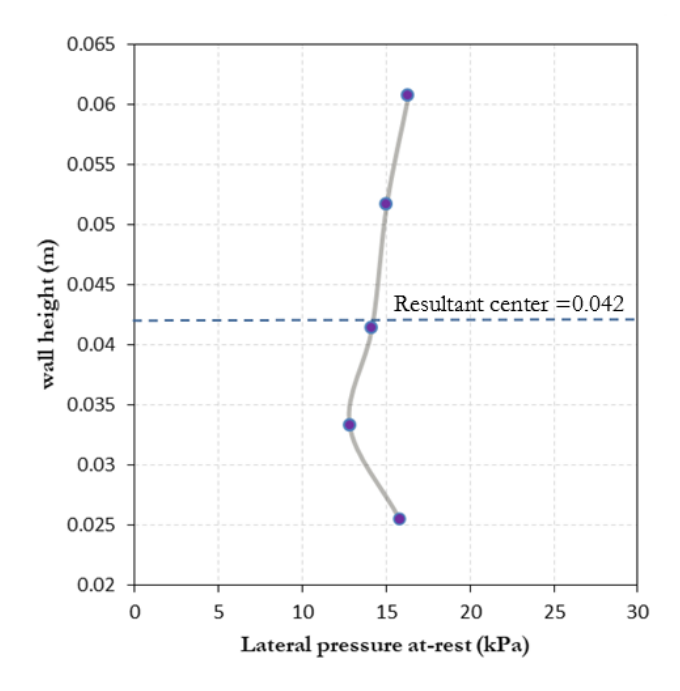


Figure 5.13: Lateral Pressure distribution at-rest without wall-backfill friction.

Many researchers have studied active earth pressure on a rigid retaining wall considering arching effect. [140] proposed a differential equation for pressure in silos. He provided a theoretical basis for understanding the effect of arching. Based on this theory, [141] and [142] proposed procedures for estimating the nonlinear pressure distribution of active earth pressure on a wall. [143] showed that lateral earth pressure behind a retaining wall depends on the wall's mode of movement, i.e. translation or rotation of the wall around the top or bottom and that the pressure distribution is nonlinear. This non-linearity is attributed to arching effect [144]. The arching effect is much more apparent during the movement of the retaining wall, as shown in the next section.

In granular media, force chains are a key concept that allows to understand the stress distribution. These chains represent preferential pathways through which forces are transmitted. Indeed, forces are not uniformly distributed throughout the material; some particles bear higher loads, forming active force chains, while others experience relatively low stress. The force chains are dynamic, continually evolving in response to particle movements and loading conditions. They can break and reform as the material deforms. Under loading, these chains tend to align with the direction of the principal stresses. Moreover, they significantly contribute to the overall rigidity of the system and play a crucial role in determining the material's mechanical strength.

In discrete element analysis, force chains are used to visualize and quantify stress distribution within a granular material. They are represented by segments connecting the centers of the grains in contact. The thickness of each segment is proportional to the intensity of the normal force [7].

Figure 5.13 shows the force chains distribution inside the backfill. Under a load $q_u = 30kpa$, these chains clearly demonstrate that the widest chains are oriented vertically, suggesting the dominance of the main vertical stresses. In addition, the intensity of horizontally oriented force chains along the retaining wall varies from with depth, indicating that the vertical distribution of lateral pressures is not uniform.

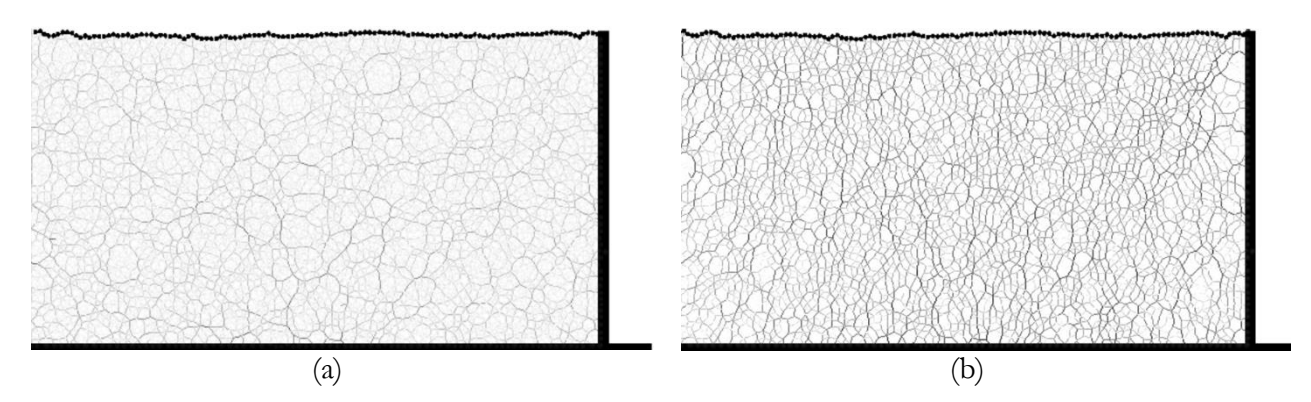


Figure 5.14. Force chains distribution inside the backfill without wall-backfill friction.

(a) Isotrope phase, (b) at $q_u = 30kpa$.

5.7. Active and passive states simulations

In this section the lateral pressure coefficient K, defined as the ratio between the effective horizontal stresses (σ_h) and the vertical stresses (σ_v) is analyzed for the active and passive states described above. In these simulations, horizontal stress is calculated as the ratio of the resultant of grain actions on the retaining wall to the height of the wall. Whereas vertical stress is equal to the pressure applied across the flexible chain q_u . In both passive and active states, and for all simulations, the wall translation rate is set to 0.0001m/s.

a. Moved soil volume

The active state results from the movement of the retaining wall in the direction of lateral pressure, allowing the embankment to relax and deform laterally. This leads to increased shear stresses within the soil and a decrease in the lateral pressure. Ultimately, when the shear strength is reached in a certain zone, a shear surface develops, isolating a detached wedge from the rest of the soil. Figure 5.10a illustrates the volume of soil that moves behind a retaining wall in the active state.

The passive state results from the movement of the retaining wall in the opposite direction to the lateral pressures, which causes additional compression of the supported soil and leads to an increase in lateral pressure. Figure 5.10b shows the volume of soil displaced during the passive state, the shape obtained indicating a main slip plane starting from the base of the wall and extending

upwards with a slightly curved shape (highlighted in yellow). A secondary downward failure surface also appears (highlighted in green), which can be attributed to soil compression, isolating the compressed part from the rest of the soil.

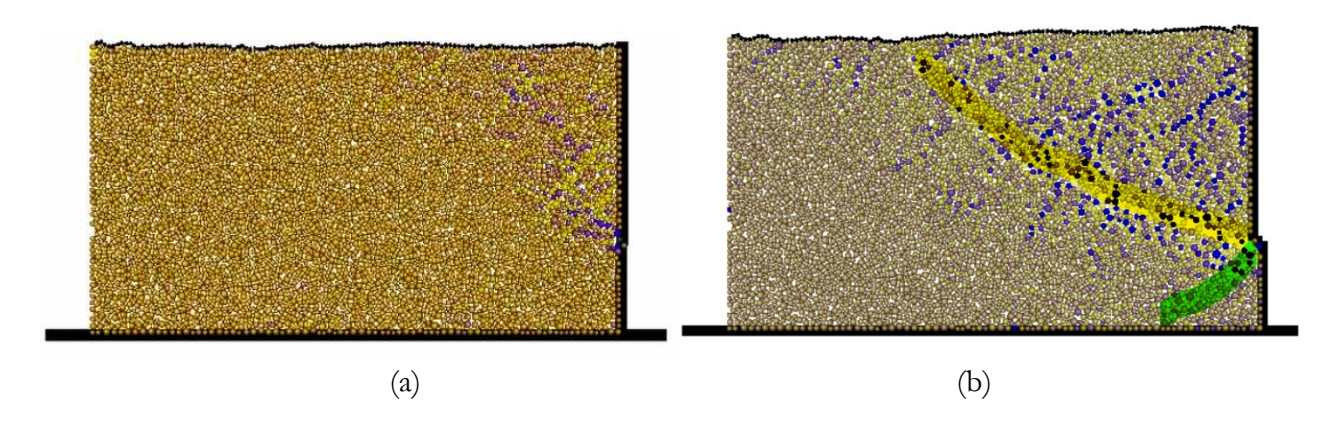


Figure 5.15: The sliding wedge and shearing bands (a) active state, (b) passive state. (the blue-colored grains undergo more rolling movement)

b. Lateral stress evolution

The evolution of horizontal stresses as a function of wall displacement is illustrated in figure 5.16, highlighting distinct behaviors between the active and passive states. In the passive state, the horizontal stress was initially $15 \, kPa$, it increased significantly with wall displacement, reaching a peak of $90 \, kPa$. This increase reflects the soil's resistance to compression as the wall moves inward. After the peak, horizontal stress gradually decreases and stabilizes at around $75 \, kPa$. This behavior is similar to the shear behavior of dense sands. On the other hand, as the wall moves outwards, the horizontal stress decreases rapidly from its resting value ($15 \, kPa$) to a stable value of $11.5 \, kPa$, representing the lateral pressure of the active state. This rapid reduction in stress is characteristic of the soil's response to extensional shear. The different behavior in the passive and active states highlights the significant influence of the direction of wall displacement on stress evolution, with the passive state showing a peak behavior followed by a higher residual pressure, and the active state showing a monotonic decrease down to the lower residual pressure.

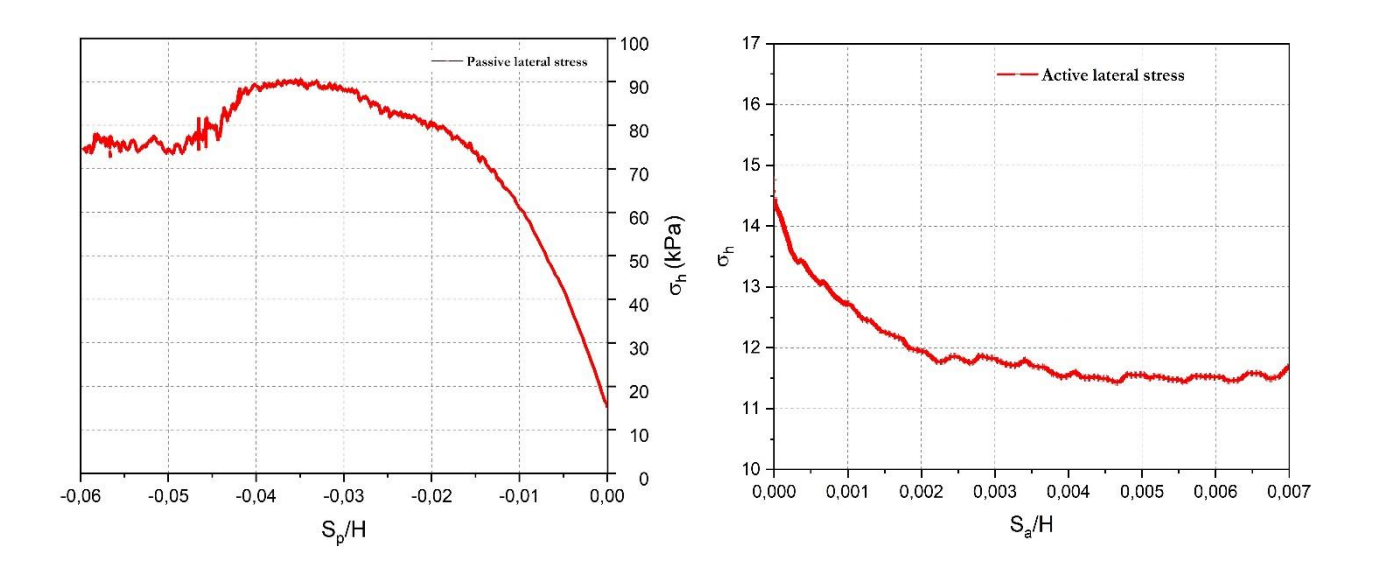


Figure 5.16: Lateral earth pressure. (left) passive state, (right) active state.

An analysis of the volume deformation during wall displacement is conducted. The void ratio during the passive tests is estimated as follows:

$$e = \frac{V_T - V_S}{V_S} = \frac{[(L \times H_T) - (H \times S_p)] - [\sum_{i=0}^{N-1} (\pi . r_i^2)]}{\sum_{i=0}^{N-1} (\pi . r_i^2)}$$

Where: V_s and V_T are the grains volume and sample volume respectively.

 $H_{\rm T}$ is the sample height calculated during the test as:

$$H_T = (H_{max} + H_0)/2$$

 H_0 is the initial sample height and H_{max} is the vertical position of the highest grain in the sample.

For the active state, it can be observed that the height of the backfill remains practically unchanged ($H_{max} \approx H_0$) until failure (see figure 5.15a). Consequently, the void ratio is calculated by the formula:

$$e = \frac{V_T - V_S}{V_S} = \frac{[(L \times H_0) - (H \times S_a)] - [\sum_{i=0}^{N-1} (\pi . r_i^2)]}{\sum_{i=0}^{N-1} (\pi . r_i^2)}$$

The evolution of the void ratio during the wall displacement is shown on figure 5.17. For the passive state, the soil exhibits contracting and then dilating behavior with increasing displacement. Initially, the void ratio decreases until a displacement ratio of $S_p/H \approx 0.017$ is reached, indicating a contracting phase where the material compacts under increasing lateral pressure. Then a dilating

behavior occurs until the end of the test, this phase should correspond to the phase of failure. On the other hand, for the active state, the behavior is essentially dilating with increasing displacement. This could be due to the reduction in pressure as the wall moves away, which allows the soil to expand, in addition to the development of failure, which makes the soil looser. These contrasting behaviors for the two states highlight the critical role of the stress path leading to the development of fracture, as the two failure limit states are reached by different stress paths; one by compression (passive state) and the other by extension (active state).

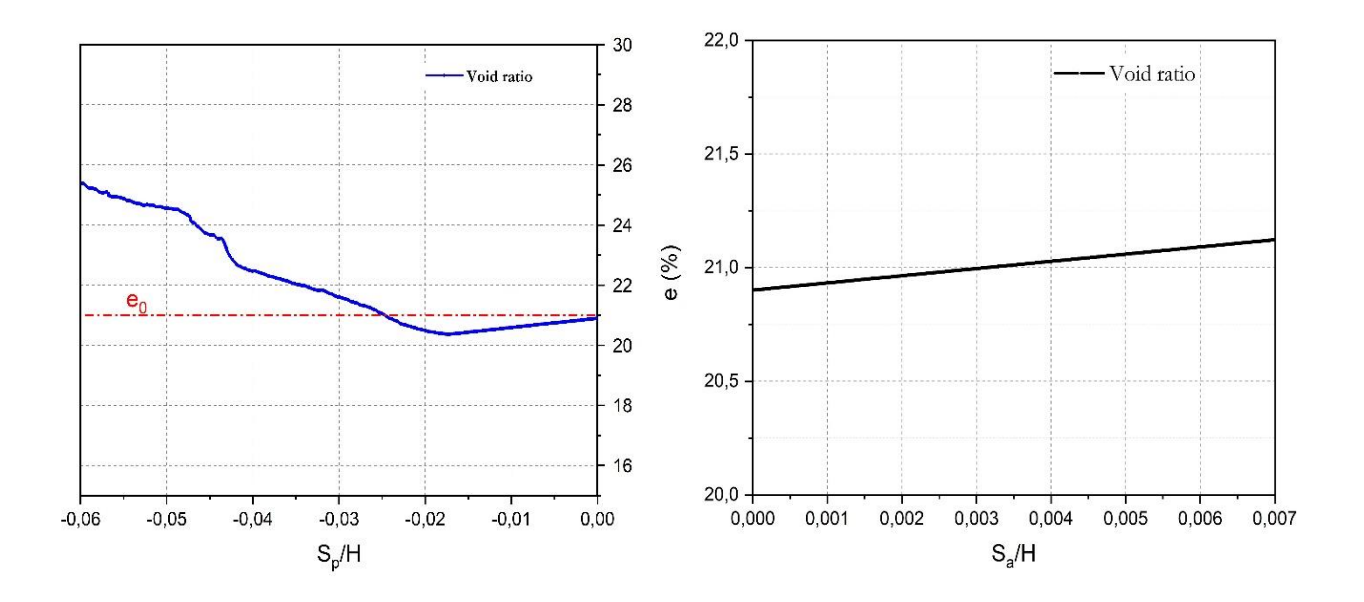


Figure 5.17: Void ratio. (left) passive state, (right) active state.

c. Passive and active earth pressure coefficients

Figure 5.18 shows the evolution of lateral earth pressure coefficients for both passive and active states. For the passive state, we note that the lateral pressure coefficient K_p is initially close to 0.5 and increases progressively as the retaining wall moves inwards, reaching a maximum value of 3 between displacements of 3H/100 and 4H/100. For the active state, a different trend is observed: the lateral pressure coefficient K_a also starts from an initial value close to 0.5, but decreases monotonically with wall displacement to stabilize at around 0.4. The displacement required to reach the active state is significantly smaller, it is about between 3H/1000 to 4H/1000. This shows that the material reaches the active state at much lower displacements than in the passive state. The lateral pressure coefficient is also much lower, remaining almost constant for larger wall displacement.

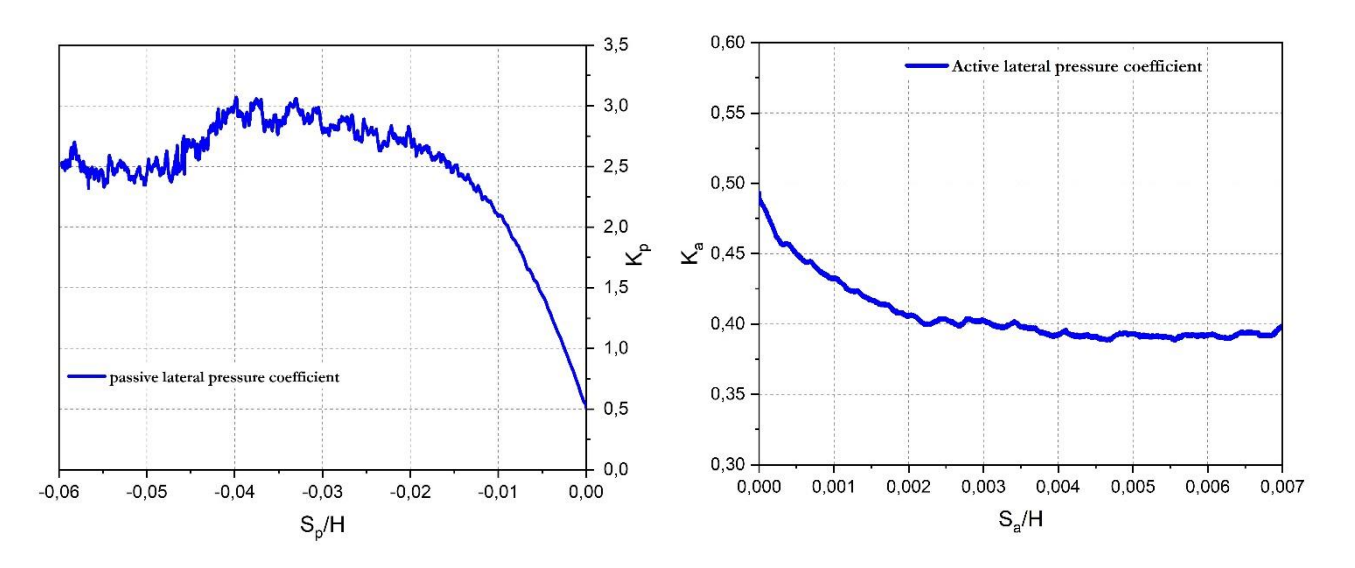


Figure 5.18: Lateral earth pressure coefficients. (left) passive state, (right) active state.

d. Lateral pressure distribution

In order to show the evolution of the pressure distribution on the retaining wall, the mean pressures at the middles of the five backfill layers were calculated at specific displacement ratios, for both the passive and active states. For the passive state, the measurements were taken at displacements $\frac{s_p}{H} = 0.01$ and 0.03, corresponding to an intermediate phase and the peak failure phase respectively. The corresponding pressure distributions are shown in figure 5.19. It could be observed that in the intermediate phase $\left(\frac{s_p}{H} = 0.01\right)$, the pressure is increasing almost linearly from the surface layer until the fourth layer. This result could be attributed to the compressibility of the soil between the shear strip and the wall. In fact, for layers where the wall is well away from the shear band (upper layers), the displacement of the wall is absorbed by the compressibility of the soil, which delays the increase in horizontal stress. On the other hand, for deeper layers, the shear band becomes close to the wall, so there is less soil compressibility and horizontal stress increases more rapidly. At a higher displacement $\left(\frac{s_p}{H} = 0.03\right)$, the failure band becomes developed over the entire height of the deposit, and the pressure distribution tends to become more uniform. Recall that the uniformity of the distribution results from the dominance of the load applied to the surface of the deposit in comparison with the soil's self-weight.

For the active state, the stress distribution was measured at a displacement ratio of $S_a/H = 0.001$ (figure 5.19, right). In this case, the lateral pressures decreased more significantly in the lower

layers. This finding could also be related to the narrow width of the sliding wedge in these layers. This small width allows less deformation of the soil and consequently less pressure in the intermediate phase. The nonlinear shape of the distribution could be attributed to arching effects.

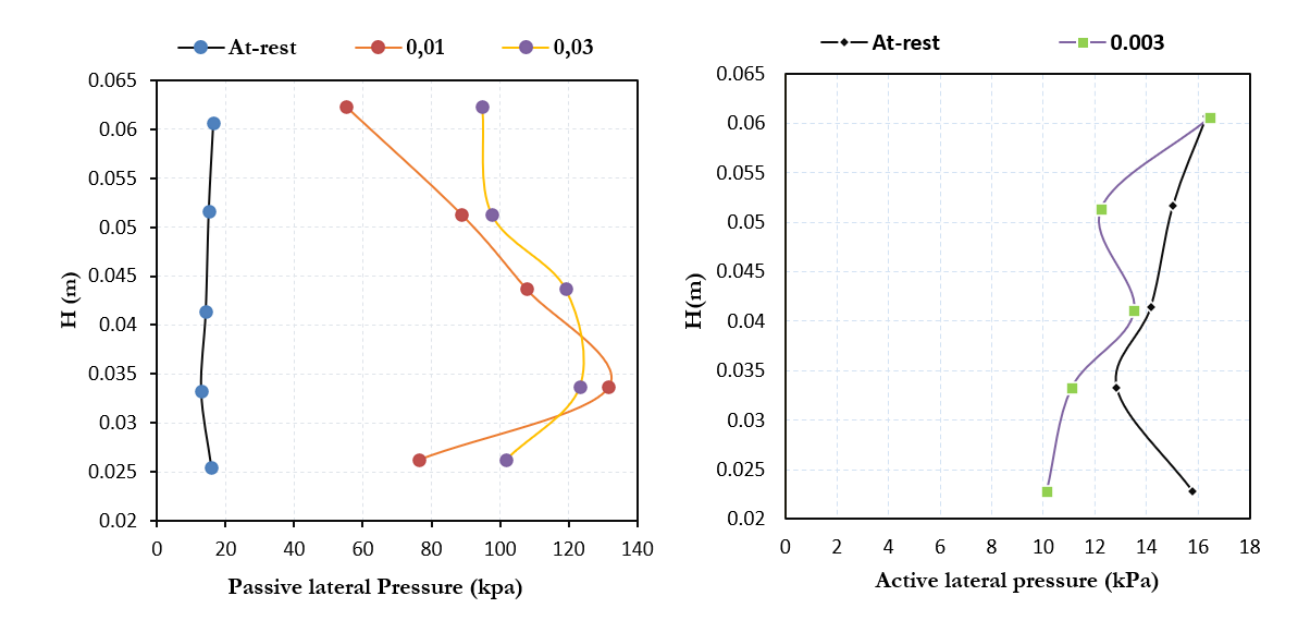


Figure 5.19: Lateral pressure distribution in backfill layers. (left) passive state, (right) active state.

5.8. Quantitative discussion of pressure coefficients with Rankine theory

The results obtained from the tests for both passive and active states show a good quantitative agreement with lateral pressure theory, particularly in terms of the lateral pressure coefficients. Qualitatively, in the passive state, the obtained peak lateral pressure coefficient $(K_p \approx 3)$ aligns well with the value calculated from Rankine's equation using the peak friction angle $(\varphi_{peak} = 30^\circ, \rightarrow K_p = \tan^2(\frac{\pi}{4} + \frac{\varphi}{2}) = 3)$. However, in the active state, the lateral pressure coefficient obtained $(K_a = 0.4)$, is slightly higher than that predicted by the Rankine equation using the peak friction angle $(\varphi_{peak} = 30^\circ, \rightarrow K_a = \tan^2(\frac{\pi}{4} - \frac{\varphi}{2}) = 0.33)$, but also slightly lower than that calculated using the critical state friction angle $(\varphi_c = 20^\circ, \rightarrow K_a = \tan^2(\frac{\pi}{4} - \frac{\varphi}{2}) = 0.49)$. These differences raise an important question: why do these deviations occur? In this context, we considered the influence of the stress path, as the passive and active states involve distinct stress paths. The evolution of stresses in the passive state follows typically the path of the compression shear test. While in the active state, the evolution of stresses follows an extensional shear test. This indicates that the deviation observed for the active pressure coefficient could result from the difference between the

stress paths.

5.9. Analysis of the effect of stress path on lateral pressure

5.9.1. A review on triaxial testing with different stress paths

To better illustrate the different stress paths, let us first examine the different cases of the triaxial test, which is the most popular test in soil mechanics. In triaxial testing, common stress paths followed during compression and extension tests include the conventional triaxial compression (CTC) path, where the axial stress σ_1 is increased while the confining pressure is held constant ($\Delta \sigma_3 = 0$), leading to an increase in the mean effective stress and an increase in deviatoric stress. Conversely, the conventional triaxial extension (CTE) path involves reducing the axial stress while maintaining constant confining pressure, resulting in a decrease in mean effective stress and an increase in deviatoric stress. Other stress paths include the constant mean effective stress (p) path, where the mean stress is kept constant while the deviatoric stress is varied, and the constant deviatoric stress (q) path, where the deviatoric stress is maintained while the mean stress is altered. These paths help characterize soil behavior under different loading conditions. Figure 5.21 illustrates various stress paths for the triaxial test, each representing distinct loading conditions.

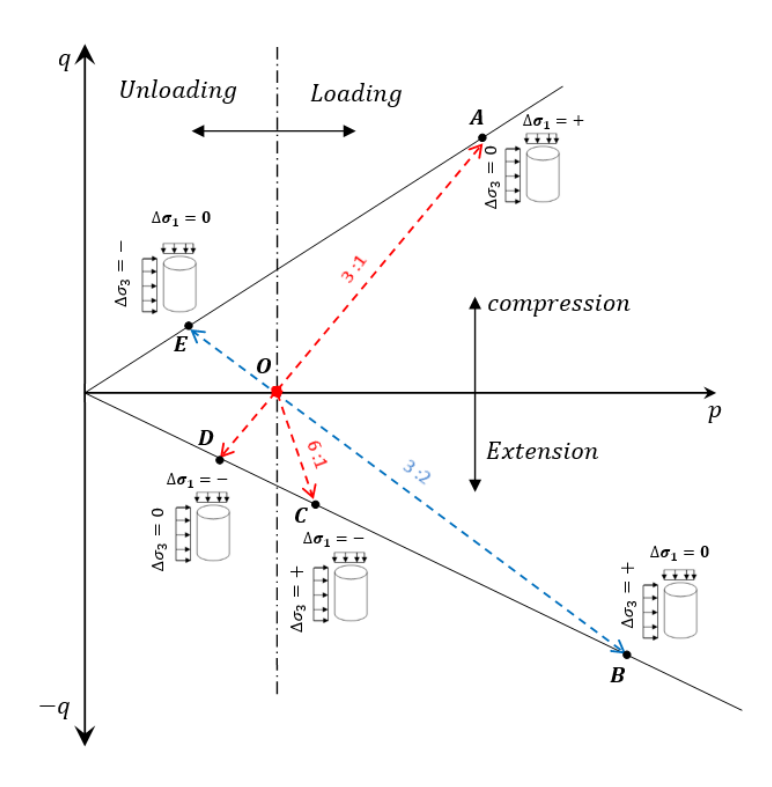


Figure 5.20: Triaxial total stress paths in p-q stress plane (drained test).

The first path, denoted by vector \overrightarrow{OA} , corresponds to a conventional compression path where the confining pressure remains constant while the axial stress increases. The second path, represented by vector \overrightarrow{OB} , is a conventional extension path where the axial stress is held constant, and the lateral stress is increased. The third path, indicated by vector \overrightarrow{OC} , depicts an extension path that maintains a constant mean stress by decreasing the axial stress while simultaneously increasing the lateral stress. The fourth path, shown by vector \overrightarrow{OD} , represents an extension path where the axial stress is reduced while the confining pressure remains unchanged. Finally, the fifth path indicated by vector \overrightarrow{OE} , is a compression path where the axial stress is kept constant, and the lateral stress is decreased.

A bibliographic review on triaxial tests conducted on sands under different stress paths reveals a wide range of insights into the mechanical behavior of granular materials. (Alain Corfdir 2008) (Theocharis; A 2016) have shown that the stress-strain response, strength, and deformation characteristics of sands are highly dependent on the loading path applied. Conventional compression paths, where the confining pressure is held constant while the axial stress is increased, typically result in contractive behavior followed by strain hardening, leading to peak strength. In contrast, conventional extension paths, where the axial stress remains constant and the lateral stress increases, often exhibit dilative behavior and lower peak strengths compared to compression paths. Additionally, tests involving constant mean stress paths or reduced axial stress paths highlight the influence of stress anisotropy and intermediate principal stress on sand behavior (Zhang, K 2018). These studies emphasize the importance of considering non-conventional stress paths, such as those encountered in actual geotechnical problems, to better understand the complex response of sands under varying loading conditions. The review underscores the need for advanced experimental and numerical approaches to capture the full spectrum of sand behavior under diverse stress paths.

5.9.2. Biaxial tests for passive and active pressure states

In order to analyze the effect of stress path on lateral earth pressure coefficients, we proposed to perform biaxial shear tests with different stress paths. In addition to the conventional biaxial compression test (CBCT) presented previously in section 3.7, which simulates well the passive state, we performed a biaxial compression unloading test (BUCT) designed to replicate the stress path in the active earth pressure condition. In this test, the vertical stress remains constant ($\Delta \sigma_1 = 0$), while the lateral stress decreases ($\Delta \sigma_2 = -$). This test corresponding to the triaxial stress path \overrightarrow{OE} shown in fig 5.21, is of particular interest as it simulates different cases commonly encountered in geotechnical engineering, such as the behavior of soil behind retaining walls or in excavation zones.

The same samples that were used for both tests; the conventional biaxial compression test (CBCT) and the biaxial compression unloading test (BUCT). Furthermore, in order to compare the results of the two types of test, we have opted to perform them under similar mean compressive stresses. To this end, it is assumed that the BUCT test comparable to a CBCT test already performed, is carried out under an initial confining stress equal to the major principal stress at failure of the CBCT test. Three CBCT tests were carried out with initial confining pressures of 50, 100 and 150 kPa. The maximum axial stresses at failure were 153, 307 and 452 kPa respectively. Consequently, the corresponding BUCT tests are conducted under these latter respective values of initial confining stress. Figure 5.21 shows the evolution of deviatoric stress for both types of shear test and for different average compressive stresses. Deviatoric stress is plotted as a function of vertical strain for CBCT tests and as a function of lateral strain for BUCT tests. For CBCT tests. The samples showed typical behavior of dense sand, characterized by a pronounced peak in deviatoric stress followed by a softening for higher strains. In contrast, for BUCT tests, the soil showed a behavior similar to that of loose sand, with a continuous increase in deviatoric stress without a distinct peak. The comparison highlights the influence of stress paths and confining pressures on the mechanical behavior of the materials, with the sand being initially dense, exhibiting a dense sand response under conventional compressive loading and loose sand-like behavior under lateral unloading conditions.

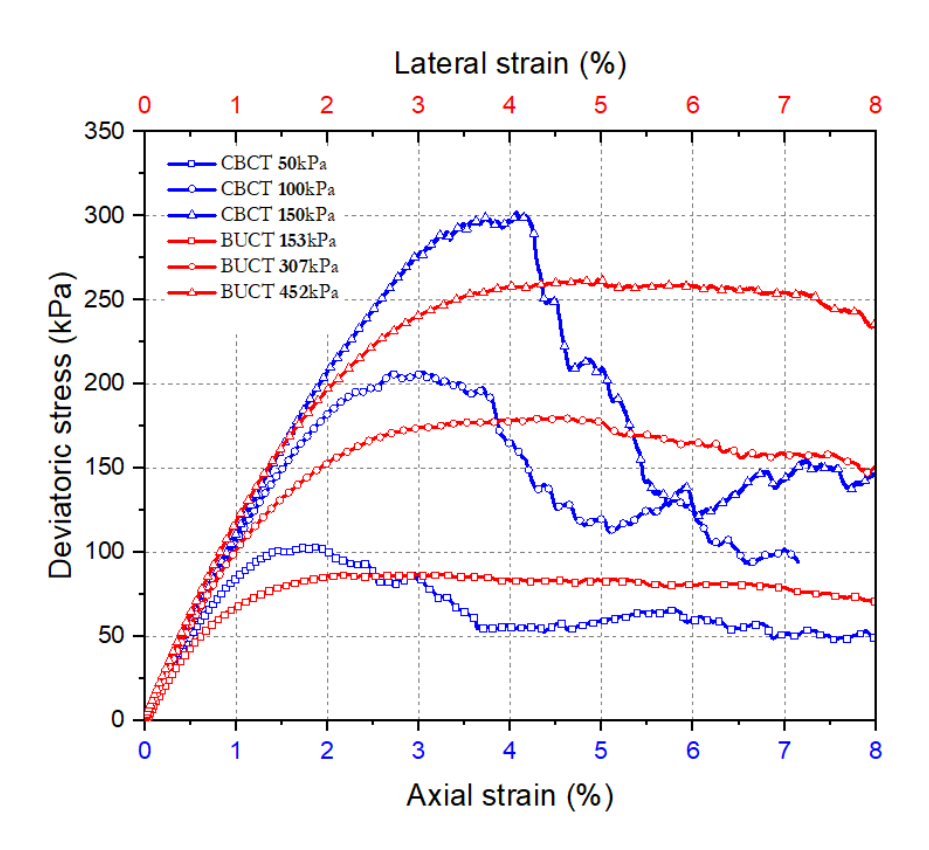


Figure 5.21: deviatoric stresses evolution during CBCT and BUCT.

Figure 5.22 shows the evolution of volumetric strain for CBCT and BUCT tests. The figure shows that for CBCT tests, the soil model initially exhibits contraction behavior, where volumetric strain decreases as axial strain increases. However, beyond a certain axial deformation, the behavior becomes dilative, reflecting soil expansion at peak strength and in the softening phase. This behavior is typical of dense sand subjected to this type of test. In contrast, for the BUCT test, the soil model shows a predominantly dilative behavior throughout the test. Volumetric strain increases continuously with axial strain, indicating persistent expansion of the soil structure. This response has similarities to the behavior of loose sand subjected to compressive shear. The contrasting volumetric responses thus highlight the influence of stress paths and initial density on the deformation characteristics of granular soils.

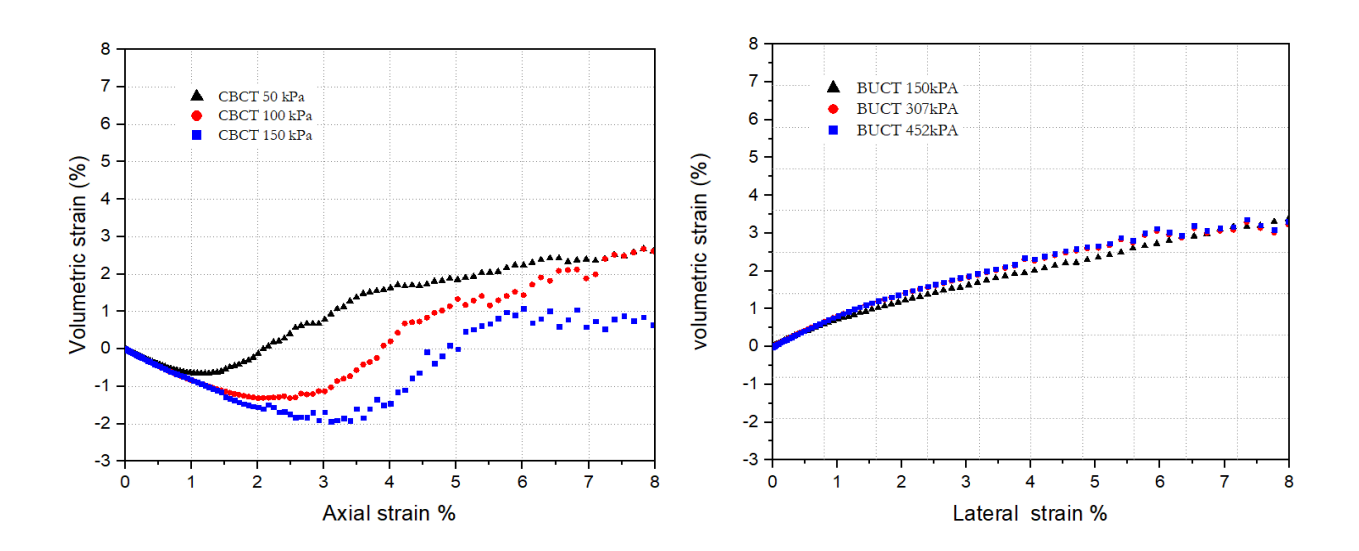


Figure 5.22: Volumetric strain during CBCT and BUCT.

The maximum axial stresses obtained from all the CBCT and BUCT tests were used to plot Mohr's circles and linear Mohr's envelopes (figure 5.23).

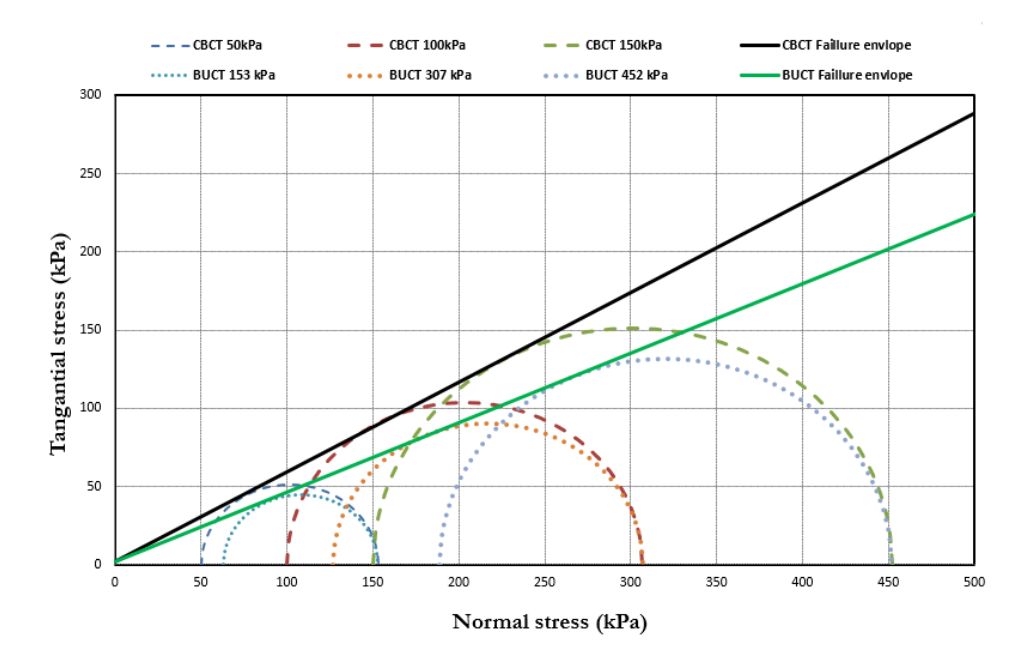


Figure 5.23 CBCT and BUCT Mohr circles and linear Mohr envelopes.

The shear strength parameters obtained from the Mohr envelopes are summarized in the table 5.3.

Test type Peack friction angle (φ_{peak}) Critical friction angle (φ_C) Cohesion (C)CBCT 30 20 0

BUCT 25 // 0

Table 5.3. CBCT and BUCT shear strength parameters

It is clear that the internal friction angle obtained from the unloading shear (BUCT) test ($\varphi = 25^{\circ}$), is different from the two angles obtained from the loading shear (CBCT) test, namely the peak angle ($\varphi_{peak} = 30^{\circ}$) and the critical state angle $\varphi_c = 20^{\circ}$. This shows that the stress path has a significant effect on soil shear strength parameters.

Using the angle of friction obtained from BUCT tests, one obtains a coefficient of lateral pressure in the active state $\left(\varphi=25^{\circ}, \rightarrow K_a=\tan^2\left(\frac{\pi}{4}-\frac{\varphi}{2}\right)\approx 0.4\right)$. This value corresponds well to that obtained from the moving retaining wall model carried out above.

These findings indicate that the accuracy of results for estimating lateral earth pressures using theoretical equations such as the Rankine equation is dependent on the friction angle used. For an accurate calculation, the friction angle to be introduced should be obtained from tests with a stress

path similar to that of the problem to be addressed. Specifically, for this 2D modeling of lateral earth pressure, it is shown that:

- For the passive state, using the peak friction angle obtained from biaxial shear tests with loading yields good results.
- For the active state, the most appropriate test for determining the friction angle, which allows for a correct estimation of lateral pressure, is the biaxial shear test with unloading.

5.10. Conclusion

In this chapter, we investigated the lateral earth pressures in dry granular soils under active and passive limit states using the Discrete Element Method (DEM). A 2D granular backfill was modeled behind a smooth retaining wall, which was subjected to displacements in two directions: towards the backfill for the passive state and away from the backfill for the active state. Additionally, we presented the distribution of lateral earth pressures at rest on the retaining wall and observed that this distribution is not linear due to the presence of arching effects within the granular medium. Furthermore, we analyzed the evolution of lateral pressure distributions on the retaining wall for incremental wall displacements corresponding to an intermediate state and the failure state. The results revealed non-linear pressure distributions in both active and passive states, emphasizing the complexity of stress transfer mechanisms in granular materials.

For the lateral pressure at passive state, the obtained results showed good agreement with those predicted by Rankine's theory using the peak friction angle obtained from conventional biaxial tests. However, in the active state, the lateral pressures obtained were different from those predicted by Rankine's theory. To explain this discrepancy, a biaxial compression test was proposed, replicating the stress path corresponding to the active state. This test yielded a friction angle between the peak and critical state friction angles obtained from conventional biaxial tests. By substituting this friction angle into the Rankine equation, the results obtained are well aligned with those obtained from DEM retaining wall simulations. This finding highlights the significant influence of the stress path on lateral earth pressures, a factor not accounted for in classical lateral earth pressure theories.

This study underscores therefore, the importance of considering stress path effects and the non-linear distribution of lateral pressures due to arching in the analysis of lateral earth pressures.

CONCLUSIONS AND PERSPECTIVES

In this thesis, the discrete element method (DEM) was used to model a granular soil, considering the complex particle-level interactions that govern the macroscopic behavior of the material. Within this framework, specific constitutive models were selected and implemented to accurately capture the mechanical response of granular materials. Notably, the intergranular friction model was a central focus, where an extended Coulomb friction model was implemented to account for the stick-slip phenomenon during interparticle contacts. This approach allowed for a more realistic representation of the complex dynamics inherent in granular systems, particularly under varying loading conditions.

The first application of the developed model was dedicated to the analysis of lateral earth pressure at rest. In this context, a 2D discrete element modeling was used to simulate cyclic oedometer tests, including one-cycle and three-cycle loading scenarios, to investigate the evolution of the lateral earth pressure coefficient (K_0) . The obtained results showed that the evolution of K_0 with loading is in good agreement with well-known empirical formulas derived from experience. In addition, the three-cycle test revealed that K_0 during the unloading phase increases slightly as the loading cycles progress, which can be attributed to grain rearrangement leading to greater overconsolidation with successive cycles. Analysis of load-dependent micromechanical parameters, such as the fabric tensor, the number of contacts, and contact forces, provided the following insights: the evolution of the fabric tensor, which describes the distribution of contact orientations, is primarily driven by differential changes in the number of contacts across different directions. Under isotropic stress conditions, contact orientations are nearly isotropic, but even a slight deviation from stress isotropy significantly disrupts this isotropy. In normally consolidated samples, such as during the first loading cycle, horizontal contacts dominate, increasing horizontal frictional forces and reducing K_0 . Conversely, in overconsolidated samples, vertical contacts become more frequent, enhancing horizontal normal forces and raising K_0 . Furthermore, K_0 is not only influenced by the dominant orientation of contacts but also by the intensity of forces acting on them. A simple three-grain model demonstrated that the evolution of K_0 during a loading-unloading cycle in the oedometer test is ultimately governed by intergranular friction, highlighting its critical role in determining K_0 for overconsolidated soils.

The second application focused on analyzing lateral earth pressures at the active and passive limits using the same model. For this purpose, a moving retaining wall supporting a granular backfill was simulated. The displacements applied to the wall replicate active and passive states. The obtained

lateral earth pressures were compared with those derived from Rankine's equations. Qualitatively, the results aligned well with Rankine's theory; however, quantitative differences were observed. For the passive state, the lateral earth pressure coefficient at peak (K_p) matched the value obtained from Rankine's equation using the peak friction angle derived from a conventional biaxial compression test. In contrast, for the active state, the lateral earth pressure coefficient (K_a) obtained from the simulation was different from that predicted by Rankine's equation. This discrepancy was attributed to the difference in stress paths between the two states. To investigate further, a biaxial compression test with a stress path matching the active state was simulated (unloading biaxial compression test). The friction angle obtained from this test was between the peak and critical state friction angles obtained from the conventional biaxial compression test and estimates accurately the lateral earth pressure through Rankine's theory. This finding indicates that, for an accurate calculation of the lateral earth pressure, the friction angle to be introduced should be obtained from tests with a stress path similar to that of the problem to be addressed.

As perspectives, first, it should be recalled that the results presented in this thesis are obtained from a 2D discrete element modeling with circular shaped elements. The conclusions drawn, even if interesting, remain more qualitative than quantitative. We believe that, in order to be sounder and more beneficial, they should be verified by more advanced numerical models such as 3D models that model natural soils with more details. On the other hand, it would also be interesting to detail more, the micromechanical analysis of the development of failures in the cases of active and passive states, which should contribute to a better understanding of the mechanisms involved as well as the overall macroscopic behavior. Furthermore, it is also interesting to develop physical experiments that support the results obtained. These experiments could, for example, be based on the triaxial device with more control over the imposed stresses and/or displacements.

Annexe A-

Bibliographic References

- [1] Holtz, R. D., & Kovacs, W. D. (1991). Introduction à la géotechnique. Presses inter Polytechnique.
- [2] Brown, E. H., Montgomery, R. F., Richards, P. W., & Wise, M. J. (1970). Geographical Research on the Royal Society/Royal Geographical Society's Expedition to North-Eastern Mato Grosso, Brazil: A Symposium: Discussion. The Geographical Journal, 136(3), 407-409.
- [3] Rothenburg, L., Bathurst, R. J., & Dusseault, M. B. (1989). Micromechanical ideas in constitutive modelling of granular materials. Powders and grains, 89.
- [4] Roodi, G. H., & Mirghasem, A. A. (2009). MODELING OF METAL-STRIP REINFORCED SOIL S TRUCTURES USING THE DISCRETE ELEMENT METHOD. Sharif Journal of Civil Engineering, 25(48.1), 3-13.
- [5] Azéma, E., Radjai, F., Peyroux, R., & Saussine, G. (2007). Force transmission in a packing of pentagonal particles. Physical Review E—Statistical, Nonlinear, and Soft Matter Physics, 76(1), 011301.
- [6] VOIVRET, Charles. Texture et comportement des matériaux granulaires à grande polydispersité. 2008. Thèse de doctorat. Université Montpellier II-Sciences et Techniques du Languedoc.
- [7] Wadell, H. (1932). Volume, shape, and roundness of rock particles. The Journal of Geology, 40(5), 443-451.
- [8] Powers, M. C. (1953). A new roundness scale for sedimentary particles. Journal of Sedimentary Research, 23(2), 117-119.
- [9] Wadell, H. (1932). Volume, shape, and roundness of rock particles. The Journal of Geology, 40(5), 443-451.
- [10] E. J. Garboczi, Three- dimensional mathematical analysis of particle shape using X- ray tomography and spherical harmonics: Application to aggregates used in concrete, Cem. Concr. Res. 32(10) (2002), 1621-1638.
- [11] V. C. Janoo, Quantification of shape, angularity, and surface texture of base course materials, Special Report 98-1, CRREL, US army Corps of Engineers (1998)
- [12] Senetakis, K., Coop, M. R., & Todisco, M. C. (2013). Tangential load–deflection behaviour at the contacts of soil particles. Géotechnique Letters, 3(2), 59-66.
- [13] Sandeep, C. S., Todisco, M. C., Nardelli, V., Senetakis, K., Coop, M. R., & Lourenco, S. D. N. (2018). A micromechanical experimental study of highly/completely decomposed tuff granules. Acta Geotechnica, 13, 1355-1367.
- [14] Yang, H., Baudet, B. A., & Yao, T. (2016). Characterization of the surface roughness of sand particles using an advanced fractal approach. Proceedings of the Royal Society A: Mathematical, Physical and Engineering Sciences, 472(2194), 20160524.
- [15] Miura, K., Maeda, K., & Toki, S. (1997). Method of measurement for the angle of repose of sands. Soils and Foundations, 37(2), 89-96.
- [16] Voivret, C., Radjai, F., Delenne, J. Y., & El Youssoufi, M. S. (2007). Space-filling properties of polydisperse granular media. Physical Review E—Statistical, Nonlinear, and Soft Matter Physics, 76(2), 021301.
- [17] Sallam, A. M. (2004). Studies on modeling angular soil particles using the discrete element method.
- [18] Sallam, A. M. (2004). Studies on modeling angular soil particles using the discrete element method.
- [19] HABIB P., LUONG M.P., (1978) Sols pulvérulents sous chargements cycliques, Séminaire

- Matériaux et Structures sous Chargement Cyclique, 28-29 septembre 1978, Ecole Polytechnique, 91128 Palaiseau.
- [20] HABIB P., LUONG M.P., (1978) Sols pulvérulents sous chargements cycliques, Séminaire Matériaux et Structures sous Chargement Cyclique, 28-29 septembre 1978, Ecole Polytechnique, 91128 Palaiseau.
- [21] Scott, G. D., & Kilgour, D. M. (1969). The density of random close packing of spheres. Journal of Physics D: Applied Physics, 2(6), 863.
- [22] Casagrande, A. (1936). The determination of the pre-consolidation load and its practical significance. In Proc. 1st Int. Conf. Soil Mech. (pp. 3-60).
- [23] Biarez, J., & Hicher, P. Y. (1994). Elementary mechanics of soil behaviour: saturated remoulded soils (pp. xvi+-208).
- [24] Mohkam, 1983. Contribution à l'étude expérimental et théorique du comportement des sables sous chargement cyclique. INPG: PhD Thesis.
- [25] Bouvard, D., & Stutz, P. (1986). Experimental study of rheological properties of a sand using a special triaxial apparatus. Geotechnical Testing Journal, 9(1), 10-18.
- [26] Saïm, R. (1997). Des comportements repères des grains sans colle à un exemple de sol réel (Doctoral dissertation, thèse Ecole centrale de Paris).
- [27] Cundall, P.A., Strack, O.D.L., 1979. A discrete numerical model for granular assemblies. Géotechnique 29, 47–65. https://doi.org/10.1680/geot.1979.29.1.47
- [28] Jean, M., & Moreau, J. J. (1992). Unilaterality and dry friction in the dynamics of rigid body collections. In 1st contact mechanics international symposium (pp. 31-48).
- [29] Radjai, F., & Dubois, F. (2011). Discrete-element modeling of granular materials (pp. 425-p). Wiley Iste.
- [30] Cheung, G., & O'Sullivan, C. (2008). Effective simulation of flexible lateral boundaries in two-and three-dimensional DEM simulations. Particuology, 6(6), 483-500.
- [31] B. Chareyre. Modélisation du comportement d'ouvrages composites sol-géosynthétiquepar élements discrets Application aux ancrages en tranchées en tête de talus. PhD thesis, Université Joseph Fourier, Grenoble, 2003.
- [32] B. Cambou and M. Jean. Hermès Science, 2001.
- [33] F. Calvetti, G. Combe, and J. Lanier. Experimental micromechanical analysis of a 2d granular material: relation between structure evolution and loading path. Mechanics of Cohesive-Frictional Materials, 2:121–163, 1997.
- [34] F. Calvetti, G. Combe, and J. Lanier. Experimental micromechanical analysis of a 2d granular material relation between structure evolution and loading path. Mechanics of Cohesive-Frictional Materials, 2:121–163, 1997.
- [35] Konietzky, H. (2003). Numerical Modeling in Micromechanics via Particle Methods: International PFC Symposium, Gelsenkirchen, Germany, 6-8 November 2002 (1st ed.). Routledge. https://doi.org/10.1201/9780203745335
- [36] Matsushima, T., and H. Saomoto. "Discrete element modeling for irregularly Y-shaped sand grains." NUMGE 2002. 5th European Conference Numerical Methods in Geotechnical Engineering. 2002.
- [37] Alonso-Marroquin, F., S. Luding, and H. J. Herrmann. "The anisotropy of granular materials." arXiv preprint cond-mat/0403064 (2004).

- [38] Nouguier-Lehon, C., E. Vincens, and B. Cambou. "Structural changes in granular materials: the case of irregular polygonal particles." International journal of Solids and Structures 42.24-25 (2005): 6356-6375
- [39] Potapov, Alexander V., and Charles S. Campbell. "A fast model for the simulation of non-round particles." Granular Matter 1.1 (1998): 9-14.
- [40] Pournin, Lionel, et al. "Three-dimensional distinct element simulation of spherocylinder crystallization." Granular Matter 7 (2005): 119-126.
- [41] Kuhn, Matthew R., and Katalin Bagi. "Contact rolling and deformation in granular media." International journal of solids and structures 41.21 (2004): 5793-5820.
- [42] Hong, D.C., McLennan, J.A., 1992. Molecular dynamics simulations of hard sphere granular particles. Physica A: Statistical Mechanics and its Applications 187, 159–171. https://doi.org/10.1016/0378 4371(92)90416-N
- [43] Jean, M., 1999. The non-smooth contact dynamics method. Computer Methods in Applied Mechanics and Engineering 177, 235–257. https://doi.org/10.1016/S0045-7825 (98)00383-1

[44]

- [45] Haff, P.K., Werner, B.T., 1986. Computer simulation of the mechanical sorting of grains. Powder Technology 48, 239–245. https://doi.org/10.1016/0032-5910(86)80048-1
- [46] Kruggel-Emden, H., Simsek, E., Rickelt, S., Wirtz, S., Scherer, V., 2007. Review and extension of normal force models for the Discrete Element Method. Powder Technology 171, 157–173. https://doi.org/10.1016/j.powtec.2006.10.004
- [47] Malone, K.F., Xu, B.H., 2008. Determination of contact parameters for discrete element method simulations of granular systems. Particuology 6, 521–528. https://doi.org/10.1016/j.partic.2008.07.012
- [48] Machado, M., Moreira, P., Flores, P., Lankarani, H.M., 2012. Compliant contact force models in multibody dynamics: Evolution of the Hertz contact theory. Mechanism and Machine Theory 53, 99 121. https://doi.org/10.1016/j.mechmachtheory.2012.02.010
- [49] Suhr, B., Six, K., 2017. Friction phenomena and their impact on the shear behaviour of granular material. Comp. Part. Mech. 4, 23–34. https://doi.org/10.1007/s40571-016-0119-2
- [50] Marchelli Filippo, Di Felice Renzo, 2021. On the Influence of Contact Models on Friction Forces in Discrete Element Method Simulations. Chemical Engineering Transactions 86, 811–816. https://doi.org/10.3303/CET2186136
- [51] Man, T., Zhang, P., Ge, Z., Galindo-Torres, S.A., Hill, K.M., 2022. Friction-dependent rheology of dry granular systems.
- [52] Luding, S., Clément, E., Blumen, A., Rajchenbach, J., Duran, J., 1994. Onset of convection in molecular dynamics simulations of grains. Phys. Rev. E 50, R1762–R1765. https://doi.org/10.1103/PhysRevE.50.R1762
- [53] Luding, S., 2008. Cohesive, frictional powders: contact models for tension. Granular Matter 10, 235 246. https://doi.org/10.1007/s10035-008-0099-x
- [54] Führer, F., Brendel, L., Wolf, D.E., 2024. Correction of the spring-dashpot-slider model. Granular Matter 26, 53. https://doi.org/10.1007/s10035-024-01424-4
- [55] Mindlin_1949_ComplianceOfElasticBodiesInContact.pdf, n.d.
- [56] Walton, O.R., Braun, R.L., 1986. Viscosity, granular-temperature, and stress calculations for shearing assemblies of inelastic, frictional disks. Journal of Rheology 30, 949–980. https://doi.org/10.1122/1.549893

- [57] Shäfer, J., Dippel, S., Wolf, D.E., 1996. Force Schemes in Simulations of Granular Materials. J. Phys. I France 6, 5–20. https://doi.org/10.1051/jp1:1996129
- [58] Heslot, F., Baumberger, T., Perrin, B., Caroli, B., Caroli, C., 1994. Creep, stick-slip, and dry-friction dynamics: Experiments and a heuristic model. Phys. Rev. E 49, 4973–4988. https://doi.org/10.1103/PhysRevE.49.4973
- [59] Bengisu, M.T., Akay, A., 1999. Stick—slip oscillations: Dynamics of friction and surface roughness. The Journal of the Acoustical Society of America 105, 194–205. https://doi.org/10.1121/1.424580
- [60] Togo, T., Shimamoto, T., 2012. Energy partition for grain crushing in quartz gouge during subseismic to seismic fault motion: An experimental study. Journal of Structural Geology 38, 139–155. https://doi.org/10.1016/j.jsg.2011.12.014
- [61] Persson, B.N.J., 2013. Sliding Friction: Physical Principles and Applications. Springer Science & Business Media.
- [62] Berman, A.D., Ducker, W.A., Israelachvili, J.N., 1996. Origin and Characterization of Different Stick-Slip Friction Mechanisms. Langmuir 12, 4559–4563. https://doi.org/10.1021/la950896z
- [63] Dunham, E.M., Rice, J.R., 2008. Earthquake slip between dissimilar poroelastic materials. J. Geophys. Res. 113, 2007JB005405. https://doi.org/10.1029/2007JB005405
- [64] Singh, T.N., Verma, A.K., Kumar, T., Dutt, A., 2011. Influence of shear velocity on frictional characteristics of rock surface. J Earth Syst Sci 120, 183–191. https://doi.org/10.1007/s12040-011 0009-1
- [65] Yang, C.-M., Yu, W.-L., Dong, J.-J., Kuo, C.-Y., Shimamoto, T., Lee, C.-T., Togo, T., Miyamoto, Y., 2014. Initiation, movement, and run-out of the giant Tsaoling landslide What can we learn from a simple rigid block model and a velocity–displacement dependent friction law? Engineering Geology 182, 158–181. https://doi.org/10.1016/j. enggeo.2014.08.008
- [66] Armstrong-Hélouvry, B., Dupont, P., De Wit, C.C., 1994. A survey of models, analysis tools and compensation methods for the control of machines with friction. Automatica 30, 1083–1138. https://doi.org/10.1016/0005-1098(94)90209-7
- [67] Luding, S., Clément, E., Blumen, A., Rajchenbach, J., Duran, J., 1994. Anomalous energy dissipation in molecular-dynamics simulations of grains: The "detachment" effect. Phys. Rev. E 50, 4113–4122. https://doi.org/10.1103/PhysRevE.50.4113
- [68] Malone, K.F., Xu, B.H., 2008. Determination of contact parameters for discrete element method simulations of granular systems. Particuology 6, 521–528. https://doi.org/10.1016/j.partic.2008.07.012
- [69] Machado, M., Moreira, P., Flores, P., Lankarani, H.M., 2012. Compliant contact force models in multibody dynamics: Evolution of the Hertz contact theory. Mechanism and Machine Theory 53, 99 121. https://doi.org/10.1016/j. mechmachtheory.2012.02.010
- [70] Ketterhagen, W.R., Curtis, J.S., Wassgren, C.R., 2005. Stress results from two-dimensional granular shear flow simulations using various collision models. Phys. Rev. E 71, 061307. https://doi.org/10.1103/PhysRevE.71.061307
- [71] Teufelsbauer, H., Wang, Y., Pudasaini, S.P., Borja, R.I., Wu, W., 2011. DEM simulation of impact force exerted by granular flow on rigid structures. Acta Geotech. 6, 119–133. https://doi.org/10.1007/s11440-011-0140-9
- [72] Mansouri, M., El Youssoufi, M.S., Nicot, F., 2016. Numerical simulation of the quicksand phenomenon by a 3D coupled Discrete Element Lattice Boltzmann hydromechanical model. International Journal for Numerical and Analytical Methods in Geomechanics 41, 338–358. https://doi.org/10.1002/nag.2556
- [73] Gallas, J.A.C., Herrmann, H.J., Sokołowski, S., 1992. Molecular dynamics simulation of powder

- fluidization in two dimensions. Physica A: Statistical Mechanics and its Applications 189, 437–446. https://doi.org/10.1016/0378-4371(92)90055-U
- [74] Melin, S., 1994. Wave propagation in granular assemblies. Phys. Rev. E 49, 2353–2361. https://doi.org/10.1103/PhysRevE.49.2353
- [75] Wei, H., Li, M., Li, Y., Ge, Y., Saxén, H., Yu, Y., 2019. Discrete Element Method (DEM) and Experimental Studies of the Angle of Repose and Porosity Distribution of Pellet Pile. Processes 7, 561. https://doi.org/10.3390/pr7090561
- [76] Wei, S., Wei, H., Saxen, H., Yu, Y., 2022. Numerical Analysis of the Relationship between Friction Coefficient and Repose Angle of Blast Furnace Raw Materials by Discrete Element Method. Materials 15, 903. https://doi.org/10.3390/ma15030903
- [77] Dhaouadi, W., Marteau, E., Kolvenbach, H., Choukroun, M., Molaro, J.L., Hodyss, R., Schulson, E.M., 2022. Discrete element modeling of planetary ice analogs: mechanical behavior upon sintering. Granular Matter 24, 12. https://doi.org/10.1007/s10035-021-01167-6
- [78] Jaky, J.: The coefficient of earth pressure at-rest. Journal of Society of Hungarian Architects and Engineers, 355–358 (1944)
- [79] Chu, J., Gan, C.L.: Effect of void ratio on K0 of loose sand. G'eotechnique 54, 285–288 (2004) https://doi.org/10.1680/geot.2004.54.4.285
- [80] Ionescu, D.: Evaluation of the Engineering Behaviour of Railway Ballast. Ph.D. Thesis. University of Wollongong, Wollongong, Australia (2004)
- [81] Wanatowski, D., Chu, J.: K0 of sand measured by a plane-strain apparatus. Canadian Geotechnical Journal 44(8), 1006–1012 (2007)
- [82] Northcutt, S., Wijewickreme, D.: Effect of particle fabric on the coefficient of lateral earth pressure observed during one-dimensional compression of sand. Canadian Geotechnical Journal 50, 457–466 (2013) https://doi.org/10.1139/cgj-2012-0162
- [83] Lee, J., Yun, T.S., Lee, D., Lee, J.: Assessment of K0 correlation to strength for granular materials. Soils and Foundations 53, 584–595 (2013) https://doi.org/10.1016/j.sandf.2013.06.009
- [84] Santana, T., Candeias, M.: Effect of void ratio on K0 of a sand by means of triaxial stress-path testing. Geotechnical and Geological Engineering 36, 257–266 (2018) https://doi.org/10.1007/s10706-017 0324-7
- [85] Talesnick, M.: A different approach and result to the measurement of K0 of granular soils. ICE, G'eotechnique 62(8), 1041–1045 (2012)
- [86] Li, L., Dai, Z., Liu, R., Jian, F.: Experimental study on the coefficient of earth pressure at rest for sand. Buildings 13(1276) (2023) https://doi.org/10.3390/buildings13051276
- [87] Okochi, Y., Tatsuoka, F.: Some factors affecting K0-values of sand measured in triaxial cell. Soils and Foundations, Japanese Society of Soil Mechanics and Foundation Engineering 24(3), 52–68 (1984)
- [88] Mitchell, J.K., Soga, K.: Fundamentals of Soil Behavior ?(Vol. 3, P. USA). John Wiley & Sons, New York (2005)
- [89] Tsukamotoo, Y., Ishihara, K., Nonak, T.: Undrained deformation and strength characteristics of soils from reclaimed deposits in kobe. Soils and Foundations, 47–55 (1998) https://doi.org/10.3208/sandf.38. Special 47
- [90] Zlatovic, S., Ishihara, K.: Normalized behavior of very loose non-plastic soils: effects of fabric. Soils and Foundations 37(4), 47–56 (1997)
- [91] Guo, P.: Effect of density and compressibility on K0 of cohesionless soils. Acta Geotechnica 5, 225 238 (2010) https://doi.org/10.1007/s11440-010-0125-0
- [92] Gao, Y., Wang, Y.H.: Experimental and dem examinations of K0 in sand under different loading

- conditions. Journal of Geotechnical and Geoenvironmental Engineering 140, 04014012 (2014) https://doi.org/10.1061/(ASCE)GT.1943-5606.0001095
- [93] Mayne, P., Kulhawy, F.: K0-ocr relationships in soil. Journal of the Geotechnical Engineering Division 108, 851–872 (1982)
- [94] Zeng, X., Ni, B.: Stress-induced anisotropic gmax of sands and its measurement. Journal of Geotechnical and Geoenvironmental Engineering 125(9), 741–749 (1999)
- [95] Yun, T.S., Lee, J., Lee, J., Choo, J.: Numerical investigation of the at-rest earth pressure coefficient of granular materials. Granular Matter 17, 413–418 (2015). https://doi.org/10.1007/s10035-015-0569-x
- [96] Lopera Perez, J.C., Kwok, C.Y., O'Sullivan, C., Huang, X., Hanley, K.J.: Numerical study of one dimensional compression in granular materials. G'eotechnique Letters 5, 96–103 (2015) https://doi.org/10.1680/jgele.14.00107
- [97] Khalili, M.H., Roux, J.-N., Pereira, J.-M., Brisard, S., Bornert, M.: Numerical study of one dimensional compression of granular materials. i. stress-strain behavior, microstructure, and irreversibility. Physical Review E 3(95), 032907 (2017)
- [98] Gu, J. X.and Hu, Huang, M., Yang, J.: Discrete element analysis of the K0 of granular soil and its relation to small strain shear stiffness. International Journal of Geomechanics 18, 06018003 (2018) https://doi.org/10.1061/(ASCE)GM.1943-5622.0001102
- [99] Chen, H., Zhao, S., Zhao, J., Zhou, X.: The microscopic origin of K0 on granular soils: the role of particle shape. Acta Geotechnica 16, 2089–2109 (2021). https://doi.org/10.1007/s11440-021-01161-5
- [100] Duncan, J. M., & Mokwa, R. L. (2001). Passive earth pressures: theories and tests. Journal of geotechnical and geoenvironmental engineering, 127(3), 248-257.
- [101] Rankine, W.J.M.: On the stability of loose earth. Scotl. Philos. Trans. R. Soc. Lond. 147, 9–27 (1857)
- [102] Coulomb C.A.: Essai sur une application des regles des maximis et minimis a quelques problemes de statique relatifs a l'architecture. Memoires de l'Academie Royale pres Divers Savants, vol. 7, pp.343–387 (in French)
- [103] Fang, Y.S., Chen, T.J., Wu, B.F.: Passive earth pressure with various wall movements. J. Geotech. Eng. (ASCE) 120(8), 1307–1323(1994)
- [104] Bang, S.: Active earth pressure behind retaining walls. J. Geotech. Eng. (ASCE) **111**(3), 407–412 (1985)
- [105] Handy, R.L.: The arch in soil arching. J. Geotech. Eng. (ASCE) 111(3), 302–318 (1985)
- [106] Harrop-Williams, K.: Arching in soil arch. J. Geotech. Eng. (ASCE) 115(3), 415–419 (1989)
- [107] Paik, K.H., Salgado, R.: Estimation of active earth pressure against rigid retaining walls considering arching effect. Geotechnique **53**(7), 643–645 (2003)
- [108] Chang, M.F.: Lateral earth pressure behind rotating walls. Can. Geotech. J. 34(2), 498–509 (1997)
- [109] Terzaghi, K.: Record earth pressure testing machine. ENR 109(29), 365–369 (1932)
- [110] Terzaghi, K.: Large retaining wall test I-pressure of dry sand. ENR 112(1), 136–140 (1934)
- [111] Terzaghi, K.: Large retaining wall test II-pressure of saturated sand. ENR 112(22), 259–262, 316 318, 403–406, 503–508 (1934)
- [112] Schofield, A.N.: The development of lateral force of sand against the vertical face of a rotating model foundation. In: Proceedings of the 5thInternational Conference on SoilMechanics and Foundation Engineering, Paris, vol. 2, pp. 479–494 (1961)
- [113] Matteotti, G.: Some results of quay-wall model tests on earth pressure. Proc. Inst. Civ. Eng. Lond. 47, 184–204 (1970)

- [114] Bros, B.: The influence of model retaining wall displacements on active and passive earth pressure in sand. In: Proceedings of the 5th European Conference on Soil Mechanics, vol. 1, pp. 241–249 (1972)
- [115] Sherif, M.M., Mackey, R.D.: Pressure on retaining wall with repeated loading. J. Geotech. Eng. (ASCE) 103(11), 1341–1345 (1977)
- [116] Matsuo, M., Kenmochi, S., Yagi, H.: Experimental study on earth pressure of retaining wall by field test. Soils Found. 18(3), 27–41 (1978)
- [117] Fang, Y.S., Ho, Y.C., Chen, T.J.: Passive earth pressure with critical state concept. J. Geotech. Eng. (ASCE) 128(8), 651–659 (2002). http://ascelibrary.org/doi/abs/10.1061/%28ASCE%
- [118] Fang, Y.S., Ishibashi, I.: Static earth pressure with various wall movements. J. Geotech. Eng (ASCE) 112(3), 317–333 (1986)
- [119] Clough, G.W., Duncan, J.M.: Finite element analysis of retaining wall behavior. J. Geotech. Eng. (ASCE) 97(12), 1657–1673 (1971)
- [120] Ozawa, Y., Duncan, J.M.: Elasto-plastic finite element analyses of sand deformations. In: Proceedings of 2nd International Conference on Numerical Methods in Geomechanics, Blacksburg, USA, pp. 243–263 (1976)
- [121] Nakai, T.: Analysis of earth pressure problems considering the influence of wall friction and the wall deflection. In: Proceedings of the 5th International Conference on Numerical and Analytical Methods in Geomechanics. Nagoya, Japan, pp. 765–772 (1985)
- [122] Potts, D.M., Fourie, A.B.: A numerical study of the effects of wall deformation on earth pressure. Int. J. Numer. Anal. Methods Geomech. 10, 383–405 (1986)
- [123] Bhatia, S.K., Bakeer, R.M.: Use of the finite element method in modeling a static earth pressure problem. Int. J. Numer. Anal. Methods Geomech. 13, 207–213 (1989)
- [124] Matsuzawa, H., Hazarika, H.: Analyses of active earth pressure against rigid retaining walls subjected to different modes of movement. Soils Found. 36(3), 51–65 (1996)
- [125] Rudnicki, J.W., Rice, J.R.: Conditions for the localization of deformation in pressure-sensitive dilatant materials. J. Mech. Phys. Solids 23, 371–394 (1975)
- [126] Vardoulakis, I.: Shear band inclination and shear modulus of sand in biaxial tests. Int. J. Numer. Anal. Methods Geomech. 4, 103–119 (1980)
- [127] Papamichos, E., Vardoulakis, I.: Shear band formation in sand according to non-coaxial plasticity model. Géotechnique 45, 649–661 (1995)
- [128] Yatomi, C., Yashima, A., Iizuka, A., Sano, I.: General theory of shear bands formation by a noncoaxial Cam-clay model. Soils Found. 29(3), 41–53 (1989)
- [129] Hazarika, H., Matsuzawa, H.: Wall displacement modes dependent active earth pressure analyses using smeared shear band method with two bands. Comput. Geotech. 19, 193–219 (1996)
- [130] Jiang, M.J., Yan, H.B., Zhu, H.H., Utili, S.: Modeling Shear behavior and strain localization in cemented sands by two-dimensional distinct element method analyses. Comput. Geotech. 38, 14–29 (2011)
- [131] Zienkiewicz, O.C., Taylor, R.L.: The Finite Element Method for Solid and Structural Mechanics. Butterworth-Heinemann, London (2005)
- [132] Itasca Consulting Group Inc.: Particle Flow Code in 2 Dimensions, PFC2D Version 3.0. Minneapolis (2002)
- [133] Jiang, M.J., Leroueil, S., Konrad, J.M.: Insight into shear strength functions of unsaturated granulates by DEM analyses. Comput. Geotech. 31, 473–489 (2004)
- [134] Sekkel, A. and Meghachou, M. 2013. The Effect of Displacement Mode of Rigid Retaining Walls on

- Shearing Bands by Active Earth Pressure. Engineering, Technology & Applied Science Research. 3, 5 (Oct. 2013), 526–531. DOI:https://doi.org/10.48084/etasr.374.
- [135] Clough, G., and Duncan, J. (1991). "Earth pressures." Chapter 6, Foundation engineering handbook, H.-Y. Fang, ed., Springer, New York,223–235.
- [136] Becker, D. E., and Moore, I. D. (2006). Canadian foundation engineering manual, Canadian Geotechnical Society, Alliston, Canada
- [137] Ni, P., Mangalathu, S., Song, L., Mei, G., & Zhao, Y. (2018). Displacement-dependent lateral earth pressure models. Journal of Engineering Mechanics, 144(6), 04018032.
- [138] Narain, J., Saran, S., & Nandakumaran, P. (1969). Model study of passive pressure in sand. Journal of the soil mechanics and foundations division, 95(4), 969-984.
- [139] Kabanemi, K. K., & Hétu, J. F. (2012). Effects of bending and torsion rigidity on deformation and breakage of flexible fibers: A direct simulation study. The Journal of Chemical Physics, 136(7).
- [140] Janssen H.A. 1895. Versuche über Getreidedruck in Silozellen, Zeitung des Vereins deutscher Ingenieure, 39, 1045-1049
- [141] Spanglar, M.G. and Handy, R.L. (1982): 'Soil Engineering', 4th Ed. Harper and Row, New york.
- [142] Dalvi, R. S., & Kulkarni, R. S. (2013). Effect of Arching on Passive Earth Pressure for Rigid Retaining Walls. Int. J. on Mech. Eng. and Robotics, 1(1), 1-8.
- [143] FANG, Y. and Ishibhishi, I. (1986): "Static Earth Pressure with Various Wall Movements", Journal of Geotechnical Engineering, ASCE, 112, No.3, pp.3 13-333.
- [144] Handy, R. L. (1985). The arch in soil arching. Journal of Geotechnical Engineering, 111(3), 302-318.

تقدم هذه الأطروحة مساهمة في تحليل ضغوط التربة الجانبية في حالات مختلفة. حالة السكون، الحالة السلبية والحالة النشطة. تركز الدراسة على عينة حبيبية جافة باستخدام النمذجة العددية ثنائية الأبعاد بطريقة العناصر المنفصلة. في هذا العمل، تم تمثيل الحبيبات باقراص مع إدخال مقاومة للدوران. تم حساب القوى الناظمية للتفاغل باستخدام نموذج لزج مرن، بينما تم تحديد قوى الاحتكاك باستخدام نموذج لزج مرن يأخذ في الاعتبار الانزلاق وظاهرة الالتصاق والانزلاق.(stick-slip)

الجزء الأول من التحليل يتناول ضغط التربة الجانبي في حالة السكون، حيث تم تطوير نموذج لاختبار الأودوميتر. أظهرت النتائج أن تطور معامل ضغط التربة الجانبي K_0 تاريخ التحميل يتوافق بشكل جيد مع الصيغ التجريبية المستخلصة من البيانات التجريبية، حيث يزداد K_0 مع زيادة نسبة التضاغط للتربة. بالإضافة إلى ذلك، أظهر التحليل الميتال الميتوب التحديد الاتصالات الأفقية بين الحبيبات، مما يؤدي إلى قوى احتكاك أفقية أعلى وبالتالي قيمة أقل لـ K_0 في المقابل، في العينة المضغوطة بشكل زائد، تصبح الاتصالات العمودية أكثر تواترًا، مما يزيد من القوى الناظمية الأفقية ويؤدي إلى زيادة K_0 باستخدام نموذج بسيط من ثلاث حبيبات، تم إبراز أن تطور K_0 خلال دورة تحميل وتفريغ في اختبار الأودوميتر يتأثر بالاحتكاك بين الحبيبات.

الجزء الثاني من التحليل يركز على ضغوط التربة الجانبية في كل من الحالتين السلبية والنشطة. تم تطوير نموذج لعينة حبيبية مدعومة بجدار متحرك صلب. أظهرت النتائج أنه في الحالة السلبية، يتطابق معامل ضغط التربة الجانبي عند الذروية (K_p) مع القيمة التي تم الحصول عليها من معادلة رانكين عند استخدام زاوية الاحتكاك الذروية المستخلصة من اختبار الضغط التنائي المحوري التقليدي. أما في الحالة النشطة، فإن معامل ضغط التربة الجانبي (K_a) يتطابق مع المعامل المتوقع من معادلة رانكين إذا تم استخدام زاوية الاحتكاك الداخلي المستخلصة من اختبارات القص التي يكون مسار الإجهاد فيها مشابها لحالة الضغط الجانبي النشط.

كلمات مفتاحية: التربة الرملية، طريقة العناصر المنفصلة، الاحتكاك، الضغط الجانبي، حالة السكون، النشطة، السلبية.

Résumé:

Cette thèse présente une contribution à l'analyse des pression latérales des terres aux différents états ; de repos, passif et actif. L'analyse concerne un dépôt granulaire à l'état sec, elle est menée par une modélisation numérique par éléments discrets 2D. Dans ce travail, les grains sont modélisés par des éléments circulaires avec introduction d'une résistance au roulement, les forces normales de contact sont calculées par un modèle viscoélastique et les forces tangentielles sont calculées par un modèle viscoélastique avec glissement tenant compte du phénomène stick-slip. La première partie de cette analyse concerne la pression latérale au repos, pour cela un modèle d'un essai œdométrique cyclique est mis au point. Les résultats obtenus ont démontré que l'évolution du coefficient des pressions latérales des terres K_0 avec l'historique du chargement est en bon accord avec celle des formules empiriques dérivées de l'expérience, où K_0 augmente avec le degré de surconslidation du sol. De plus, l'analyse micromécanique a montré que pour un échantillon normalement consolidé, les contacts horizontaux sont plus dominants, par conséquence les forces de frottement horizontales sont plus élevées ce qui donne une faible valeur de K_0 . Pour un échantillon surconsolidé, les contacts verticaux deviennent plus fréquents, ce qui augmente les forces normales horizontales et conduit à une augmentation de K_0 . En utilisant un modèle simple à trois grains, il est mis en évidence que l'évolution de K_0 selon une boucle pour un cycle de chargement-déchargement dans l'essai oedométrique résulte du frottement intergranulaire. La deuxième partie concerne l'analyse concerne la pression latérale des terres aux deux états, passif et actif. Pour un modèle d'un dépôt granulaire soutenu par un mur rigide déplaçable est mis au point. Les résultats obtenus ont montré que, pour l'état passif, le coefficient de pressi on latérale du sol au pic (K_p) correspondait à la valeur obtenue à partir de l'équation de Rankine en utilisant l'angle de frottement au pic dérivé d'un essai de compression biaxiale conventionnel. En revanche, pour l'état actif, le coefficient de pression latérale des terres (K_a) correspond au coefficient prédit par l'équation de Rankine si l'angle de frottement interne introduit est dérivé d'essais de cisaillement avec un chemin de contrainte similaire à celui de l'état actif des pression latérales.

Mots Clés: Sol Granulaire, Méthode des Éléments Discrets, pressions latérales des terres, au repos, active, passive.

Abstract:

This thesis presents a contribution to the analysis of lateral earth pressures in different states; at rest, passive and active. The analysis concerns a granular deposit in the dry state, and is carried out using 2D discrete element numerical modeling. In this work, the grains are modeled by circular elements with the introduction of a rolling resistance, the normal contact forces are calculated by a viscoelastic model and the tangential forces are calculated by a viscoelastic model with sliding taking into account the stick-slip phenomenon. The first part of this analysis deals with lateral pressure at rest, for which a model of a cyclic odometer test is developed. It is shown that the evolution of the lateral earth pressure coefficient K_0 with loading history is in good agreement with that of empirical formulas derived from experience, where K_0 increases with the increase of soil's overconsolidation ratio. Furthermore, micromechanical analysis has shown that for a normally consolidated sample, horizontal contacts are more dominant, and consequently horizontal friction forces are higher, resulting in a low value of K_0 . For an overconsolidated sample, vertical contacts become more frequent, increasing horizontal normal forces and leading to an increase in K_0 . Using a simple three-grain model, it is highlighted that the evolution of K_0 along a loop for a loading-unloading cycle in the oedometer test results from intergranular friction. The second part concerns the analysis of lateral earth pressure in both passive and active states. A model of a granular deposit supported by a rigid moving wall is developed. The obtained results have shown that, for the passive state, the lateral earth pressure coefficient at peak (K_n) matched the value obtained from Rankine's equation using the peak friction angle derived from a conventional biaxial compression test. Whereas, for the active state, the lateral earth pressure coefficient (Ka) matches the coefficient predicted by Rankine's equation if the introduced internal friction angle is derived from shear tests with stress path similar to that of the active lateral pressure state.

Key Words: Granular soil, Discrete Element Method, lateral earth pressure, at rest, active, passive.